Compositionally Complex Titanium Niobium Oxynitride Materials for Solar-Driven Photochemistry

by

James J. Brancho

A dissertation submitted in partial fulfillment
of the requirements for the degree of
Doctor of Philosophy
(Chemistry)
in the University of Michigan
2017

Doctoral Committee:

Associate Professor Bart M. Bartlett, Chair
Professor Kevin J. Kubarych
Associate Professor Stephen Maldonado
Professor Jamie D. Phillips

James J. Brancho

jbrancho@umich.edu

ORCID iD: 0000-0002-8175-6103

To Joey, whose curiosity and enthusiasm have always inspired my own.

Acknowledgements

Chronologically, more or less –

To my mother Melissa, my father Jim, my brothers Mike and Matt, and my sister Jennie, thank you for this life, for pushing me always, and for the love, support, and perspective I needed to make my way northward. To my siblings, your perseverance and creativity impress and inspire me more than you could ever know.

To my grandparents Louise, Dicky, Linda, and Joey, thank you especially for your kindness and constant encouragement. There have been many phone calls on a nighttime walk back from the lab that have turned my week around. Thank you for cosigning loans (ick) when I needed it most. To all the Kobucks, Branchos, and Snyders, thank you all for influencing me as vibrant individuals and for showing me that there is no one right way to be.

To my roots in Pennsylvania – Andrew and the Sabol family, and also Carrie, Corey, and Heather – thank you for remaining unimpressed by this career move. You keep my head small and my heart huge. I treasure our friendships and the ability we have to pick things up in Pittsburgh with no time lost.

To Kim, thank you in one thousand unnamable ways for growing up with me.

To Elizabeth, Rachel, Brad, and Jared, thank you for tolerating a weird senior in your group. Thank you for Oleander. Thank you for making me feel at home at Duquesne and for memories that still make me laugh (and worry a little).

To my late undergraduate advisor, Dr. Jeffry D. Madura, I owe you so much. Thank you for conjuring space for me in your lab during a delicate time of transition in my career. Thank you

for a challenge more difficult than any I had yet faced in school. Thank you for your support, for sending me around the country to present, for making me feel like a rock star at every step of the way. Your influence in my life as a scientist and in the Duquesne community cannot be overstated, and you will be sorely missed.

To Dr. Jeff Evanseck, thank you for guiding my application to graduate school, for expecting more of me than I expected of myself, and for your incredible advising and classroom presence.

To my committee chair Dr. Bart Bartlett, and to my committee Dr. Stephen Maldonado, Dr. Kevin Kubarych, and Dr. Jamie Phillips, thank you for guiding me in learning what it means to be a professional chemist. From you I have learned to not always rely on traditional sources or methods to find answers, to always do "the boring experiment," and that, on occasion, I do know what I'm doing.

To Mitchell, Tim, Betsy, Charles, and Michael, thank you for your friendship through graduate school and onward. Birthday dinners, potluck dinners, Fourth of July dinners, game night dinners, wedding dinners – all of these food-based experiences will stick positively to my bones and in my mind. I wish you all the best and hope that we can remain in touch as we migrate and become professionals.

To the Old Lab – Joe, Chelsea, Xiao, Brendo, Ben, Amy, Frances, and Megan – thank you for teaching me how to be a synthetic chemist and how we can learn from one another as researchers. I must leave space to especially thank Tanya for her tremendous, heroic effort in founding the lab and in establishing this exciting project that I've gotten to carry forward. I also want to especially thank Kayla and Emily. You were the first in Michigan to invite me into your social lives, and I'll never forget that. The two of you have been such incredible support for me as a professional and as a human being. I would not have passed candidacy or become a blogger without your guidance and encouragement. I owe you so much.

To Susie Hamilton, thank you for helping me rediscover my strength.

To the New Lab – Aaron, Andy, Adam, Sam, John D., and Dan – thank you for game nights, fantasy football, and for getting me through this last phase of my degree. Thank you for your ideas in working out what have been some difficult finishing experiments.

To Nicky, thank you for Frank's Diner and for hockey adventures. Our Detroit trips mark some of the high points of my time here.

I am indebted to the Graduate Employees Organization for fighting tirelessly for our contract, which has enabled me to live comfortably throughout graduate school without having to worry about my health or legal rights. Our labor union is spectacular, and the membership is full of too many inspired individuals to name here. Thank you all for shaping my political identity, for teaching me what my time is worth, and for everything that you have done and continue to do. Solidarity forever!

To Dr. Ginger Shultz, Emilia Askari, Julie Halpert, Alex Taylor, Liz Wason, Kevin Boehnke, Barbara Lucas, Sara Talpos, Ada Hagan, Irene Park, MiSciWriters, and a whole cadre of others, thank you immensely for your contributions to my development as a science writer. I have devoured every bit of ENVIRON 320, Arbor Brewing science writing meetups, and all of the blogging and editing experience we've participated in together. You are all talented, inquisitive, and wonderfully supportive, and I owe my next job appointment to all of you.

To Sarah, Angelina, and John W., bless your beautiful hearts, thank you.

To Lily, thank you for your energy, your boundless care, for helping me feel at home with myself –

– and to Laurel and Fiona as well, thank you for teaching me how joy works, for a deep sense of authentic community, and for more honest compassion than I know what to do with.

I am grateful to the United States Department of Energy (DE-FG02-11ER16262, DE-SC0006587) and the National Science Foundation (DMR-1253347) for funding this work. I also thank Rackham Graduate School and Dow Chemical Company (via the Karle Symposium) for travel funding to various conferences for presentations.

Table of Contents

Dedication **ii**
Acknowledgements **iii**
List of Tables **viii**
List of Figures **ix**
List of Appendices **xiv**
Abstract **xv**

Chapter 1: Introduction **1**
1.1 Future Energy Demands Necessitate Renewable Sources and Storage 1
1.2 Water Splitting as an Example of Solar Energy Storage 2
1.3 General Considerations for Semiconductor Photocatalysts 4
1.4 Notable Photochemical and Photoelectrochemical Systems 8
1.5 Scope of This Thesis 9

Chapter 2: Previous Studies Furthering Single Ion and Co-Doping in TiO_2 **13**
2.1 Modifying Titanium Dioxide by Single Ion Doping 13
2.2 Essential Vocabulary to Describe Band Engineering and Electronic Structure 16
2.3 Co-doped and Co-incorporated TiO_2 19
2.4 Challenges for Preparing and Characterizing Co-Alloyed Materials 21

Chapter 3: Visible Light Water Oxidation Using a Co-Catalyst Loaded Anatase-Structured $Ti_{1-(5x/4)}Nb_xO_{2-y-\delta}N_y$ Compound Prepared By Traditional Syntheses **31**
3.1 Introduction 31
3.2 Experimental Procedures 32
3.3 Physical Characterization by PXRD and HRTEM 34
3.4 Photochemical Water Oxidation with TiNbON-25 35
3.5 Kinetic Role and Stability of TiNbON-25 38
3.6 Conclusions 40

Chapter 4: Urea-Glass Preparation of Titanium Niobium Nitrides and Subsequent Oxidation to Photoactive Titanium Niobium Oxynitrides **42**
4.1 Introduction 42
4.2 Materials Preparation 43

4.3 Characterization and Compositional Analysis 43
4.4 Methylene Blue Photodegradation Procedure 45
4.5 Urea-Glass Synthesis of $Ti_{1-x}Nb_xN$ 46
4.6 Nitride Oxidations 47
4.7 Methylene Blue Photomineralization Rate Constants 50
4.8 Compositional Analysis Results 51
4.9 Conclusions 53

Chapter 5. Preparation of Titanium Niobium Oxynitride by an Improved Urea-Glass Synthesis Using a $CaCO_3$ Additive 55
5.1 Introduction 55
5.2 Materials Preparation 56
5.3 Materials Characterization 56
5.4 Methylene Blue Degradation Procedure 57
5.5 Effect of Temperature and Urea Content on Product Composition 57
5.6 Optical and Photochemical Properties 61
5.7 Conclusions and Outlook 64

Chapter 6. $Cu_{1-x}Ni_xWO_4/WO_3$ Heterojunction Photoanodes Towards Solar Water Oxidation with Improved Faradaic Efficiency 66
6.1 Introduction 66
6.2 Experimental Procedures 68
6.3 Physical Characterization of BHJ Photoanodes 71
6.4 Photoelectrochemistry and Charge-Transfer Kinetics of BHJ Electrodes 72
6.5 Photoelectrochemical Oxygen Evolution 75
6.6 Hydroxyl Radical Trapping using α-Thujone 76
6.7 Conclusions 79

Chapter 7. Conclusions and Potential Future Directions 81
7.1 Summary of Presented Work 81
7.2 Ammonia-Selective Electrodes for Compositional Analysis 82
7.3 Thin-Film Photoelectrodes of TiNbON 83
7.4 Further Reactivity Studies with TiNbON Prepared by Urea-Glass Synthesis 84
7.5 Concluding Remarks 85

Appendices 86

List of Tables

Table 2.1. Composition and IPCE data for modified TiO_2 electrodes. [a]: compositional analysis via XPS and does not represent bulk concentration unless otherwise noted. Variable subscripts imply undetermined values. [b]: Bulk concentration of Nb only determined by EDX. [c]: surface concentrations determined by secondary ion mass spectrometry, see ref. 62. 21

Table 2.2. Composition and photochemical pollutant degradation activity for modified TiO2 photocatalyst powders. [a]: compositional analysis via XPS and does not represent bulk concentration unless otherwise noted. Variable subscripts or "nd" imply undetermined values. [b]: Incident light intensities not reported. "UV + visible" refers to an unfiltered metal halide lamp (Philips HPA 400/30S). 21

Table 5.1. First-order Langmuir-Hinshelwood rate constants (k_{LH}) for methylene blue degradation and dye sorption measurements (q_{rel}) over TiNbON prepared by Ca^{2+}-assisted urea-glass synthesis before and after an additional annealing step. 64

Table 6.1. Average values of photocurrent response in μA for WO_3 and BHJ electrodes in denoted solutions. 74

Table 6.2. GCMS yields of α-thujone oxidation products using the denoted working electrodes expressed as a percentage of total detected products. *: Total radically-oxidized products per coulomb, normalized to ROP/C detected using WO_3. 77

Table A1. XPS Ratios of N_s/N_i 86

Table B1. Metal contents for $Ti_{1-x}Nb_xN$ found by energy dispersive X-ray spectroscopy. 90

Table B2. First-order Langmuir-Hinshelwood rate constants for methylene blue degradation (k_{LH}) and specific methylene blue adsorption (q_{rel}) over TiNbON-*x* compounds, along with BET surface areas. 91

List of Figures

Figure 1.1. Schematic representation of various solar-to-hydrogen schemes which can involve water splitting. Reproduced from ref. 3. Reprinted with permission. 3

Figure 1.2. A minimum band gap is imposed by the reduction potentials for HER and OER along with associated overpotentials (η) for those reactions. The requirements can be eased by using so-called Z-scheme configurations in which a redox mediator A moves charge between physically separated semiconductors. Reproduced from ref. 15. Reprinted with permission. 5

Figure 1.3. Semiconductor energy levels a) in high vacuum conditions, b) in contact with a redox-active electrolyte before Fermi-level equilibration, and c) after Fermi-level equilibration. 6

Figure 1.4. Semiconductor energy levels in a) a photoelectrode in contact with a redox-active electrolyte and in Ohmic contact with a conductive (metallic) substrate; b) a particle suspended in redox-active electrolyte; and c) a particle with a metallic co-catalyst suspended in a redox-active electrolyte. 8

Figure 2.1. Incident and absorbed photon-to-current conversion efficiency for sputtered TiO_2 and $TiO_{2-x}N_x$ in 0.1 M NaOH at a potential of 0.7 V vs Ag/AgCl under backside (substrate-electrode interface) illumination. Reproduced with permission from ref. 17. Copyright 2004 American Chemical Society. 15

Figure 2.2. Schematic representation of the electronic structure of (a) pristine TiO_2; (b) TiO_2 doped with an acceptor atom; (c) TiO_2 co-doped with acceptor and donor atoms; (d) TiO_2 alloyed with donor atoms but dopes with acceptors, resulting in the formation of additional donor states below the CB; (e) TiO_2 co-alloyed with an acceptor and a donor whose energy levels reside within the original conduction band; and (f) TiO_2 co-alloyed with an acceptor and a donor whose energy levels reside below the original conduction band edge. Electronic transitions represented by dotted lines are not expected to result in mobile charge carriers. The band positions shown are based on anatase TiO_2. 17

Figure 2.3. IPCE spectra of TiO_2:N and TiTaON nanowire electrodes measured at 1.23 V vs. RHE in 1 M KOH electrolyte. The inset shows an enlargement of the visible light region. Adapted from ref. 44 with permission. Copyright 2012 American Chemical Society. 20

Figure 2.4. SIMS profile of a single TiWOC nanowire showing dopant concentration across the nanowire thickness. Adapted from ref. 45 with permission from Nature Publishing Group. 24

Figure 3.1. TEM images of a) dispersed TiNbON-25 nanoparticles, b) TiNbON-25 d_{101} spacing, and c) and d) 1 wt% RuO_2 loaded TiNbON-25. 35

Figure 3.2. O_2 evolution using 50 mg 1 wt% RuO_2 loaded TiNbON-25 powder, 30 mL of 1 mM $NaIO_3$, and 600 mW/cm^2 illumination by a 150 W Xe lamp, AM 1.5G filter (red). Inset. Control experiments (all under illumination): 1 mM IO_3^- only (black), 0.5 mg RuO_2 and 1 mM IO_3^- (blue), 1 wt% RuO_2 loaded TiNbON-25 (green), TiNbON-25 and 1 mM IO_3^- (orange). 36

Figure 3.3. Optimization of RuO_2 wt% on TiNbON-25, annealed at 350 °C for 1 hour. Reaction conditions: 50 mg loaded powder, 30 mL of 1 mM $NaIO_3$, 600 mW/cm^2 illumination by a 150 W Xe lamp, AM 1.5G filter. 37

Figure 3.4. a) Dependence of O_2 evolution after three hours of irradiation with cut-on filters for NbN-25 loaded with 1 wt% RuO_2 (red). The diffuse reflectance UV-Vis spectrum of TiNbON-25 is also shown (black). Reaction conditions: 50 mg catalyst, 1 mM $NaIO_3$ (30 mL), 150 W Xe lamp fitted with water filter and cut-on filters, and a custom-built Pyrex cell fitted with a quartz window. b) Oxygen evolution *vs*. irradiance for TiNbON-25 loaded with 1 wt% RuO_2. Reaction conditions: 50 mg catalyst, 1 mM $NaIO_3$ (30 mL), 150 W Xe lamp fitted with water filter and 295 nm cut-on filter, and a custom-built Pyrex cell fitted with a quartz window. 37

Figure 3.5. Oxygen evolution as a function of time for TiNbON-25 loaded with 1 wt% RuO_2 with different concentrations of $NaIO_3$ sacrificial acceptor. 37

Figure 3.6. Oxygen evolution as a function of time for freshly prepared TiNbON-25 loaded with 1 wt% RuO_2 (black line) and for a second run in which the catalyst was recycled (red line). Reaction conditions: 1 mM $NaIO_3$, 600 mW/cm^2, AM 1.5G filtered light. 39

Figure 4.1. PXRD patterns for $Ti_{1-x}Nb_xN$ prepared by urea-glass synthesis with tungsten powder added as an internal standard. Nb content increases from the top of the graph to the bottom. Black: $x = 0$; red: $x = 5$; blue: $x = 15$; green: $x = 25$; purple: $x = 30$. 46

Figure 4.2. Thermogravimetric analysis traces recorded in flowing air for $Ti_{1-x}Nb_xN$ compounds. Black: $x = 0$; red: $x = 5$; blue: $x = 15$; green: $x = 25$; purple: $x = 30$. 47

Figure 4.3. PXRD patterns for $Ti_{1-x}Nb_xN$ after oxidation in air (TiNbON-*x*). Black: *x* = 0; red: *x* = 5; blue: *x* = 15; green: *x* = 25; purple: *x* = 30. Gray and red reference patterns are anatase and rutile TiO_2, respectively. 48

Figure 4.4. Diffuse reflectance spectra for TiNbON-*x* compounds. Black: *x* = 0; red: *x* = 5; blue: *x* = 15; green: *x* = 25; purple: *x* = 30. Degussa P25 TiO_2 is shown in grey for reference. 49

Figure 4.5. First-order Langmuir-Hinshelwood rate constants for photochemical methylene blue degradation over TiNbON-*x* as a function of Nb concentration. Data are shown for reactions run with the full AM1.5G spectrum (black squares) and for AM1.5G modified by a 400 nm cut-on filter (red circles). Error bars shown are the error in the fit for the rate law for the average concentration vs. time data for two trials. 51

Figure 4.6. a) EPR spectra for TiNbON-0 (black, multiplied 5x) and TiNbON-5 (red). b) EPR spectrum for TiNbON-25. Spectra were acquired at a microwave frequency of 9.26 GHz at 120 K using a modulation frequency of 10 GHz. 52

Figure 5.1. PXRD patterns for TiNbON-15 prepared by Ca^{2+} urea-glass synthesis. a) Reactions carried out at 750 ºC and R = 0.7 (black), R = 0.1 (red). Vertical lines represent reference patterns for rutile TiO_2 (grey) and fersmite $CaNb_2O_6$ (blue). b) Reaction carried out at 500 ºC and R = 0.7. Grey vertical lines represent reference pattern for anatase TiO_2. 58

Figure 5.2. a) PXRD patterns for TiNbON-5 prepared at different *R*. b) Photographs of TiNbON prepared at different *R*. Left, *R* = 0.7 (black); middle, *R* = 0.5 (brown); right, *R* = 0.3 (grey). 59

Figure 5.3. Thermogravimetric analysis trace for TiNbON before acid washing (black) and after (red). Analysis was carried out in flowing air. 60

Figure 5.4. Scanning electron micrograph of TiNbON-5 prepared by Ca^{2+}-assisted urea-glass method after annealing at 400 ºC for 3 h. 61

Figure 5.5. Diffuse reflectance UV-Vis spectrum of TiNbON after acid wash before annealing (black) and after annealing (red). 62

Figure 5.6. Tauc plots for TiNbON before (black) and after (red) the annealing step. Part a) is the plot for indirect band gap, and part b) for direct. 63

Figure 5.7 63

Figure 5.8. Kinetics plot showing raw concentration data over time for methylene blue degradation experiments. Black squares: before annealing, red circles: after annealing. The rate constant is equal to the slope of the line of best fit through the points. 64

Figure 6.1. Cross-sectional scanning electron microscopy (left) and elemental mapping by energy dispersive x-ray spectroscopy (right) for WO_3 (top), BHJ-Cu (middle) and BHJ-CuNi (bottom) films. Legend: Sn, black; W, red; Cu, blue; Ni, green. 72

Figure 6.2. Linear sweep voltammograms in 0.1 M KBi with no additives (top), 0.2 M methanol (middle), and 0.2 M formate (bottom) for representative films. Dashed lines represent the current without illumination, and solid lines under illumination. Average values for photocurrent are shown in Table 1. Legend: WO_3, black; BHJ-Cu, red; BHJ-CuNi, blue. 73

Figure 6.3. Photochemical OER of WO_3 and BHJ films. a) j-t curves for WO_3 (black), BHJ-Cu (red), and BHJ-CuNi. b-d) Oxygen evolution versus time for the same 3 electrodes, respectively. Dotted lines represent expected O_2 at 100% Faradaic efficiency; solid lines represent actual measured O_2. 75

Figure 6.4. Schematic depicting favorable and unfavorable charge transport pathways during photochemical OER using BHJ-Cu (left) and BHJ-CuNi (right) photoanodes. 78

Figure A1. X-ray photoelectron spectra of N(1s) peak a) before and b) after annealing TiNbON-25 at 350 °C for 1 hour. N_i denotes interstitial nitrogen, N_S denotes substitutional nitrogen. 86

Figure A2. XRD of $RuCl_3$ annealed at 350 °C for 1 hour, yielding RuO_2 (JCPDF 70-2662). 87

Figure A3. Histogram of particle size for 100 randomly measured particles by SEM. 87

Figure A4. Diffuse reflectance UV-Vis spectroscopy of a) TiNbON-25 and b) TiNbON-25 loaded with 1 wt% RuO_2 and annealed at 350 °C for 1 hour, and c) 2 wt% RuO_2. 88

Figure A5. Temperature *vs.* time for a representative oxygen-evolution experiment. Reaction conditions: 50 mg catalyst, 1 mM $NaIO_3$ (30 mL), 150 W Xe lamp fitted with water filter and 295 nm cut-on filter (~ 600 mW/cm^2), and a custom built Pyrex cell fitted with a quartz window. 88

Figure B1. Urea-glass synthesis products prepared at different urea:valence ratios *R*, denoted here u:v. *: No Nb added. All other samples prepared using a metals ratio of $Ti_{0.85}Nb_{0.15}$. 89

Figure B2. Scanning electron micrographs of $Ti_{1-x}Nb_xN$ prepared by the urea-glass route: a) $x = 0$, b) $x = 5$, c) $x = 15$, d) $x = 25$, e) $x = 30$. Each sample shares a common scale bar. 90

Figure B3. Scanning electron micrographs of TiNbON-*x* prepared by the urea-glass route: a) $x = 0$, b) $x = 5$, c) $x = 15$, d) $x = 25$, e) $x = 30$. Each sample shares a common scale bar. 90

Figure B4. Linear fits for first-order Langmuir-Hinshelwood kinetics for a) full-spectrum and b) $\lambda \geq 400$ nm methylene blue degradation measurements. The slope of the fit line is the rate constant for the reaction. Black squares: TiNbON-0; red circles: TiNbON-5; blue up-triangles: TiNbON-15; green down-triangles: TiNbON-25; purple stars: TiNbON-30. 91

Figure C1. Schematic depiction of the spray pyrolysis apparatus used to synthesize pure-phase $CuWO_4$ and $Cu_{0.95}Ni_{0.05}WO_4$ films. 92

Figure C2. Powder x-ray diffraction patterns of sol-gel WO_3 (black), BHJ-Cu (red), and BHJ-CuNi films after synthesis and soaking in 0.5 M HCl. Inset: enlarged pattern between 25-40° 2θ, showing the appearance of $CuWO_4$ peaks for BHJ films. 93

Figure C3. Tauc plots for UV-Vis diffuse reflectance spectra of WO_3 and MWO_4 thin films. Legend: WO_3 (black), BHJ-Cu (red), BHJ-CuNi (blue), $CuWO_4$ (green), and $Cu_{0.95}Ni_{0.05}WO_4$ (violet). 93

Figure C4. Linear sweep voltammograms of WO_3 and BHJ electrodes in 0.1 M KBi with no additives (a), 0.2 M methanol (b), and 0.2 M formate (c) added. Dashed lines depict the current response under no illumination, solid lines from electrode-electrolyte (EE) illumination, and dotted lines from substrate-electrolyte (SE) illumination. Legend: WO_3 (black), BHJ-Cu (red), BHJ-CuNi (blue). 94

List of Appendices

Appendix A: Supporting Information for Chapter 3 **86**
Appendix B: Supporting Information for Chapter 4 **89**
Appendix C: Supporting Information for Chapter 6 **92**

Abstract

The focus of this thesis is to examine co-incorporation of cationic and anionic dopants simultaneously as a strategy for increasing visible light absorption in TiO_2. Co-incorporation has been well-studied theoretically as a viable mechanism for introducing low-energy transitions into the stable TiO_2 host lattice; the history and fundamental motivation for co-incorporation is examined here in detail. However, experimental preparations of co-doped and co-incorporated materials remain limited, and a general synthetic method that establishes rigorous control over both cationic and anionic dopant stoichiometry has yet to emerge.

In this work, TiO_2 co-incorporated with the charge-compensating pair Nb^{5+}/N^{3-} to form titanium niobium oxynitride (TiNbON) is prepared by three synthetic routes and its photochemical properties investigated.

First, TiNbON with 25% Nb is prepared by a traditional hydrolytic sol-gel method followed by high-temperature ammonolysis. The resultant material is modified with 1 wt % of RuO_2 and evaluated as a photochemical water oxidation catalyst in a solution of $NaIO_3$ sacrificial oxidant. Under 6 times the intensity of solar illumination (6 suns), TiNbON-25 produces oxygen via water oxidation at the rate of ~100 μmol h^{-1} g^{-1}. Water oxidation occurs regardless of excitation wavelength, though diminished proportionally to the material absorptivity at each wavelength. The rate constant exhibits a zero-order dependence on iodate. Finally, oxygen evolution experiments in ^{18}O-labeled water produce primarily $^{36}O_2$, suggesting that the dominant pathway for oxygen evolution is the coupling of two water molecules.

Secondly, we undertake a new synthetic preparation for TiNbON materials by adapting the urea-glass synthesis for metal nitrides. The reaction produces micron-sized particles of mixed-

metal titanium niobium nitride for a variety of niobium contents. These materials are then oxidized to form photoactive anatase/rutile TiNbON that absorbs visible light of $\lambda \leq 550$ nm. Contrary to previous results, the optimized material contains 8% Nb of total metals and degrades methylene blue with a first-order Langmuir-Hinshelwood rate constant of 0.704 h^{-1} under 5 suns illumination (0.595 h^{-1} when restricted to $\lambda \geq 400$ nm). Full compositional analysis of TiNbON-5 reveals an empirical formula of $Ti_{0.92}Nb_{0.08}O_{1.97}N_{0.03}$.

A further refinement of the urea-glass synthesis for TiNbON is presented in which the alkaline-earth cation Ca^{2+} is added to the synthesis to slow the rate of ammonia release during the initial heating step. TiNbON-5 prepared by this method exhibits superior visible light absorption to 600 nm. Tauc analyses of optical spectra suggest a direct band gap. TiNbON-5 produced by this route exhibits a superior first-order Langmuir-Hinshelwood rate constant of 1.785 h^{-1} under 5 suns solar irradiation. It is hypothesized that the material's improved properties are due to increased nitrogen content.

Finally, a preparation for layered transition metal tungstate/tungsten oxide (MWO_4/WO_3) photoanodes for photoelectrochemical water oxidation is presented. This strategy seeks to improve on the fundamental shortcomings of the well-studied photoanode material WO_3, namely its instability and propensity to participate in side reactions, by adding a more stable and chemoselective interface layer. The interface layers chosen for this study are $CuWO_4$ and $Cu_{0.95}Ni_{0.05}WO_4$. The photoelectrochemical reactivity of MWO_4/WO_3 electrodes does not change appreciably with respect to bare WO_3. Furthermore, we introduce α-thujone, a water-soluble organic molecule with the potential to report on radical chemistry near an electrode surface. Experiments including α-thujone suggest decreased radical prevalence near the surface of MWO_4/WO_3 compared to WO_3.

Chapter 1
Introduction

1.1 Future Energy Demands Necessitate Renewable Sources and Storage

Global energy demand is skyrocketing. The world population continues to increase, and countries that were formerly not widely industrialized are developing. The number of people drawing from power grids worldwide is larger each day. The total demand for electricity on earth is projected to exceed 47.9 PWh (173 EJ/year) by 2050.[1-3]

Currently, the majority of electrical power on earth is generated by combusting fossil fuels. Strong evidence exists that fossil fuel use drives anthropogenic climate change, which has warmed the surface of the earth by ~1 ºC over pre-industrial averages.[4] Drastic and prompt action is needed to reduce fossil fuel use if the unpredictable effects of climate change are to be diverted.

The further political and environmental ramifications of fossil fuel use are shrouded in discourse to the effect that fossil fuels – somehow – remain the most economically viable option for energy generation. Pro-fossil fuel studies contend that there is enough coal, oil, and natural gas available to power civilization for several centuries.[5] These projections merely delay the inevitable. Natural sources of fossil fuels were created over millennia of biological and geological activity. Climate effects notwithstanding, no matter how many new reserves are discovered and harvested, the rate of fossil fuel consumption will always vastly outstrip the rate of generation. Renewable energy sources are necessary to sustain a growing and industrializing society.

Of the renewable energy sources under study, solar energy is particularly attractive. Sunlight strikes the earth's surface with a radiant power 430 EJ/h, meaning that the hypothetical 2050 society would need to harness just 0.005% to power their civilization.[5] In other words, enough sunlight reaches earth in under 1 hour to power all of society's energy consumption for 1 year.

Solar electricity generation, like many renewables, is inherently intermittent. Peak demand for electricity (6-8 pm across much of the United States, for example)[6] and peak solar irradiance (noon-3 pm) are misaligned, resulting in power shortages at night and the potential for grid overload during the middle of the day.[7]

The field of solar energy storage arose to meet this fundamental challenge. A wide variety of solar energy storage reactors have been proposed; discussing their merits and drawbacks is beyond the scope of this dissertation. The reactors under study herein convert energy in electromagnetic radiation to chemical energy by using incident solar radiation to excite a semiconductor, which supplies an electrical voltage that powers a fuel-forming chemical reaction. The result is a stable fuel product that can be stored and used on-demand.

1.2 Water Splitting as an Example of Solar Energy Storage

Solar energy storage is often illustrated in terms of water splitting, a redox process by which water is converted into its constituent elements, hydrogen and oxygen. In the cathodic process, two protons are reduced by one electron each and form a bond to create a molecule of hydrogen gas; this is termed the hydrogen evolution reaction (HER, reaction 1). The anodic process, the oxygen evolution reaction (OER, reaction 2), occurs when a molecule of water is oxidized by four electrons to form half of an oxygen molecule. Part of the energy used to drive the reaction is stored in the H-H bond of hydrogen.

(1) $2\ H^+ + 2\ e^- \rightarrow H_{2(g)}$ $\quad E^o_{cat} = 0.0$ V vs. NHE

(2) $O_{2(g)} + 4\ H^+ + 4\ e^- \rightarrow 2\ H_2O_{(l)}$ $\quad E^o_{an} = 1.23$ V vs. NHE

(3) $2\ H_2O \rightarrow 2\ H_{2(g)} + O_{2(g)}$ $\quad E^o_{cell} = -1.23$ V vs. NHE

Water splitting (reaction 3) powerfully illustrates the concept of solar energy storage. Hydrogen makes an attractive fuel due to a high gravimetric energy density of 142 kJ/g. Combusting hydrogen in air produces water in the reverse of reaction 3, resulting in an atom-

economic, carbon-neutral cycle of energy storage and use. While hydrogen's low volumetric energy density, difficulties presented by its transport and storage, and overall potential as an explosive hazard may limit its practical use by consumers,[8] water splitting provides a quintessential example of a clean energy economy and remains a motivator for active materials development projects.

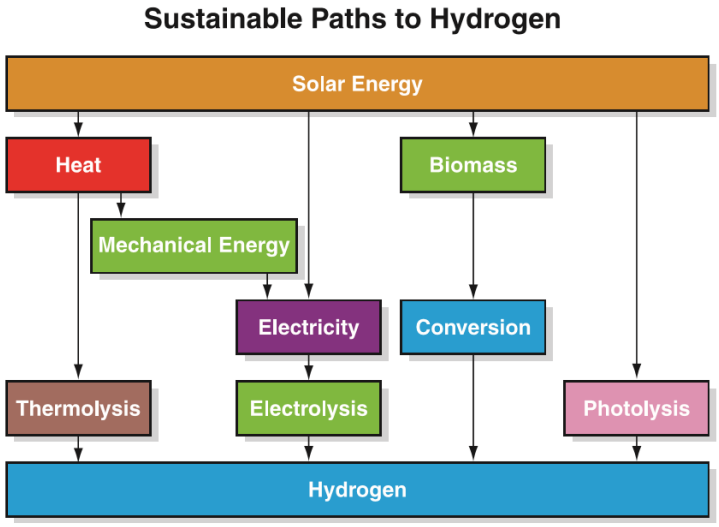

Figure 1.1. Schematic representation of various solar-to-hydrogen schemes which can involve water splitting. Reproduced from ref. 3. Reprinted with permission.

Generally speaking, a water splitting device need only harness the energy present in solar radiation and supply it to a catalyst immersed in aqueous solution. This can be achieved with a number of known technologies, as illustrated in Figure 1.1.[3] Which water splitting configuration will result in the most efficient energy storage device – or even a commercializable one – remains to be seen. The present work will discuss water splitting using photochemical (PC) and photoelectrochemical (PEC) cells; this limitation in scope is based on particular scientific interest and is not intended to reflect the superiority of such technologies. In a PC system, free-standing particulate matter absorbs light and supplies redox equivalents to a chemical reaction with no external voltage. A PEC system is distinguished by an active material immobilized on a conductive substrate to form an electrode to which a bias can be applied.

This work will also endeavor to advance water splitting research using inorganic semiconductors as light absorbers. The most familiar example of a light-absorbing inorganic semiconductor is crystalline silicon, the material that makes up traditional photovoltaic solar cells.

Binary compounds of main group elements, such as CdTe and GaAs, are also very well-studied as photovoltaics.[9] However, despite these photovoltaic compounds' abilities to strongly absorb light and rapidly transport charge, they cannot function in PC or PEC cells due to instability in aqueous solution. The failure mechanism of main group semiconductors – and indeed most non-oxide semiconductor materials – is the material's oxidation upon exposure to aqueous conditions accompanied by the formation of an insulating oxide layer and/or corrosion of the material.[10-12] Research in P(E)C water splitting has focused primarily on semiconducting transition metal oxides. While transition metal oxides generally absorb light less strongly and are less conductive, their superior stability along with higher raw material abundance has made them attractive research targets.

1.3 General Considerations for Semiconductor Photocatalysts

From the perspective of a laboratory chemist, semiconductor water splitting systems must simultaneously demonstrate 1) *in operando* chemical stability for years, 2) strong absorption in the visible region of the solar spectrum, 3) long excited state charge carrier lifetimes such that the rate of charge migration to particle surfaces and into solution outstrips the sum of recombination rates, and 4) fast and selective surface kinetics for both HER and OER. The stability consideration is typically beyond the scope of research chemistry, requiring sophisticated accelerated testing equipment and prototype devices to acquire meaningful data.

Upon absorbing a photon, an electron in a semiconductor is promoted from an occupied ground state, typically the valence band (VB), to an unoccupied excited state, usually the conduction band (CB). Promoting the electron leaves behind a reactive hole (h^+) in the valence band. The excited electrons and holes serve as the reducing equivalents and oxidizing equivalents (respectively) that drive water splitting. A semiconductor that absorbs a greater number of photons will create a greater number of oxidizing and reducing equivalents, resulting in a higher rate for both reactions. Therefore, when considering devices that operate using solar radiation as input, it is critical to harness visible wavelengths simply because a higher flux of these photons strikes the earth's surface.

The range of energies of electromagnetic radiation that a semiconductor can absorb is controlled by the difference in potential of its valence band maximum (VBM) and conduction band minimum (CBM). The energy gap between the VBM and CBM is referred to as the band gap, E_g.

In the types of highly ionic oxide semiconductors under study here, the filled VB states near the VBM are typically comprised of O(2p) orbitals, though in transition metal oxides some metal d character is observed as well.[13] States in the CB near the CBM originate from empty transition metal d states. However, it is not generally true that semiconductor band gaps can be predicted by referencing the vacuum energy levels of constituent ions. Because electronic states evolve both as a function of energetic and spatial overlap, the crystal structure of a semiconductor is also a prime determinant of its band gap. Therefore, strategies for tuning semiconductor band gaps typically involve beginning from a known material and modifying it systematically. Generally, the ideal band gap of a semiconductor photocatalyst is larger than that of a photovoltaic device and depends on the reaction for which the photocatalyst is intended. In the example of water splitting, the ideal band gap appears to be near 2.0 eV, as shown in Figure 1.2.[14] Electrons and holes in the semiconductor must have enough energy to overcome the standard cell potential for water splitting (1.23 eV) as well as the typical overpotentials for HER and OER (≥ 0.1 eV and ≥ 0.4 eV, respectively).[15]

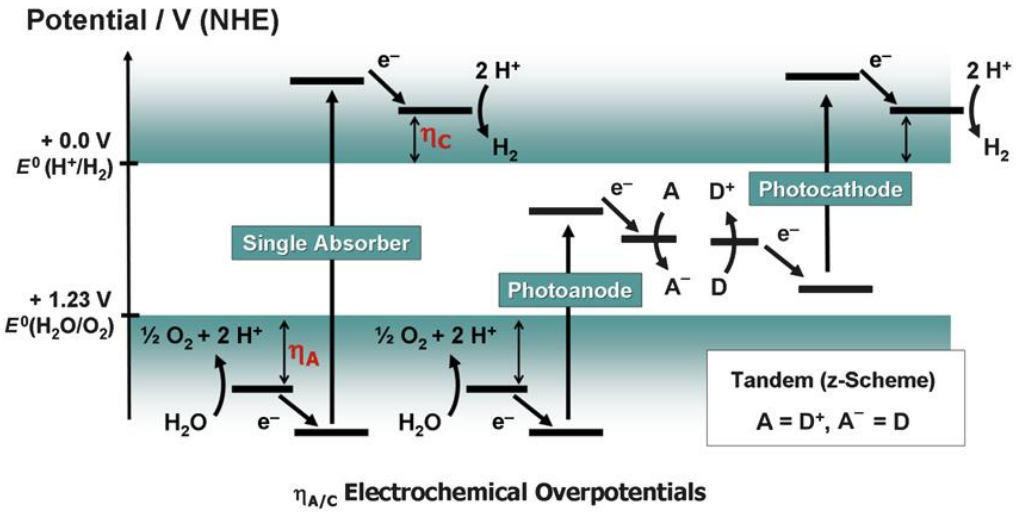

Figure 1.2. A minimum band gap is imposed by the reduction potentials for HER and OER along with associated overpotentials (η) for those reactions. The requirements can be eased by using so-called Z-scheme configurations in which a redox mediator A moves charge between physically separated semiconductors. Reproduced from ref. 15. Reprinted with permission.

The third requirement, that semiconductors conduct charges to the particle/solution interface faster than those charges recombine, merits some discussion. In developing semiconductor photocatalysts, scientists have harnessed the intrinsic property of semiconductors to equilibrate electrically with their environment, known as Fermi level equilibration.[16,17] In the

absence of Fermi level equilibration (i.e. high vacuum conditions), electrons and holes diffuse through a semiconductor crystal randomly by diffusion alone. Diffusion provides no driving force for the electron and hole, which are electrostatically attracted, to separate, so recombination is prominent. In typical operating conditions, Fermi level equilibration leaves the semiconductor with a permanent internal electric field which can move the oppositely-charged carriers away from one another with greater efficiency.

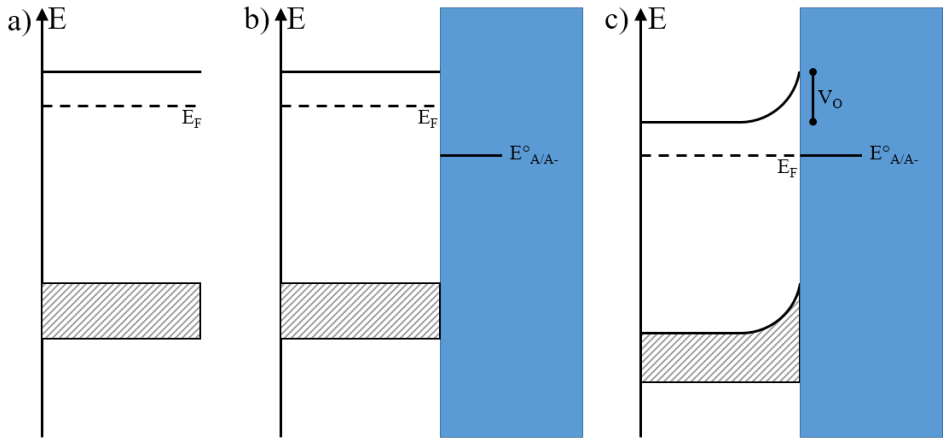

Figure 1.3. Semiconductor energy levels a) in high vacuum conditions, b) in contact with a redox-active electrolyte before Fermi-level equilibration, and c) after Fermi-level equilibration.

Figure 1.3 shows the example of Fermi level equilibration for an n-type semiconductor equilibrating with a solution redox couple A/A_{red}. The semiconductor's Fermi level (E_F), which for an n-type semiconductor sits close to the CBM, is in this example more negative than the E^o for A/A_{red}. In this case, Fermi level equilibration follows the case of a Schottky barrier. When the semiconductor is immersed in solution before Fermi level equilibration, an electrical potential develops across the semiconductor/solution interface. Electrons flow from the semiconductor into solution as a response to the potential, resulting in a positive shift in the semiconductor E_F. When the E_F equals $E^o_{A/Ared}$, Fermi level equilibration is complete.

The flow of electrons into solutions results in negatively-charged species accumulating near the semiconductor surface. As such, ionizable species (donors) within the semiconductor near the surface ionize, and positively-charged species accumulate near the semiconductor/solution interface. This capacitive interface is known as the space-charge layer or depletion layer and has a defined width W, which is related to the semiconductor donor and acceptor density by Equation 4, where V_O is the resultant internal electric field of the semiconductor (built-in voltage), N_A and

N_D are the density of acceptors and donors respectively, ε is the material permittivity, and q is the elementary charge.

$$(4)\ W = \sqrt{\frac{2\varepsilon}{q} V_O \left(\frac{1}{N_A} + \frac{1}{N_D}\right)}$$

Critical to photocatalysis, the equilibrated semiconductor's bands are now "bent" to more positive energy. Negatively-charged adsorbates induce an electric field within the semiconductor that draws positive valence band holes in the depletion layer rapidly towards the surface. However, electrons are not attracted to the surface and so tend to remain outside the depletion layer in the material bulk. As a result, holes become spatially separated from electrons as they are conducted in opposite directions by the internal electric field, and bulk charge recombination is reduced.

Lastly, considerations of surface kinetics for HER and OER are largely empirical. It is considerably more difficult to observe reaction intermediates and conclude step-by-step mechanistic cycles in heterogeneous catalysis compared to homogeneous catalysis. Furthermore, research in heterogeneous water splitting has moved away from single-phase systems to absorber-catalyst tandem systems in which the semiconductor functions only as a light absorber that conducts charge to otherwise inactive electrocatalysts attached to the particle surface. Kinetic investigations are typically carried out on the electrocatalysts alone, and it is assumed that the details of their function do not change upon their attachment to the semiconductor. This decoupled development allows for the separate – and more practical – optimization of different device components for individual functions.

Semiconductor photocatalysts in both photoelectrochemical and photochemical systems can take advantage of an electrocatalyst increasing rate and selectivity for the reaction of interest. However, there is an additional concern of relevance for photochemical systems as highlighted in Figure 1.4. In the example n-type photoanode shown, electrons are drawn away from the semiconductor/solution interface first by the Schottky barrier as discussed above, then by the Ohmic contact with the photoanode substrate. This architecture provides continually descending energy levels for photogenerated electrons and accelerates their extraction from the photoanode to the external circuit. Concurrently, holes are swept in the opposite direction and their injection to solution is facilitated. The electronic structure shown develops in a photoanode whether an electrocatalyst is present or not.

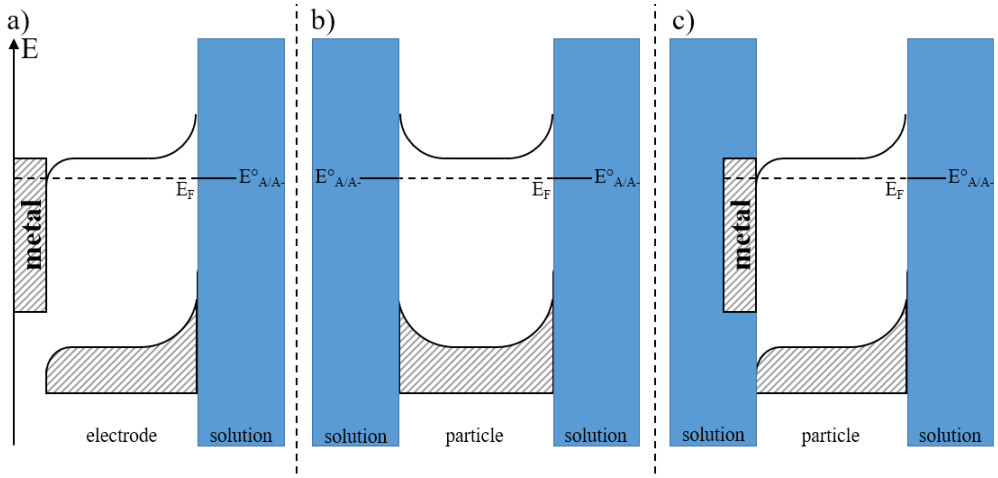

Figure 1.4. Semiconductor energy levels in a) a photoelectrode in contact with a redox-active electrolyte and in Ohmic contact with a conductive (metallic) substrate; b) a particle suspended in redox-active electrolyte; and c) a particle with a metallic co-catalyst suspended in a redox-active electrolyte.

Photochemical systems, however, do not have a "back contact" substrate to extract electrons. In the absence of an electrocatalyst, a semiconductor particle in solution develops a depletion layer around the entire particle surface. As such, hole transfer to solution is facilitated in every direction, but electrons are only ever driven towards the particle bulk, impeding the particle's ability to perform both half reactions of a redox cell. Adding a metallic co-catalyst creates a region at the surface where electron transfer is favorable, creating an electronic structure more similar to that of the photoanode and facilitating transfer for both electrons and holes.

1.4 Notable Photochemical and Photoelectrochemical Systems

The first reports of PEC water oxidation appeared in 1972 with Fujishima and Honda's description of a TiO_2 electrode that evolved oxygen gas under the action of an electrical voltage and illumination.[18] Since that seminal paper, TiO_2 has been arguably the most intimately-studied material for water splitting applications.[19-21] TiO_2 commonly crystallizes in one of two polymorphs; the low-temperature anatase phase has a slightly higher band gap of 3.2 eV compared to the high-temperature rutile phase's 3.0 eV. Water splitting systems employing TiO_2 have generally demonstrated higher activity when the anatase phase is used. Luttrell et al. recently demonstrated the superior charge transport properties of the anatase phase by comparing epitaxially grown anatase and rutile TiO_2 thin films.[22]

High-aspect nanotube electrodes are the state of the art for TiO_2 photoelectrodes and were reviewed extensively in 2009 by Shankar, et al.[21] Incident photon to current conversion efficiencies (IPCE) of as high as 80% have been reported for pure nanotube TiO_2 electrodes under ultraviolet radiation;[23] however, as previously mentioned, the wide TiO_2 band gap precludes visible light activity and, thus, application to suitably efficient solar water splitting. Strategies for modifying TiO_2 in PC and PEC systems will be covered in detail in Chapter 2 of this thesis.

WO_3 has also been extensively studied for PEC water oxidation. The first report of a WO_3 photoanode appeared in 1977, shortly after Fujishima and Honda described their TiO_2 photoanode.[24] WO_3 has a significantly smaller band gap of 2.7 eV compared to TiO_2, resulting in its ability to absorb some blue wavelengths of the visible spectrum. However, WO_3's comparatively low CBM energy of 0.2 eV vs. NHE precludes its application to PC water splitting because photogenerated electrons do not have enough potential to perform the HER.[10] PEC systems based on WO_3 have realized high photocurrents (~5 mA/cm^2),[25,26] but encounter some limitations based on WO_3's fundamental chemistry. WO_3, being an Arrhenius acidic oxide, is stable only in strongly acidic solutions where Nernstian shifts in reduction potential make water oxidation thermodynamically more expensive. WO_3 is also known to indiscriminately oxidize a wide range of common acid anions during water oxidation.[27,28] It is hypothesized that the hydroxyl radical •OH, formed by the reaction between surface water and WO_3's highly oxidizing valence band holes, reacts rapidly to oxidize these anions and kinetically out-competes water oxidation to result in the accumulation of side products.[27,29]

To circumvent the selectivity and stability issues using bare WO_3, a wide variety of electrocatalytic or insulating layers have been applied. Insulating layers such as Al_2O_3 provide a chemically stable coating that is thin enough to allow charges to pass through by quantum mechanical tunneling.[30] Electrocatalytic layers such as cobalt phosphate,[31] nickel borate,[32] metal oxyhydroxides,[33] and others improve overall charge transfer by improving charge separation and reaction rate for OER. Insulating and electrocatalytic layers alike have also been shown to reduce recombination rates by passivating surface recombination sites.

1.5 Scope of this Thesis

The work presented herein seeks to advance co-doped TiO_2 as a viable material for visible light-promoted catalysis. TiO_2, as an abundant metal oxide that is highly stable in aqueous

conditions and is known to catalyze a variety of reactions, still remains an attractive research target nearly half a century after its ability to promote water splitting was discovered.

Co-doping can potentially address the main drawback of TiO_2-based systems, which is their inability to absorb visible light. Co-doped TiO_2 will be reviewed in detail in Chapter 2. Briefly, the goal of most co-doping approaches is to substitute some anions (O^{2-}) for another anion with filled orbitals more positive in energy, typically N^{3-} or C^{4-}. Simultaneously, to compensate the extra negative charge added to the parent lattice, a higher-valent metal cation must be substituted for some of the material's cations, e.g. Nb^{5+} or W^{6+} in place of Ti^{4+}. The higher-energy filled states introduced by the dopant anions have the effect of decreasing the apparent E_g and inducing visible light absorption, while the high-valent dopant cation passivates electronic defect states that are introduced by excess negative charge.

While the hypothesis of co-doping is established, precise control of dopant ratios during material synthesis is necessary.[34] Such an achievement remains elusive. The work presented in this thesis deals primarily with exploring new reaction pathways to preparing TiO_2 doped with Nb^{5+} and N^{3-}, referred to herein as TiNbON. This compositional system has been explored by our laboratory and others.[35-40] Generally, Nb^{5+} composition is easily controlled through the use of metal halide or alkoxide reactants, but N^{3-} is introduced through gas-phase nitridation reactions for which compositional control is more difficult. The work presented here emphasizes synthesis and compositional analysis in an attempt to establish control over dopant ratios in the TiNbON system.

1.6 References

(1) World Energy Council 2013, World Energy Scenarios: Composing Energy Futures to 2050, London 2013.

(2) Lewis, N. S.; Nocera, D. G. Powering the Planet: Chemical Challenges in Solar Energy Utilization. *Proc. Natl. Acad. Sci.* **2006**, *103* (43), 15729–15735.

(3) Turner, J. A. A Realizable Renewable Energy Future. *Science* **1999**, *285* (5428), 687–689.

(4) Stocker, T.F.; Qin, D.; Plattner, G. -K.; Tignor, M.; Allen, S. K.; Boschung, J.; Nauels, A.; Xia, Y.; Bex, V.; Midgley, P. M. (eds.) *Climate Change 2013: The Physical Science Basis. Contribution of Working Group I to the Fifth Assessment Report of the Intergovernmental Panel on Climate Change*. **2013**, IPCC. Cambridge University Press, Cambridge, United Kingdom and New York, NY, USA, 1535 pp.

(5) United Nations Development Program (2003). World Energy Assessment Report: Energy and the Challenge of Sustainability (United Nations, New York).

(6) U.S. Electric System Operating Data. United States Energy Information Administration. https://www.eia.gov/beta/realtime_grid/?src=l2#/summary/demand?end=20160725&start=20160625

(7) Trotochaud, L.; Young, S. L.; Ranney, J. K.; Boettcher, S. W. *J. Am. Chem. Soc.* **2013**, *136*, 6744–6753.
(8) Tseng, P.; Lee, J.; Friley, P. A Hydrogen Economy: Opportunities and Challenges. *Energy* **2005**, *30* (14), 2703–2720.
(9) Polman, A.; Knight, M.; Garnett, E. C.; Ehrler, B.; Sinke, W. C. Photovoltaic Materials: Present Efficiencies and Future Challenges. *Science* **2016**, *352* (6283), aad4424-aad4424.
(10) Kudo, A.; Miseki, Y. Heterogeneous Photocatalyst Materials for Water Splitting. *Chem. Soc. Rev.* **2009**, *38* (1), 253–278.
(11) Maeda, K.; Domen, K. New Non-Oxide Photocatalysts Designed for Overall Water Splitting under Visible Light. *J. Phys. Chem. C* **2007**, *111* (22), 7851–7861.
(12) Ellis, A. B.; Kaiser, S. W.; Bolts, J. M.; Wrighton, M. S. Study of N-Type Semiconducting Cadmium Chalcogenide-Based Photoelectrochemical Cells Employing Polychalcogenide Electrolytes. *J. Am. Chem. Soc.* **1977**, *99* (9), 2839–2848.
(13) Xu, Y.; Schoonen, M. A. A. The Absolute Energy Positions of Conduction and Valence Bands of Selected Semiconducting Minerals. *Am. Mineral.* **2000**, *85*, 543–556.
(14) Osterloh, F. E.; Parkinson, B. A. Recent Developments in Solar Water-Splitting Photocatalysis. *MRS Bull.* **2011**, *36* (1), 17–22.
(15) McCrory, C. C. L.; Jung, S.; Peters, J. C.; Jaramillo, T. F. Benchmarking Heterogeneous Electrocatalysts for the Oxygen Evolution Reaction. *J. Am. Chem. Soc.* **2013**, *135*, 16977–16987.
(16) Nozik, A. J.; Memming, R. Physical Chemistry of Semiconductor−Liquid Interfaces. *J. Phys. Chem.* **1996**, *100* (31), 13061–13078.
(17) Elementary solid state phyics M. Ali Omar Chapter 7 I think?
(18) Fujishima, A.; Honda, K. Electrochemical Photolysis of Water at a Semiconductor Electrode. *Nature* **1972**, *238* (5358), 37–38.
(19) Schneider, J.; Matsuoka, M.; Takeuchi, M.; Zhang, J.; Horiuchi, Y.; Anpo, M.; Bahnemann, D. W. Understanding TiO_2 Photocatalysis: Mechanisms and Materials. *Chem. Rev.* **2014**, *114* (19), 9919–9986.
(20) Chen, X.; Mao, S. S. Titanium Dioxide Nanomaterials: Synthesis, Properties, Modifications, and Applications. *Chem. Rev.* **2007**, *107* (7), 2891–2959.
(21) Shankar, K.; Basham, J. I.; Allam, N. K.; Varghese, O. K.; Mor, G. K.; Feng, X.; Paulose, M.; Seabold, J. A; Choi, K.-S.; Grimes, C. A. Recent Advances in the Use of TiO_2 Nanotube and Nanowire Arrays for Oxidative Photoelectrochemistry. *J. Phys. Chem. C* **2009**, *113* (16), 6327–6359.
(22) Luttrell, T.; Halpegamage, S.; Tao, J.; Kramer, A.; Sutter, E.; Batzill, M. Why Is Anatase a Better Photocatalyst than Rutile?--Model Studies on Epitaxial TiO_2 Films. *Sci. Rep.* **2014**, *4*, 4043.
(23) Varghese, C. K.; Paulose, M.; Shankar, K.; Mor, G. K.; Grimes, C. A. Water-Photolysis Properties of Micron-Length Highly-Ordered Titania Nanotube-Arrays. *J. Nanosci. Nanotechnol.* **2005**, *5*, 1158-1165.
(24) Butler, M. A. Photoelectrolysis and Physical Properties of the Semiconducting Electrode WO_3. *J. Appl. Phys.* **1977**, *48* (5), 1914–1920.
(25) Kim, J. K.; Shin, K.; Cho, S. M.; Lee, T.-W.; Park, J. H. Synthesis of Transparent Mesoporous Tungsten Trioxide Films with Enhanced Photoelectrochemical Response: Application to Unassisted Solar Water Splitting. *Energy & Environmental Science*, 2011, *4*, 1465.
(26) Santato, C.; Odziemkowski, M.; Ulmann, M.; Augustynski, J. Crystallographically Oriented Mesoporous WO_3 Films: Synthesis, Characterization, and Applications. *J. Am. Chem. Soc.* **2001**, *123* (43), 10639–10649.
(27) Mi, Q.; Zhanaidarova, A.; Brunschwig, B. S.; Gray, H. B.; Lewis, N. S. A Quantitative Assessment of the Competition between Water and Anion Oxidation at WO_3 Photoanodes in Acidic Aqueous Electrolytes. *Energy Environ. Sci.* **2012**, *5* (2), 5694.
(28) Hill, J. C.; Choi, K.-S. Effect of Electrolytes on the Selectivity and Stability of N-Type WO_3 Photoelectrodes for Use in Solar Water Oxidation. *J. Phys. Chem. C* **2012**, *116* (14), 7612–7620.

(29) Leaustic, A.; Babonneau, F.; Livage, J. Photoreactivity of WO_3 Dispersions: Spin Trapping and Electron Spin Resonance Detection of Radical Intermediates. *J. Phys. Chem.* **1986**, *90*, 4193–4198.
(30) Kim, W.; Tachikawa, T.; Monllor-Satoca, D.; Kim, H.; Majima, T.; Choi, W. Promoting Water Photooxidation on Transparent WO_3 Thin Films Using an Alumina Overlayer. *Energy Environ. Sci.* **2013**, *6* (12), 3732.
(31) Seabold, J. A.; Choi, K. S. Effect of a Cobalt-Based Oxygen Evolution Catalyst on the Stability and the Selectivity of Photo-Oxidation Reactions of a WO_3 Photoanode. *Chem. Mater.* **2011**, *23* (5), 1105–1112.
(32) Seabold, J. A.; Choi, K. -S. *J. Am. Chem. Soc.* **2012**, *134*, 2186–2192.
(33) Lhermitte, C. R.; Verwer, J. G.; Bartlett, B. M. Improving the Stability and Selectivity for the Oxygen-Evolution Reaction on Semiconducting WO_3 Photoelectrodes with a Solid-State FeOOH Catalyst. *J. Mater. Chem. A* **2016**, *4* (8), 2960–2968.
(34) Brancho, J. J.; Bartlett, B. M. Challenges in Co-Alloyed Titanium Oxynitrides, a Promising Class of Photochemically Active Materials. *Chem. Mater.* **2015**, *27* (21), 7207–7217.
(35) Breault, T. M.; Bartlett, B. M. Composition Dependence of TiO_2:(Nb,N)-X Compounds on the Rate of Photocatalytic Methylene Blue Dye Degradation. *J. Phys. Chem. C* **2013**.
(36) Breault, T. M.; Brancho, J. J.; Guo, P.; Bartlett, B. M. Visible Light Water Oxidation Using a Co-Catalyst Loaded Anatase-Structured $Ti_{1-(5x/4)}Nb_xO_{2-y-\delta}N_y$ Compound. *Inorg. Chem.* **2013**, *52* (16), 9363–9368.
(37) Breault, T. M.; Bartlett, B. M. Lowering the Band Gap of Anatase-Structured TiO_2 by Coalloying with Nb and N: Electronic Structure and Photocatalytic Degradation of Methylene Blue Dye. *J. Phys. Chem. C* **2012**, *116* (10), 5986–5994.
(38) Chadwick, N. P.; Glover, E. N. K.; Sathasivam, S.; Basahel, S. N.; Althabaiti, S. a.; Alyoubi, A. O.; Parkin, I. P.; Carmalt, C. J. Photo-Activity and Low Resistivity in N/Nb Co-Doped TiO_2 Thin Films by Combinatorial AACVD. *J. Mater. Chem. A* **2016**, 407–415.
(39) Cottineau, T.; Béalu, N.; Gross, P.-A.; Pronkin, S. N.; Keller, N.; Savinova, E. R.; Keller, V. One Step Synthesis of Niobium Doped Titania Nanotube Arrays to Form (N,Nb) Co-Doped TiO_2 with High Visible Light Photoelectrochemical Activity. *J. Mater. Chem. A* **2013**, *1* (6), 2151–2160.
(40) Marchiori, C.; Di Liberto, G.; Soliveri, G.; Loconte, L.; Lo Presti, L.; Meroni, D.; Ceotto, M.; Oliva, C.; Cappelli, S.; Cappelletti, G.; Aieta, C.; Ardizzone, S. Unraveling the Cooperative Mechanism of Visible-Light Absorption in Bulk N,Nb Codoped TiO_2 Powders of Nanomaterials. *J. Phys. Chem. C* **2014**, *118* (41), 24152–24164.

Chapter 2

Previous Studies Furthering Single Ion and Co-doping in TiO_2

Portions of this chapter have been published:

Brancho, J. J.; Bartlett, B. M. *Chem Mater*. **2015**, *27* (21), 7207–7217.

2.1. Modifying Titanium Dioxide by Single Ion Doping

To date, no single-phase material has shown the requisite activity for implementation as a commercial energy solution. With few exceptions, transition metal oxides are hindered either by wide band gaps that limit solar absorption to ultraviolet light or by partially-filled d-shells that effect low charge carrier mobility.[1-3]

TiO_2 is an attractive potential industrial material due to its durability, an impressive versatility of available syntheses, and the relative crustal abundance of Ti among transition metals.[4-6] Its CBM and VBM potentials enable it to drive a variety of desirable reactions photochemically, including water splitting. The main limitation in TiO_2 is a band gap energy of 3.2 eV (anatase) or 3.0 eV (rutile), restricting TiO_2 to an ultraviolet photocatalyst. Attempts to produce a visible light-active titania began with singly-doping the material, either with a cation on a Ti^{4+} site or with an anion on an O^{2-} site.

Cationic doping of TiO_2 has largely focused on first-row transition metals in various oxidation states.[7,8] Transition metal-doped TiO_2 materials have not been widely successful as visible light photocatalysts. For example, Serpone *et al.* prepared TiO_2 doped with Cr^{3+}, Fe^{3+}, and

V^{5+}, and measured their photoconductivity and photochemistry relative to pure TiO_2.[9] Although the compounds displayed high activity for more kinetically facile reactions (oxalic acid oxidation coupled with HER), their ability to generate hydrogen via photochemical water splitting was diminished in the case of TiO_2:Cr^{3+} or eliminated completely for TiO_2:Fe^{3+} and TiO_2:V^{5+}. The visible light excitations were attributed to dopant metal crystal-field transitions; the octahedral-field t_{2g} and e_g orbital sets for these transition metal dopants lie within the TiO_2 midgap region and so can easily trap photogenerated charges.

It is widely observed that metals with partially-filled d-shells, whether incorporated as dopants or stoichiometrically, facilitate charge carrier recombination by acting as trap sites. However, a number of cation-doped systems have demonstrated increased photochemical activity under ultraviolet excitation relative to TiO_2, particularly when doped with Fe^{3+}. It has been suggested that Fe^{3+}-doped catalysts are uniquely effective among cation-doped TiO_2 due to the ability of Fe^{3+} to serve as a shallow trap for both electrons and holes.[7] Also, an important relationship exists between the Fe^{3+} loading in the photocatalyst and the size of the host particle. Zhang *et al*. prepared several Fe^{3+}-doped TiO_2 materials of various particle sizes and measured their photoactivity for chloroform oxidation, finding a different optimum Fe^{3+} loading for each particle size.[10] In smaller particles charge carrier recombination at the particle surface becomes a dominant loss pathway; Fe^{3+} doping slows the migration of excited charge carriers towards the surface, thereby reducing the rate of surface recombination. However, if Fe^{3+} is doped in beyond the optimum concentration (< 1 at% as found by Zhang et al.), the charge carrier mobility decreases critically as they are trapped more often en route to the surface. Optical spectra of TiO_2 doped at ~1 at % with Fe^{3+} do not display strong enough visible light absorption to act as solar photocatalysts.[7] More recently, Berglund et al. carried out a high-throughput screening of transition metal dopants for TiO_2 and their effect on photoelectrochemical dye-sensitized solar cell carrier collection efficiency and photovoltage, showing that only a small number of cations positively impacted performance.[11]

Anionic doping of TiO_2 produced a body of work that has been influential in guiding oxynitride and co-alloyed material engineering. The first major report of an active anion-doped TiO_2 photocatalyst was published in 2001.[12] The nitrided $TiO_{2-x}N_x$ published by Asahi *et al.* showed visible light absorption out to wavelengths of 500 nm and, driven by visible light

excitation, degraded methylene blue dye and acetaldehyde gas. Formed by sputtering TiO_2 in a 40% N_2 atmosphere, the $TiO_{2-x}N_x$ had a nitrogen content of 1.0-1.4 at %. The field of anion-doped TiO_2 blossomed with more reports of N-doped titania as well as C-doped titania and S-doped titania. Anion-doped TiO_2 has been extensively reviewed elsewhere.[5,6,8,13,14]

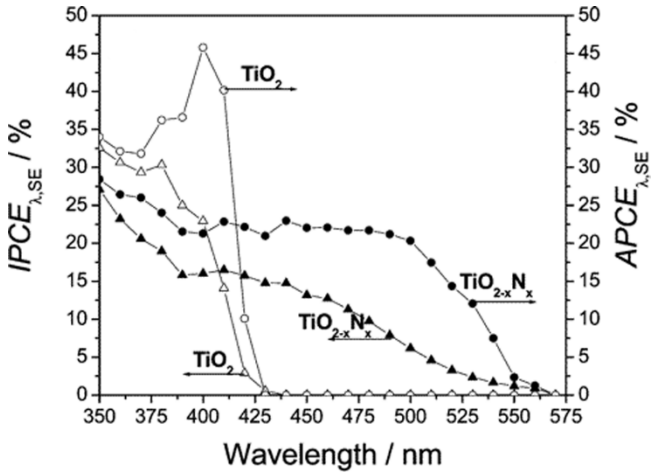

Figure 2.1. Incident and absorbed photon-to-current conversion efficiency for sputtered TiO_2 and $TiO_{2-x}N_x$ in 0.1 M NaOH at a potential of 0.7 V vs Ag/AgCl under backside (substrate-electrode interface) illumination. Reproduced with permission from ref. 17. Copyright 2004 American Chemical Society.

Although anion-doping TiO_2 has been more successful in creating visible light-active photocatalysts, these singly-doped systems suffer from inefficient internal charge transport. Experimentally, this inefficiency has been verified for N-doped TiO_2 by observations of decreased photoconductivity and decreased photon-to-current conversion efficiency under ultraviolet irradiation relative to unmodified TiO_2.[15-17] For example, Romualdo Torres *et al.* observed an incident photon-to-current efficiency (IPCE, also known as external quantum efficiency or EQE) of 23% at λ = 400 nm using sputtered TiO_2 electrodes. $TiO_{2-x}N_x$ prepared in an analogous way exhibited IPCE values of 7% at λ = 500 nm, but the IPCE at λ = 400 nm decreased to 16%. (NB: $IPCE|_{\lambda=500nm}$ reported for these $TiO_{2-x}N_x$ films are among the highest reported; typical visible light efficiencies for N-doped TiO_2 are less than 1%.) The authors measured a similar change in the absorbed photon-to-current efficiencies (APCE, also known as internal quantum efficiency IQE, reporting $APCE|_{\lambda=400nm}$ of 45% and 22% for TiO_2 and $TiO_{2-x}N_x$, respectively. Such a change is indicative of charge-trapping states introduced by the N-doping process that decrease the overall photoconductivity of the material, manifesting in decreased efficiency even for band-to-band excitation. The authors also performed voltammetry measurements on $TiO_{2-x}N_x$ electrodes and

observed a cathodic photocurrent. The photocurrent was determined to be a capacitive filling of dopant states emptied by illumination rather than a Faradaic passage of current from the electrode to the electrolyte, consistent with charge-trapping.[17]

Despite these observations, some singly-doped titania photocatalysts have shown excellent photochemical performance. Khan *et al.* reported C-doped TiO_2 synthesized by flame pyrolysis of a Ti metal sheet in a natural gas flame.[18] The film shows an IPCE of 8.35% compared to the 1.08% achieved by similarly-prepared TiO_2 films (efficiency corrected for applied potential). More recently, Chen *et al.* reported a black hydrogenated TiO_2 in 2011, claiming its visible light absorption results from a continuum of electronic states arising primarily from lattice disorder,[19] though other reports have the more traditional point defect as the origin for the observed phenomena.[20-22] The photocatalyst produced hydrogen from a water/CH_3OH mixture over 100 hours of illumination with negligible loss of activity, and was also able to carry out the reaction using only visible light as the driving force.

2.2 Essential Vocabulary to Describe Band Engineering and Electronic Structure

Reports of singly-doped titania have produced materials with absorption features reaching further into the visible than unmodified counterparts. Important to the current discussion, several of these manuscripts reported "band gap narrowing" of the modified titania. Band gap narrowing requires modifying the electronic structure of a material by raising its VBM and/or lowering the CBM, which would be reflected in a red shift in the absorption edge of the UV-Vis spectrum. However, band gap narrowing is not the only effect that can introduce such red shifts. Absorption involving localized impurity states can also lead to spectral changes. The differences and implications of these two kinds of absorption were discussed at length with reference to anion-doped titania by Serpone in 2006.[8] A detailed analysis of absorption spectra for both cation- and anion-doped titania suggested that the reported red shifts in absorption were probably due to transitions to, from, or between defect states rather than true band gap narrowing (Figure 2.1).[23] Specifically, introducing dopants such as C or N results in the reduction of Ti^{4+} to Ti^{3+} and/or ejection of oxygen to form oxygen vacancies (F^+ or F^{++} centers), which also contribute to the defect electronic structure.

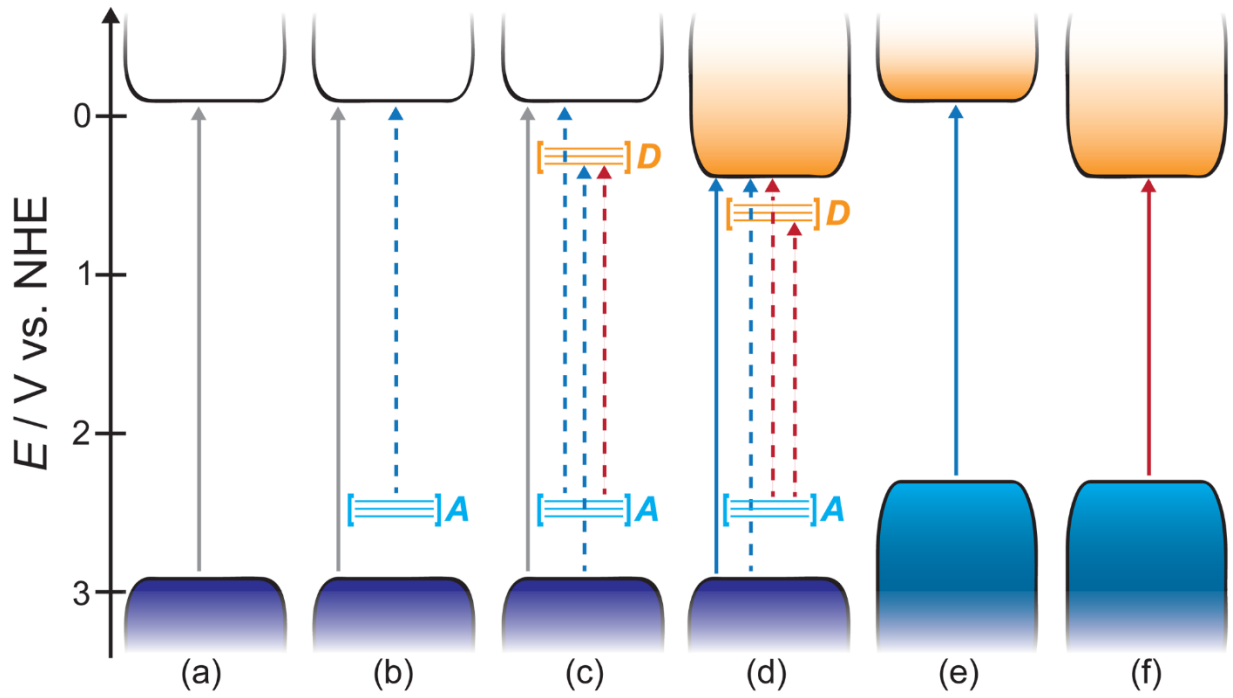

Figure 2.2. Schematic representation of the electronic structure of (a) pristine TiO_2; (b) TiO_2 doped with an acceptor atom; (c) TiO_2 co-doped with acceptor and donor atoms; (d) TiO_2 alloyed with donor atoms but dopes with acceptors, resulting in the formation of additional donor states below the CB; (e) TiO_2 co-alloyed with an acceptor and a donor whose energy levels reside within the original conduction band; and (f) TiO_2 co-alloyed with an acceptor and a donor whose energy levels reside below the original conduction band edge. Electronic transitions represented by dotted lines are not expected to result in mobile charge carriers. The band positions shown are based on anatase TiO_2.

What are the implications, then, of defect absorption? Figure 2.2 shows a series of electronic structure schematics that will accompany the discussion. Part (a) shows the band gap of pristine TiO_2, in which the valence band is composed of O(2p) states and the conduction band of Ti(3d) states. In (b), TiO_2 has been doped with an anion with acceptor levels (A) above the VBM and in (c), the *co-doping* case, a cation with donor levels (D) below the conduction band has been added. By definition, the discrete A and D defect states do not mix with the delocalized states comprising the VB or CB. Absorption involving defect states does not generate mobile charge carriers because there is little to no spatial overlap between the localized defect states in which the electron (or hole) resides after excitation and the delocalized CB (or VB). Therefore, while heavy co-doping may increase a material's visible light absorption, overall photoconductivity or photochemical response often decreases. In Figure 2.2, such transitions have been denoted using

dashed lines. Part (d) shows a partially-alloyed case in which donor atoms have been added in an alloying stoichiometry but acceptor atoms have not. In this case, or in the case of large mismatch in concentration of donor and acceptor atoms (termed co-incorporation), defect states will still dominate the electronic structure. The acceptor states have not hybridized with the valence band, and additional charge-compensating donor states are still required. In TiO_2-based systems, these additional states are often Ti^{3+}. Charge may also be compensated by cation vacancies.

The converse case in which acceptor atoms are added in an alloying stoichiometry but donor atoms are not would exhibit an analogously defect-dominated electronic structure. Oxides commonly compensate for excess negative charge by ejecting oxygen to form oxygen vacancies, which function as donors.

Finally, parts (e) and (f) of the figure show TiO_2 compositions in which both anions and cations have been substituted in alloying stoichiometries so that their respective defect states broaden and hybridize into delocalized bands. In these *co-alloyed* cases, absorption producing mobile charge carriers is expected. It should be noted that for some common substituent ion choices, such as $Ti_{1-x}Nb_xO_2$, the Nb(4d) donor states lie within the conduction band of TiO_2.[24-25] It is not necessary for donor states to lie in the midgap for co-alloying to be effective, as in (e). In (f), we have outlined the case of maximum band gap narrowing, where donor states do lie in the midgap and reduce the band gap by bringing the CBM lower in energy.

A current example of band engineering in water splitting photocatalysis is the oxynitride. Stoichiometric transition metal oxynitrides have emerged relatively recently as interesting materials with photochemical applications. Oxynitrides were popularized largely by the work of Domen and coworkers on the materials $LaTiO_2N$ and TaON.[26-36] Oxynitrides make attractive targets for photocatalysts due to their raised VBM energies. It has been shown that O(2p) and N(2p) atomic states hybridize to form an energetically continuous VB that is closer in energy to the empty metal d states that typically compose the bottom of the CB. The result is a semiconducting material with a reduced band gap compared to the related oxide.

Returning to TiO_2, co-alloyed titania systems stand to address many of the limitations identified in singly-doped TiO_2. In an ideal co-alloyed material, both a cationic and an anionic substituent replace atoms of the host structure on their appropriate crystallographic sites in a charge-compensating stoichiometry and in large mole fraction. With judicious choice of co-

alloying agents, this enables 1) minimization of defect structure, which should maintain high photoconductivity through reducing the number of trap states; and 2) delocalization of co-alloying ion states into true bands capable of hybridizing with the existing band structure of the parent compound.

2.3 Co-doped and Co-incorporated TiO_2

Electronic structure calculations have been performed that predict the behavior of co-alloyed TiO_2.[24,25,37,38] However, experimental measurements confirming their predictions up to this point have been limited because synthetic efforts have only realized non-stoichiometric incorporation of impurity pairs (co-incorporation) rather than stoichiometric co-alloying. For example, our group has synthesized a co-incorporated $Ti_{1-(5x/4)}Nb_xO_{2-y-\delta}N_y$ (hereby referred to as TiNbON-*x*, where *x* = the mole percent Nb) which will be the subject of Chapter 3. The resulting bright orange powder showed an absorption edge near 2.2 eV.[39-41] Nitridation was achieved via a heterogeneous high-temperature ammonolysis reaction that resulted in a maximum of 2% nitrogen incorporation regardless of Nb concentration, though it was shown that the fraction of substitutional (N on an O site in anatase) versus interstitial (N occupies a new crystallographic site) nitrogen increased with increasing Nb content.

Cottineau *et al.* also prepared a co-incorporated TiNbON of mixed rutile/anatase phase in the form of nanotube photoelectrodes.[42] The co-incorporated nanotube arrays' efficiencies for visible light-driven photochemistry were measured using photocurrent-action spectra, which showed that TiNbON showed anodic photocurrent in 0.1 M H_2SO_4 in the visible range of the spectrum. The activity was greatest for a Nb fraction of about 0.7% and a N fraction of 6.9%. Importantly, the TiNbON nanotubes showed superior activity to nitride TiO_2 in the ultraviolet range of the spectrum.

Marchiori et al. analyzed visible light absorption for anatase/brookite TiNbON with 2.15% Nb (N content not reported).[43] The authors performed no photochemistry, but used extended X-ray absorption fine structure (EXAFS) analysis and electron paramagnetic resonance (EPR) spectroscopy coupled with density functional theory (DFT) calculations to determine the electronic structure of the materials. Visible light absorption was attributed to localized N^{3-} midgap states whose charge density is enhanced after Nb^{5+} doping.

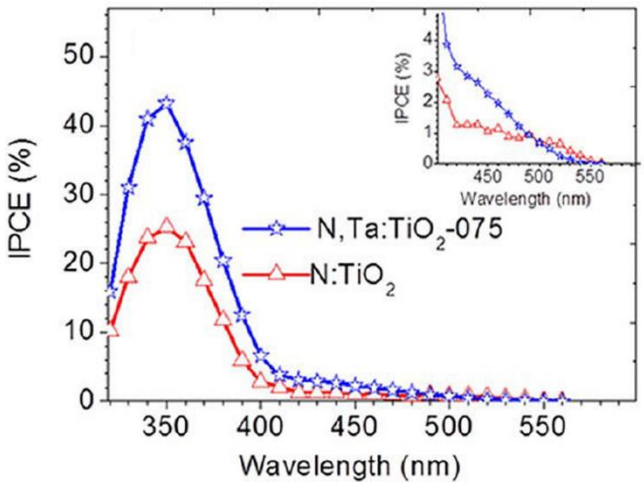

Figure 2.3. IPCE spectra of TiO_2:N and TiTaON nanowire electrodes measured at 1.23 V vs. RHE in 1 M KOH electrolyte. The inset shows an enlargement of the visible light region. Adapted from ref. 44 with permission. Copyright 2012 American Chemical Society.

Impurity pairs besides Nb^{5+} and N^{3-} have been studied as well. Hoang et al. reported the solvothermal synthesis of co-incorporated rutile TiTaON nanowire electrodes with 0.29 at % Ta (N content not reported).[44] Co-incorporated samples exhibit photocurrent-action spectra that extend well into the visible range of the spectrum, showing improved performance compared to TiO_2:N until ~500 nm (Figure 2.3). Importantly, the IPCE was nearly doubled in the ultraviolet region of the spectrum, reaching 43% (compared to 25% for TiO_2:N and 60% for TiO_2:Ta, $\lambda = 350$ nm). Cho et al. prepared rutile TiWOC nanowire electrodes at surface concentrations of 10 at % W and 13 at % C.[45] These electrodes exhibit a photocurrent density for water oxidation of 1.8 mA/cm^2 on an electrode poised at 1.23 V vs. RHE along with very high IPCE values of 80% at $\lambda = 360$ nm. However, despite a noticeable tail extending into the visible region of the UV-Vis spectrum, the TiWOC electrodes exhibited very low quantum efficiencies (<1%) in that region, possibly due to surface segregation of impurity pairs. These discoveries and others are summarized in Tables 2.1 and 2.2.[46-48] In most cases, incorporation of impurity pairs (N, in particular) remains low.

Table 2.1. Composition and IPCE data for modified TiO_2 electrodes. [a]: compositional analysis via XPS and does not represent bulk concentration unless otherwise noted. Variable subscripts imply undetermined values. [b]: Bulk concentration of Nb only determined by EDX. [c]: surface concentrations determined by secondary ion mass spectrometry, see ref. 45.

Sample	formula[a]	$IPCE_{UV}$ (λ, nm)	$IPCE_{vis}$ (λ, nm)	ref.
TiO_2 film	TiO_2	23% (400)	0% (500)	[17]
$TiO_{2-x}N_x$ film	$TiO_{1.987}N_{0.013}$	16% (400)	7% (500)	[17]
TiO_2 nanotubes (NT)	TiO2	30% (350)	0% (500)	[42]
TiO_2:N nanotubes	$TiO_{1.986}N_{0.014}$	3% (350)	0.02% (500)	[42]
TiO_2:(Nb,N) NTs	$Ti_{0.913}Nb_{0.007}O_{1.931}N_{0.069}$[b]	13% (350)	0.05% (500)	[42]
TiO_2 nanowires (NW)	TiO_2	30% (350)	0% (500)	[44]
TiO_2:N NWs	$TiO_{2-x}N_x$	23% (350)	1% (500)	[44]
TiO_2:(Ta,N) NWs	$Ti_{0.913}Ta_{0.087}O_{2-x}N_x$	42% (350)	1% (500)	[44]
TiO_2 NWs	TiO_2	32% (395)	0% (500)	[45]
TiO_2:(W,C) NWs	$Ti_{0.697}W_{0.303}O_{1.607}C_{0.393}$[c]	80% (380)	0.5% (500)	[45]

Table 2.2. Composition and photochemical pollutant degradation activity for modified TiO2 photocatalyst powders. [a]: compositional analysis via XPS and does not represent bulk concentration unless otherwise noted. Variable subscripts or "nd" imply undetermined values. [b]: Incident light intensities not reported. "UV + visible" refers to an unfiltered metal halide lamp (Philips HPA 400/30S).

Sample	formula[a]	Pollutant	k (h^{-1})	illumination[b]	ref
Degussa P25	TiO_2	Methylene blue (40 ppm)	0.561	AM 1.5G	[39]
TiO_2:(Nb,N)	$Ti_{0.75}Nb_{0.25}O_{1.98-\delta}N_{0.02}$	Methylene blue (40 ppm)	0.779	AM 1.5G	[41]
TiO_2	TiO_2	Rhodamine B (10 μM)	0.135	λ > 420 nm	[46]
TiO_2:(Mo,C)	nd	Rhodamine B (10 μM)	0.252	λ > 420 nm	[46]
TiO_2	TiO_2	4-chlorophenol (50 μM)	0.012	λ > 400 nm	[47]
		4-chlorophenol (50 μM)	1.218	UV + visible	[47]
TiO_2:(B,N)	nd	4-chlorophenol (50 μM)	0.198	λ > 400 nm	[47]
		4-chlorophenol (50 μM)	2.046	UV + visible	[47]
TiO_2:(Sn,N)	$Ti_{0.926}Sn_{0.034}O_{1.94}N_{0.06}$	4-chlorophenol (50 μM)	0.083	λ > 400 nm	[48]
		4-chlorophenol (50 μM)	2.916	UV + visible	[48]

2.4 Challenges for Preparing and Characterizing Co-alloyed Materials

In order to realize band gap narrowing and maximize visible light absorption, unit mole ratios of substituent ions in high mole faction are necessary. Thus, synthetic preparations for co-alloyed materials remain limited. A useful synthetic method must be generalizable, tunable, and scalable. Many of the methods presented in this section and elsewhere rely on preparing a TiO_2 or cation-doped TiO_2 precursor followed by heat treatment in a reactive atmosphere to achieve anion

co-doping. Heterogeneous reactions are often confined to particle surfaces, which is a likely explanation for the > 7 mol % ceiling observed in most N-doped TiO_2 studies, even with a cationic dopant present to increase the solubility of the nitride anion. With only a narrow range of anion contents available by these methods, tunability is limited. Electrosynthetic methods based on TiO_2 anodization have not yet demonstrated complete control over cation contents over their solubility range, e.g. ref 42.

Additionally, dopants introduced in gas-phase surface reactions do not necessarily diffuse throughout the material bulk, as evidenced by secondary-ion mass spectrometry (SIMS) mapping analsys by Cho *et al.* in TiWOC nanowires (Figure 2.4).[45]

Ruddy *et al.* presented an interesting synthesis for attempts at co-alloyed TiMoON which proceeded via high-temperature, high-pressure thermolysis of a molybdenum nitrido complex in the presence of titanium *tert*-butoxide in benzene solution.[49] Compositional analysis of the resulting materials shows superior nitrogen incorporation with N:Mo ratios of 0.73 – 0.77 in the co-alloyed products with Ti:Mo ranging from 3.05 to 21.5. This clever synthetic approach releases cationic and anionic dopant species simultaneously in a charge-compensating stoichiometry. However, nitrido complexes are not accessible for all transition metals, so the scope of this approach may be limited to dopant candidates for which metal nitride complexes are isolable.

Another promising body of synthetic work has been the development of the urea-glass synthesis, which has been used to prepare a variety of phase-pure metal nitride nanoparticles with low carbon content.[50-52] This attractive synthetic pathway combines readily available metal chlorides with urea as an abundant nitrogen source in alcohol solution. It has been suggested that the synthesis is amenable to preparing thin film electrodes, but to date electrodes have been prepared (when necessary) by suspending nanoparticles in Nafion. The nitride materials are promising electrocatalysts.[53,54] However, only one report of synthesizing oxynitrides via the urea-glass route has been published,[55] and no reports of ternary metal nitrides have been published using this synthesis. Extending the urea-glass synthesis to co-alloyed materials will be the focus of Chapters 4 and 5.

Compositional analysis on co-alloyed materials remains difficult. Chemical analysis is typically achieved using X-ray photoelectron spectroscopy (XPS) and less often by energy dispersive X-ray spectroscopy (EDX). Chemical analysis by XPS is confined to the 5 – 10 nm

surface layer of a particle and is not representative of the bulk composition. Ion beam milling can provide depth-dependent compositional analysis but analysis may be complicated by preferential sputtering in which one element is removed from a material faster than another. EDX is more favorable for metals but is made difficult for light elements by overlapping lines and ease of contamination. Reliable, direct quantification of nitrogen content remains a challenge in the field.

Rutherford backscattering (RBS) spectrometry has been used to probe compositions in TiO_2 and N-doped TiO_2 materials.[56-60] RBS, often coupled with angle-resolved XPS, has been well-utilized in materials science to characterize thin films and assemblies of a variety of compositions.[61-65] Depth profiling is also possible. However, for titanium oxynitride species, compositional analysis is complicated by overlapping signals for N and O. Auger electron spectroscopy (AES) may also be used for nitrogen determination due to the superior signal strength for light elements in that technique. However, again, for titanium (oxy)nitrides, the analysis is confounded by overlapping signals for Ti and N that require careful mathematical treatment to maintain accuracy.[66-67]

Secondary-ion mass spectrometry (SIMS) is perhaps the most promising technique currently available for examining depth-dependent compositions. SIMS has already been used to measure sensitive phenomena such as nitrogen dopant diffusion through rutile crystals.[68,69] Figure 2.4 shows an example of SIMS used to characterize TiWOC nanowires.[45]

Bulk nitrogen may be determined by Kjeldahl analysis, a standard technique in organic and biochemistry. A sample is dissolved in acidic solution, which releases the material's nitride as ammonium cation. The solution is alkalized and boiled, and the effluent gas (ammonia) is trapped by a standard acid. Nitride as ammonia is then determined by titration. This technique has not been widely applied to compositional analysis of co-incorporated materials, likely due to the large sample sizes (~1 g or greater) needed for accurate analysis on typical laboratory equipment.

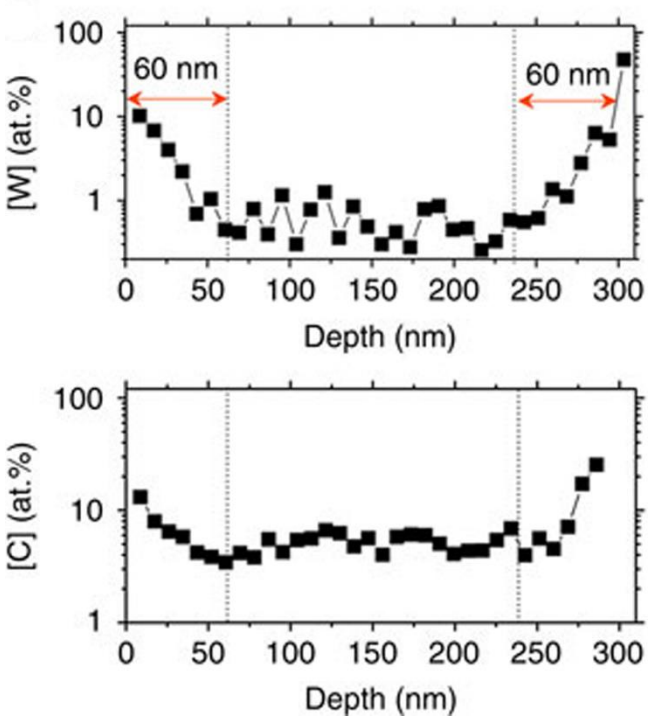

Figure 2.4. SIMS profile of a single TiWOC nanowire showing dopant concentration across the nanowire thickness. Adapted from ref. 45 with permission from Nature Publishing Group.

Wavelength-dependent quantifications of P(E)C reactivity have been very useful for establishing a picture of electronic structure in co-incorporated TiO_2 materials. Generally, modified titania photocatalysts have exhibited poor quantum efficiencies in the visible range of the spectrum despite, in some cases, strong visible light absorption. Additionally, activity in the ultraviolet range is decreased relative to parent TiO_2 prepared using similar methods as discussed previously. Improved spectral response in both the UV and visible regions has been interpreted to be a result of improved charge compensation and reduced defect structure in the material bulk. However, the inherent difficulty of preparing well-contacted thin films in many cases precludes highly resolved wavelength-dependent measurements for powder photocatalysts. More general methods of interrogating both thin films and powder materials are needed.

Photoluminenscence (PL) spectroscopy is a standard technique characterizing defect structure in inorganic solids. It has been applied to both rutile and anatase TiO_2 of various morphologies[70-73] and also to doped titania systems.[74-76] Photoluminsescence lifetimes have informed on the nature of defect states and how various defects affect carrier transport and recombination. However, measured lifetimes are typically in the μs to ms regime. To investigate

faster processes that can have a profound effect on photocatalysis, more sophisticated techniques are required. Transient absorption spectroscopy (TAS) has become an extremely useful technique for measuring fast photodynamical processes in reactive semiconductors. The technique has been applied to several TiO_2-based systems.[20,77-82] Perhaps the greatest strength of TAS is its adaptability to *in situ* and *in operando* measurements. Although doped TiO_2 has been investigated with TAS, co-doped TiO_2 has not received the same attention. Understanding the effects of co-doping, co-incorporating, and potentially co-alloying on charge carrier dynamics will be critical to understanding observed differences in reactivity; TAS provides such information with great detail and unparalleled time resolution. Ruddy *et al.* present a similarly useful transient photoconductance study on their co-incorporated TiMoON materials and find that they exhibit ms timescale photoconductance at both UV and visible excitation wavelengths.[49] The photoconductance signal is unexpectedly low, pointing to potential ps-timescale charge trapping activity or to low generation yield.

Other broadly useful spectroscopic methods include electron paramagnetic resonance (EPR) and ultraviolet and X-ray photoelectron spectroscopy (UPS and XPS). EPR can be used to provide information about specific defect identities. XPS is traditionally used to probe surface chemical states, particularly for transition metals, but both valence band XPS and UPS are useful for mapping occupied states in a material's electronic structure as well as measuring the VBM.

Quantifications of the band edge energies and defect structures of potential photocatalysts will guide their application towards chemical reactions; however, it must be stressed that these measurements only realize their full impact when conducted in full knowledge of the chemical composition and homogeneity of the materials in question. It is recommended that priority be placed on improving/applying further methods of characterizing both the bulk composition and the depth-dependent composition of photocatalysts and photoelectrodes.

2.5 References

(1) Kudo, A.; Miseki, Y. Heterogeneous Photocatalyst Materials for Water Splitting. *Chem. Soc. Rev.* **2009**, *38* (1), 253–278.

(2) Batzill, M. Fundamental Aspects of Surface Engineering of Transition Metal Oxide Photocatalysts. *Energy Environ. Sci.* **2011**, *4* (9), 3275.

(3) Maeda, K.; Domen, K. New Non-Oxide Photocatalysts Designed for Overall Water Splitting under Visible Light. *J. Phys. Chem. C* **2007**, *111* (22), 7851–7861.

(4) Shankar, K.; Basham, J. I.; Allam, N. K.; Varghese, O. K.; Mor, G. K.; Feng, X.; Paulose, M.; Seabold, J. a; Choi, K.-S.; Grimes, C. A. Recent Advances in the Use of TiO_2 Nanotube and Nanowire Arrays for Oxidative Photoelectrochemistry. *J. Phys. Chem. C* **2009**, *113* (16), 6327–6359.

(5) Ni, M.; Leung, M. K. H.; Leung, D. Y. C.; Sumathy, K. A Review and Recent Developments in Photocatalytic Water-Splitting Using TiO_2 for Hydrogen Production. *Renew. Sustain. Energy Rev.* **2007**, *11* (3), 401–425.

(6) Chen, X.; Mao, S. S. Titanium Dioxide Nanomaterials: Synthesis, Properties, Modifications, and Applications. *Chem. Rev.* **2007**, *107* (7), 2891–2959.

(7) Choi, W.; Termin, A.; Hoffmann, M. R. The Role of Metal Ion Dopants in Quantum-Sized TiO_2: Correlation between Photoreactivity and Charge Carrier Recombination Dynamics. *J. Phys. Chem.* **1994**, *98* (51), 13669–13679.

(8) Serpone, N. Is the Band Gap of Pristine TiO_2 Narrowed by Anion- and Cation-Doping of Titanium Dioxide in Second-Generation Photocatalysts? *J. Phys. Chem. B* **2006**, *110*, 24287–24293.

(9) Serpone, N.; Lawless, D.; Disdier, J.; Herrmann, J.-M. Spectroscopic, Photoconductivity, and Photocatalytic Studies of TiO_2 Colloids: Naked and with the Lattice Doped with Cr^{3+}, Fe^{3+}, and V^{5+} Cations. *Langmuir* **1994**, *10* (3), 643–652.

(10) Zhang, Z.; Wang, C.-C.; Zakaria, R.; Ying, J. Y. Role of Particle Size in Nanocrystalline TiO_2 -Based Photocatalysts. *J. Phys. Chem. B* **1998**, *102* (52), 10871–10878.

(11) Berglund, S. P.; Hoang, S.; Minter, R. L.; Fullon, R. R.; Mullins, C. B. Investigation of 35 Elements as Single Metal Oxides, Mixed Metal Oxides, or Dopants for Titanium Dioxide for Dye-Sensitized Solar Cells. *J. Phys. Chem. C* **2013**, *117* (48), 25248–25258.

(12) Asahi, R.; Morikawa, T.; Ohwaki, T.; Aoki, K.; Taga, Y. Visible-Light Photocatalysis in Nitrogen-Doped Titanium Oxides. *Science* **2001**, *293* (July), 2000–2002.

(13) Daghrir, R.; Drogui, P.; Robert, D. Modified TiO_2 for Environmental Photocatalytic Applications: A Review. *Industrial and Engineering Chemistry Research*, 2013, *52*, 3581–3599.

(14) Nagarajan, R.; Kumar, V.; Ahmad, S. Anion Doped Binary Oxides, SnO_2, TiO_2 and ZnO: Fabrication Procedures, Fascinating Properties and Future Prospects. *Indian J. Chem. - Sect. A Inorganic, Phys. Theor. Anal. Chem.* **2012**, *51* (1–2), 145–154.

(15) Pomoni, K.; Vomvas, A.; Trapalis, C. Dark Conductivity and Transient Photoconductivity of Nanocrystalline Undoped and N-Doped TiO_2 Sol-Gel Thin Films. *Thin Solid Films* **2008**, *516* (6), 1271–1278.

(16) Lindgren, T.; Lu, J.; Hoel, A.; Granqvist, C. G.; Torres, G. R.; Lindquist, S. E. Photoelectrochemical Study of Sputtered Nitrogen-Doped Titanium Dioxide Thin Films in Aqueous Electrolyte. *Sol. Energy Mater. Sol. Cells* **2004**, *84* (1–4), 145–157.

(17) Torres, G. R.; Lindgren, T.; Lu, J.; Granqvist, C. G.; Lindquist, S. E. Photoelectrochemical Study of Nitrogen-Doped Titanium Dioxide for Water Oxidation. *J. Phys. Chem. B* **2004**, *108* (19), 5995–6003.

(18) Khan, S. U. M.; Al-Shahry, M.; Ingler, W. B. Efficient Photochemical Water Splitting by a Chemically Modified N-TiO_2. *Science* **2002**, *297* (5590), 2243–2245.

(19) Chen, X.; Liu, L.; Yu, P. Y.; Mao, S. S. Increasing Solar Absorption for Photocatalysis with Black Hydrogenated Titanium Dioxide Nanocrystals. *Science* **2011**, *331* (6018), 746–750.

(20) Wheeler, D. A; Ling, Y.; Dillon, R. J.; Fitzmorris, R. C.; Dudzik, C. G.; Zavodivker, L.; Rajh, T.; Dimitrijevic, N. M.; Millhauser, G.; Bardeen, C.; Li, Y.; Zhang, J. Z. Probing the Nature of Bandgap States in Hydrogen-Treated TiO_2 Nanowires. *J. Phys. Chem. C* **2013**, *117* (50), 26821–26830.

(21) Fabregat-Santiago, F.; Barea, E. M.; Bisquert, J.; Mor, G. K.; Shankar, K.; Grimes, C. A. High Carrier Density and Capacitance in TiO_2 Nanotube Arrays Induced by Electrochemical Doping. *J. Am. Chem. Soc.* **2008**, *130* (34), 11312–11316.

(22) Wang, G.; Wang, H.; Ling, Y.; Tang, Y.; Yang, X.; Fitzmorris, R. C.; Wang, C.; Zhang, J. Z.; Li, Y. Hydrogen-Treated TiO_2 Nanowire Arrays for Photoelectrochemical Water Splitting. *Nano Lett.* **2011**, *11* (7), 3026–3033.

(23) Kuznetsov, V. N.; Serpone, N. Photoinduced Coloration and Photobleaching of Titanium Dioxide in TiO_2/polymer Compositions upon UV- And Visible-Light Excitation of Color Centers' Absorption Bands: Direct Experimental Evidence Negating Band-Gap Narrowing in Anion-/cation-Doped TiO_2s. *J. Phys. Chem. C* **2007**, *111* (42), 15277–15288.

(24) Gai, Y.; Li, J.; Li, S. S.; Xia, J. B.; Wei, S. H. Design of Narrow-Gap TiO_2: A Passivated Codoping Approach for Enhanced Photoelectrochemical Activity. *Phys. Rev. Lett.* **2009**, *102* (3), 23–26.

(25) Ma, X.; Wu, Y.; Lu, Y.; Xu, J. Effect of Compensated Codoping on the Photoelectrochemical Properties of Anatase TiO_2 Photocatalyst. *J. Phys. Chem. C* **2011**, *115*, 16963–16969.

(26) Kasahara, A.; Nukumizu, K.; Hitoki, G.; Takata, T.; Kondo, J. N.; Hara, M.; Kobayashi, H.; Domen, K. Photoreactions on $LaTiO_2N$ under Visible Light Irradiation. *J. Phys. Chem. A* **2002**, *106* (29), 6750–6753.

(27) Hitoki, G.; Takata, T.; Kondo, J. N.; Hara, M.; Kobayashi, H.; Domen, K. An Oxynitride, TaON, as an Efficient Water Oxidation Photocatalyst under Visible Light Irradiation ($\lambda \leq 500$ nm). *Chem. Commun.* **2002**, *2* (16), 1698–1699.

(28) Leroy, C. M.; Maegli, A. E.; Sivula, K.; Hisatomi, T.; Xanthopoulos, N.; Otal, E. H.; Yoon, S.; Weidenkaff, A.; Sanjines, R.; Grätzel, M. $LaTiO_2N/In_2O_3$ Photoanodes with Improved Performance for Solar Water Splitting. *Chem. Comm.* **2012**, *48*, 820.

(29) Maegli, A. E.; Pokrant, S.; Hisatomi, T.; Trottmann, M.; Domen, K.; Weidenkaff, A. Enhancement of Photocatalytic Water Oxidation by the Morphological Control of $LaTiO_2N$ and Cobalt Oxide Catalysts. *J. Phys. Chem. C* **2013**, *118* (30), 16344–16351.

(30) Feng, J.; Luo, W.; Fang, T.; Lv, H.; Wang, Z.; Gao, J.; Liu, W.; Yu, T.; Li, Z.; Zou, Z. Highly Photo-Responsive $LaTiO_2N$ Photoanodes by Improvement of Charge Carrier Transport among Film Particles. *Adv. Funct. Mater.* **2014**, *24* (23), 3535–3542.

(31) Zhang, F.; Yamakata, A.; Maeda, K.; Moriya, Y.; Takata, T.; Kubota, J.; Teshima, K.; Oishi, S.; Domen, K. Cobalt-Modified Porous Single-Crystalline $LaTiO_2N$ for Highly Efficient Water Oxidation under Visible Light. *J. Am. Chem. Soc.* **2012**, *134*, 8–11.

(32) Singh, R. B.; Matsuzaki, H.; Suzuki, Y.; Seki, K.; Minegishi, T.; Hisatomi, T.; Domen, K.; Furube, A. Trapped State Sensitive Kinetics in $LaTiO_2N$ Solid Photocatalyst with and without Cocatalyst Loading. *J. Am. Chem. Soc.* **2014**, *136* (49), 17324–17331.

(33) Wang, Z.; Hou, J.; Yang, C.; Jiao, S.; Huang, K.; Zhu, H. Hierarchical Metastable γ-TaON Hollow Structures for Efficient Visible-Light Water Splitting. *Energy Environ. Sci.* **2013**, *6* (7), 2134–2145.

(34) Maeda, K.; Lu, D.; Domen, K. Direct Water Splitting into Hydrogen and Oxygen under Visible Light by Using Modified TaON Photocatalysts with d(0) Electronic Configuration. *Chem. A Eur. J.* **2013**, *19* (16), 4986–4991.

(35) Kim, E. S.; Nishimura, N.; Magesh, G.; Kim, J. Y.; Jang, J. W.; Jun, H.; Kubota, J.; Domen, K.; Lee, J. S. Fabrication of $CaFe_2O_4$/TaON Heterojunction Photoanode for Photoelectrochemical Water Oxidation. *J. Am. Chem. Soc.* **2013**, *135* (14), 5375–5383.

(36) Higashi, M.; Domen, K.; Abe, R. Highly Stable Water Splitting on Oxynitride TaON Photoanode System under Visible Light Irradiation. *J. Am. Chem. Soc.* **2012**, *134* (16), 6968–6971.

(37) Wang, D.; Zou, Y.; Wen, S.; Fan, D. A Passivated Codoping Approach to Tailor the Band Edges of TiO_2 for Efficient Photocatalytic Degradation of Organic Pollutants. *Appl. Phys. Lett.* **2009**, *95* (1).

(38) Yin, W.-J.; Tang, H.; Wei, S.-H.; Al-Jassim, M. M.; Turner, J.; Yan, Y. Band Structure Engineering of Semiconductors for Enhanced Photoelectrochemical Water Splitting: The Case of TiO_2. *Phys. Rev. B* **2010**, *82* (4), 45106.

(39) Breault, T. M.; Bartlett, B. M. Lowering the Band Gap of Anatase-Structured TiO_2 by Coalloying with Nb and N: Electronic Structure and Photocatalytic Degradation of Methylene Blue Dye. *J. Phys. Chem. C* **2012**, *116* (10), 5986–5994.

(40) Breault, T. M.; Bartlett, B. M. Composition Dependence of TiO_2:(Nb,N)-X Compounds on the Rate of Photocatalytic Methylene Blue Dye Degradation. *J. Phys. Chem. C* **2013**, *117* (17), 8611–8618.
(41) Breault, T. M.; Brancho, J. J.; Guo, P.; Bartlett, B. M. Visible Light Water Oxidation Using a Co-Catalyst Loaded Anatase-Structured $Ti_{1-(5x/4)}Nb_xO_{2-y-\delta}N_y$ Compound. *Inorg. Chem.* **2013**, *52* (16), 9363–9368.
(42) Cottineau, T.; Béalu, N.; Gross, P.-A.; Pronkin, S. N.; Keller, N.; Savinova, E. R.; Keller, V. One Step Synthesis of Niobium Doped Titania Nanotube Arrays to Form (N,Nb) Co-Doped TiO_2 with High Visible Light Photoelectrochemical Activity. *J. Mater. Chem. A* **2013**, *1* (6), 2151–2160.
(43) Marchiori, C.; Di Liberto, G.; Soliveri, G.; Loconte, L.; Lo Presti, L.; Meroni, D.; Ceotto, M.; Oliva, C.; Cappelli, S.; Cappelletti, G.; Aieta, C.; Ardizzone, S. Unraveling the Cooperative Mechanism of Visible-Light Absorption in Bulk N,Nb Codoped TiO_2 Powders of Nanomaterials. *J. Phys. Chem. C* **2014**, *118* (41), 24152–24164.
(44) Hoang, S.; Guo, S.; Mullins, C. B. Coincorporation of N and Ta into TiO_2 Nanowires for Visible Light Driven Photoelectrochemical Water Oxidation. *J. Phys. Chem. C* **2012**, *116* (44), 23283–23290.
(45) Cho, I. S.; Lee, C. H.; Feng, Y.; Logar, M.; Rao, P. M.; Cai, L.; Kim, D. R.; Sinclair, R.; Zheng, X. Codoping Titanium Dioxide Nanowires with Tungsten and Carbon for Enhanced Photoelectrochemical Performance. *Nat. Commun.* **2013**, *4*, 1723.
(46) Li, Y. F.; Xu, D.; Oh, J. Il; Shen, W.; Li, X.; Yu, Y. Mechanistic Study of Codoped Titania with Nonmetal and Metal Ions: A Case of C + Mo Codoped TiO_2. *ACS Catal.* **2012**, *2* (3), 391–398.
(47) Yuan, J.; Wang, E.; Chen, Y.; Yang, W.; Yao, J.; Cao, Y. Doping Mode, Band Structure and Photocatalytic Mechanism of B-N-Codoped TiO_2. *Appl. Surf. Sci.* **2011**, *257* (16), 7335–7342.
(48) Wang, E.; He, T.; Zhao, L.; Chen, Y.; Cao, Y. Improved Visible Light Photocatalytic Activity of Titania Doped with Tin and Nitrogen. *J. Mater. Chem.* **2011**, *21* (1), 144.
(49) Ruddy, D. A.; Reid, O. G.; Leonard, B. M.; Pylypenko, S.; Neale, N. R. Non-Aqueous Thermolytic Route to Oxynitride Photomaterials Using Molecular Precursors $Ti(OtBu)_4$ and $N{\equiv}Mo(OtBu)_3$. *J. Mater. Chem. A* **2013**, *1*, 14066–14070.
(50) Giordano, C.; Erpen, C.; Yao, W.; Antonietti, M. Synthesis of Mo and W Carbide and Nitride Nanoparticles via a Simple "Urea Glass" route. *Nano Lett.* **2008**, *8* (12), 4659–4663.
(51) Giordano, C.; Erpen, C.; Yao, W.; Milke, B.; Antonietti, M. Metal Nitride and Metal Carbide Nanoparticles by a Soft Urea Pathway. *Chem. Mater.* **2009**, *21* (21), 5136–5144.
(52) Giordano, C.; Antonietti, M. Synthesis of Crystalline Metal Nitride and Metal Carbide Nanostructures by Sol–gel Chemistry. *Nano Today* **2011**, *6* (4), 366–380.
(53) Youn, D. H.; Han, S.; Kim, J. Y.; Kim, J. Y.; Park, H.; Choi, S. H.; Lee, J. S. Highly Active and Stable Hydrogen Evolution Electrocatalysts Based on Molybdenum Compounds on Carbon Nanotube-Graphene Hybrid Support. *ACS Nano* **2014**, *8* (5), 5164–5173.
(54) Higgins, D. C.; Choi, J.-Y.; Wu, J.; Lopez, A.; Chen, Z. Titanium Nitride–carbon Nanotube Core–shell Composites as Effective Electrocatalyst Supports for Low Temperature Fuel Cells. *J. Mater. Chem.* **2012**, *22* (9), 3727–3732.
(55) Gao, Q.; Giordano, C.; Antonietti, M. Controlled Synthesis of Tantalum Oxynitride and Nitride Nanoparticles. *Small* **2011**, *7* (23), 3334–3340.
(56) Kim, S. J.; Xu, K.; Parala, H.; Beranek, R.; Bledowski, M.; Sliozberg, K.; Becker, H. W.; Rogalla, D.; Barreca, D.; Maccato, C.; Sada, C.; Schuhmann, W.; Fischer, R. a.; Devi, A. Intrinsic Nitrogen-Doped CVD-Grown TiO_2 Thin Films from All-N-Coordinated Ti Precursors for Photoelectrochemical Applications. *Chem. Vap. Depos.* **2013**, *19* (1–3), 45–52.
(57) Tavares, C. J.; Marques, S. M.; Viseu, T.; Teixeira, V.; Carneiro, J. O.; Alves, E.; Barradas, N. P.; Munnik, F.; Girardeau, T.; Rivière, J. P. Enhancement in the Photocatalytic Nature of Nitrogen-Doped PVD-Grown Titanium Dioxide Thin Films. *J. Appl. Phys.* **2009**, *106* (11).
(58) Mohamed, S. H.; Kappertz, O.; Ngaruiya, J. M.; Niemeier, T.; Drese, R.; Detemple, R.; Wakkad, M. M.; Wuttig, M. Influence of Nitrogen Content on Properties of Direct Current Sputtered TiO_xN_y Films. *Phys. Status Solidi Appl. Res.* **2004**, *201* (1), 90–102.

(59) Drogowska, K.; Kim-Ngan, N. T. H.; Balogh, A. G.; Radecka, M.; Brudnik, A.; Zakrzewska, K.; Tarnawski, Z. Diffusion and Chemical Composition of TiN_xO_y Thin Films Studied by Rutherford Backscattering Spectroscopy. *Surf. Sci.* **2010**, *604* (11–12), 1010–1014.

(60) Fabreguette, F.; Imhoff, L.; Guillot, J.; Domenichini, B.; Marco de Lucas, M. C.; Sibillot, P.; Bourgeois, S.; Sacilotti, M. Temperature and Substrate Influence on the Structure of TiN_xO_y Thin Films Grown by Low Pressure Metal Organic Chemical Vapour Deposition. *Surf. Coatings Technol.* **2000**, *125* (1–3), 396–399.

(61) Brijs, B.; Sajavaara, T.; Giangrandi, S.; Janssens, T.; Conard, T.; Arstila, K.; Nakajima, K.; Kimura, K.; Bergmaier, A.; Dollinger, G.; Vantomme, A.; Vandervorst, W. The Analysis of a Thin $SiO_2/Si_3N_4/SiO_2$ Stack: A Comparative Study of Low-Energy Heavy Ion Elastic Recoil Detection, High-Resolution Rutherford Backscattering and Secondary Ion Mass Spectrometry. *Nucl. Instruments Methods Phys. Res. Sect. B Beam Interact. with Mater. Atoms* **2006**, *249* (1–2 SPEC. ISS.), 847–850.

(62) Kimura, K.; Nakajima, K.; Conard, T.; Vandervorst, W.; Bergmaier, A.; Dollinger, G. Precise Nitrogen Depth Profiling by High-Resolution RBS in Combination with Angle-Resolved XPS. *Nucl. Instruments Methods Phys. Res. Sect. B Beam Interact. with Mater. Atoms* **2010**, *268* (11–12), 1960–1963.

(63) Kimura, K.; Nakajima, K.; Zhao, M.; Nohira, H.; Hattori, T.; Kobata, M.; Ikenaga, E.; Kim, J. J.; Kobayashi, K.; Conard, T.; Vandervorst, W. Combination of High-Resolution RBS and Angle-Resolved XPS: Accurate Depth Profiling of Chemical States. *Surf. Interface Anal.* **2008**, *40* (3–4), 423–426.

(64) Silva, C.; Vovk, A.; da Silva, R. C.; Strichonavec, P.; Algarabel, P. A.; Casaca, A.; Meneghini, C.; Carlomagno, I.; Godinho, M.; Cruz, M. M. Influence of the Substrate on Structure and Magnetic Properties of Co–N Thin Films. *J. Alloys Compd.* **2015**, *633*, 470–478.

(65) Tian, X. B.; Wei, C. B.; Yang, S. Q.; Fu, R. K. Y.; Chu, P. K. Corrosion Resistance Improvement of Magnesium Alloy Using Nitrogen Plasma Ion Implantation. *Surf. Coatings Technol.* **2005**, *198* (1–3), 454–458.

(66) Dawson, P. T.; Tzatzov, K. K. Quantitative Auger Electron Spectroscopic Analysis of Titanium Nitrides. *Surf. Sci.* **1985**, *149*, 105–118.

(67) Sundgren, J. E.; Johansson, B. O.; Karlsson, S. E. Kinetics of Nitride Formation on Titanium Targets during Reactive Sputtering. *Surf. Sci.* **1983**, *128* (2–3), 265–280.

(68) Diwald, O.; Thompson, T. L.; Goralski, E. G.; Walck, S. D.; Yates, J. T. The Effect of Nitrogen Ion Implantation on the Photoactivity of TiO_2 Rutile Single Crystals. *J. Phys. Chem. B* **2004**, *108* (1), 52–57.

(69) Palgrave, R. G.; Payne, D. J.; Egdell, R. G. Nitrogen Diffusion in Doped TiO_2 (110) Single Crystals: A Combined XPS and SIMS Study. *J. Mater. Chem.* **2009**, *19* (44), 8418–8425.

(70) Zhang, W. F.; Zhang, M. S.; Yin, Z.; Chen, Q. Photoluminescence in Anatase Titanium Dioxide Nanocrystals. *Appl. Phys. B Lasers Opt.* **2000**, *70* (2), 261–265.

(71) Yan, J.; Wu, G.; Guan, N.; Li, L.; Li, Z.; Cao, X. Understanding the Effect of Surface/bulk Defects on the Photocatalytic Activity of TiO_2: Anatase versus Rutile. *Phys. Chem. Chem. Phys.* **2013**, *15* (26), 10978–10988.

(72) Mercado, C. C.; Knorr, F. J.; McHale, J. L.; Usmani, S. M.; Ichimura, A. S.; Saraf, L. V. Location of Hole and Electron Traps on Nanocrystalline Anatase TiO_2. *J. Phys. Chem. C* **2012**, *116* (19), 10796–10804.

(73) Yoo, H.; Kim, M.; Bae, C.; Lee, S.; Kim, H.; Ahn, T. K.; Shin, H. Understanding Photoluminescence of Monodispersed Crystalline Anatase TiO_2 Nanotube Arrays. *J. Phys. Chem. C* **2014**, *118* (18), 9726–9732.

(74) D'Arienzo, M.; Siedl, N.; Sternig, A.; Scotti, R.; Morazzoni, F.; Bernardi, J.; Diwald, O. Solar Light and Dopant-Induced Recombination Effects: Photoactive Nitrogen in TiO_2 as a Case Study. *J. Phys. Chem. C* **2010**, *114* (42), 18067–18072.

(75) Enache, C. S.; Schoonman, J.; Van De Krol, R. The Photoresponse of Iron- and Carbon-Doped TiO_2 (Anatase) Photoelectrodes. *J. Electroceramics* **2004**, *13* (1–3), 177–182.
(76) Zhang, J.; Chen, X.; Shen, Y.; Li, Y.; Hu, Z.; Chu, J. Synthesis, Surface Morphology, and Photoluminescence Properties of Anatase Iron-Doped Titanium Dioxide Nano-Crystalline Films. *Phys. Chem. Chem. Phys.* **2011**, *13* (28), 13096–13105.
(77) Knauf, R. R.; Brennaman, M. K.; Alibabaei, L.; Norris, M. R.; Dempsey, J. L. Revealing the Relationship between Semiconductor Electronic Structure and Electron Transfer Dynamics at Metal Oxide–Chromophore Interfaces. *J. Phys. Chem. C* **2013**, *117* (48), 25259–25268.
(78) Zhao, H.; Zhang, Q.; Weng, Y. X. Deep Surface Trap Filling by Photoinduced Carriers and Interparticle Electron Transport Observed in TiO_2 Nanocrystalline Film with Time-Resolved Visible and Mid-IR Transient Spectroscopies. *J. Phys. Chem. C* **2007**, *111* (9), 3762–3769.
(79) Sun, J.; Yang, Y.; Khan, J. I.; Alarousu, E.; Guo, Z.; Zhang, X.; Zhang, Q.; Mohammed, O. F. Ultrafast Carrier Trapping of a Metal-Doped Titanium Dioxide Semiconductor Revealed by Femtosecond Transient Absorption Spectroscopy. *ACS Appl. Mater. Interfaces* **2014**, *6* (13), 10022–10027.
(80) Tamaki, Y.; Furube, A.; Murai, M.; Hara, K.; Katoh, R.; Tachiya, M. Dynamics of Efficient Electron-Hole Separation in TiO_2 Nanoparticles Revealed by Femtosecond Transient Absorption Spectroscopy under the Weak-Excitation Condition. *Phys. Chem. Chem. Phys.* **2007**, *9* (12), 1453–1460.
(81) Yoshihara, T.; Yoshihara, T.; Katoh, R.; Katoh, R.; Furube, A.; Furube, A.; Tamaki, Y.; Tamaki, Y.; Murai, M.; Murai, M.; Hara, K.; Hara, K.; Murata, S.; Murata, S.; Arakawa, H.; Arakawa, H. Identification of Reactive Species in Photoexcited Nanocrystalline TiO_2 Films by Wide-Wavelength-Range (400−2500 nm) Transient Absorption Spectroscopy. *J. Phys. Chem. B* **2004**, *108* (12), 3817–3823.
(82) Willis, R. L.; Olson, C.; O'Regan, B.; Lutz, T.; Nelson, J.; Durrant, J. R. Electron Dynamics in Nanocrystalline ZnO and TiO_2 Films Probed by Potential Step Chronoamperometry and Transient Absorption Spectroscopy. *J. Phys. Chem. B* **2002**, *106* (31), 7605–7613.

Chapter 3

Visible Light Water Oxidation Using a Co-Catalyst Loaded Anatase-Structured $Ti_{1-(5x/4)}Nb_xO_{2-y-\delta}N_y$ Compound Prepared By Traditional Syntheses

Portions of this chapter have been published:

Breault, T. M., Brancho, J. J., Guo, P., Bartlett, B. M. *Inorg. Chem.* **2013**, 52, 9363-9368.

3.1 Introduction

The work contained in subsequent chapters of this thesis builds on seminal studies on co-doped and co-incorporated anatase $Ti_{1-(5x/4)}Nb_xO_{2-y-\delta}N_y$ (TiNbON) materials prepared by well-known synthetic methods. These works[1-3] establish the proof-of-concept needed for further explorations of co-incorporated material synthesis in the TiNbON system, while other research efforts, both computational and experimental, have focused on coalloying pairs in TiTaON and TiWOC. Complete charge compensation between the donor and acceptor (a true co-alloy) has yet to be achieved in any form of TiO_2; however, the reports cited above show improved photoelectrochemical response for water oxidation when compared to singly-alloyed analogues.

Our group's previous work on TiNbON introduced the first experimental reports of incorporating Nb^{5+} and N^{3-} in anatase TiO_2, targeting high mole percent (25%) of the donor species Nb. The reported nitrogen content maximizes at 2 mol %. Nevertheless, we observe that methylene blue dye degrades at twice the rate over TiNbON-25 compared to commercial Degussa P25 and seven times the rate of anatase TiO_2. In addition, we have determined the interplay between niobium loading and substitutional nitrogen in the compound. We find that high niobium mole

percents are optimal for fast dye degradation due to a combination of a lower optical absorption edge (E ~ 2.2 eV) and a decrease in Ti^{3+} impurity states. One pathway for methylene blue dye degradation using TiNbON-25 is oxidizing tertiary amines to form the azure dyes. This reaction requires generating hydroxyl radicals (•OH), a reactive oxygen species, from aqueous solution.[4] In this chapter, we show that in addition to redox chemistry leading to dye degradation by active oxygen species, our TiNbON-25 compound also acts as a visible light-active water oxidation photocatalyst in the presence of a cocatalyst and an electron acceptor.

3.2 Experimental Procedures

Synthesis of TiNbON-25. All reagents were used without further purification. The parent oxide, $Ti_{0.75}Nb_{0.25}O_2$, was synthesized by sol-gel chemistry. In a typical reaction, niobium (V) chloride (Strem, 99.99%) and titanium (IV) butoxide (Aldrich, 97%) were dissolved in a 1:3 mole ratio in 2-methoxyethanol. The colorless solution was allowed to stir overnight at room temperature in ambient conditions. The solution was then annealed in air in an MTI box furnace at 500 °C with a heating and cooling rate of 4 °C/min. For nitrogen incorporation, isolated white powders were annealed under an ammonia flow (110 mL/min, Cryogenic Gases, 99.99%) for 4 h in an MTI tube furnace. The samples were cooled under ammonia flow at a rate of 1.3 °C/min.

The desired quantity of RuO_2 cocatalyst was added using a $RuCl_3•xH_2O$ precursor (Strem, 99.9%). A stock solution of 1 mg/mL RuCl3 was prepared by dissolving a known quantity of $RuCl_3•xH_2O$ in Millipore water (18.2 MΩ) and stirring at room temperature. The appropriate volume of stock solution was then added to 200 mg of the photocatalyst to achieve various wt % loadings. The solutions were stirred at 100 °C until all of the water was evaporated. The cocatalyst loaded powder was subsequently annealed in air at 350 °C for 1 h to crystallize RuO_2.

Characterization. The powders were analyzed using powder X-ray diffraction (Bruker D8 Advance diffractometer, Cu Ka radiation) with a 0.6 mm incidence slit, a step size of 0.05 /step, and a scan rate of 2 s/step. X-ray photoelectron spectroscopy was performed using a Kratos XPS (8 mA, 14 keV, monochromatic Al source). All peaks were calibrated to the C(1s) peak at 284.5 eV. The XPS data were fit using CasaXPS. UV-vis spectroscopy was performed on a Cary5000 spectrophotometer (Agilent) equipped with a Praying Mantis diffuse reflectance accessory. Spectra were recorded in reflectance mode and transformed mathematically into normalized absorbance by the Kubelka-Munk function, $F(R) = (1 - R)^2/2R$. $BaSO_4$ was used as the reference

material. HRTEM was performed on a JEOL 3011 TEM with a LaB_6 electron source operated at 300 kV. The samples were dispersed in methanol and drop cast onto a copper grid with ultrathin holey carbon film (Ted Pella).

Photochemical Methods. The water oxidation reaction was performed in a custom-built 64 mL Pyrex cell fit with a quartz window. A total of 50 mg of TiNbON-25 loaded with RuO_2 was suspended in 30 mL of 1 mM $NaIO_3$ (Aldrich, 99%). The solution was purged with nitrogen for 1 h. A fluorescence probe (FOSSPOR Ocean Optics, Inc.) was calibrated at 20.9% O_2 and 0% O_2 before use. Once the solution was pruged and the probe equilibrated at 0% O_2, the cell was irradiated for 3 h using a Newport-Oriel 150 W Xe arc lamp fitted with appropriate filters, specified throughout. The ideal gas law was used to calculate the number of moles of O_2 produced, using the measured volume of head space (34 mL), temperature recorded by the NeoFox probe, and partial pressure of O_2 recorded with the fluorescence probe. Additionally, the reaction order in iodate anion was determined by measuring the O_2 evolution rate at various iodate concentrations (1 mM, 2 mM, and 5 mM). Control experiments were performed in a similar setup excluding cocatalyst loaded powders and iodate anions, and negligible oxygen is detected after 3 h of illumination.

Gas-phase Mass Spectrometry. In a typical experiment, a custom-designed 5 mL U-shaped glass reactor with magnetic stir bar was loaded with 4 μL of a 0.250 M aqueous $NaIO_3$ solution, which was then evaporated to dryness in a drying oven. Experiments were conducted using 6 mg of photocatalyst and 1 mL of either deionized water or $H_2{}^{18}O$ (Cambridge Isotope Laboratory, 97% enrichment, 99.5% purity), which created a 1 mM $NaIO_3$ solution after reconstituting the dried salt. The solution was sparged with He for 30 min before attached to the mass spectrometer using Swagelok adapters. The reactor was irradiated using a Newport-Oriel 150 W Xe arc lamp at 1.2 W/cm2 with stirring for 1 h. Headspace analysis was performed on a Hiden Analytical HPR-20 mass spectrometer coupled with an Aalborg mass flow controller. Helium (99.997%, Cryogenic Gases) was used as the carrier gas. Faraday detectors were used to quantify gaseous water, helium, and nitrogen. A single-electron multiplier detector was used to quantify oxygen species ($^{32}O_2$, $^{34}O_2$, $^{36}O_2$). The flow rate of He was 6 mL/min. To obtain the total moles of gases detected in a given experiment, the pressure data from the instrument were first normalized to the flow rate of helium to obtain individual gas flow rates. Using the flow rates at the time the lamp was activated as a

baseline, the data were integrated in Origin 8.6 to give the total volumes of gas detected. The volume was then converted to moles using the ideal gas law.

Inductively Coupled Plasma/Atomic Emission Spectroscopy (ICP-AES). An ICP-AES assay was conducted on the supernatant solution from a typical oxygen evolution experiment using he AM 1.5G filter at 600 mW/cm^2 irradiance for 3 h. The solution was centrifuged on a Thermo Durafuge 100 for 10 min at 3500 rpm, and the supernatant was passed through a sintered glass frit filter funnel before analysis for Ti, Nb, and Ru content. A Perkin-Elmer Optima 2000DV apparatus was employed for analysis using a Y internal standard. The emission lines used for Ti, Nb, Ru, and Y were 334.090 nm, 313.079 nm, 240.272 nm, and 371.029 nm, respectively.

3.3 Physical Characterization by PXRD and HRTEM

TiNbON-25 was synthesized via a sol-gel route, yielding a crystalline anatase compound with an optical absorption edge of 2.2 eV, consistent with previous reports. The RuO_2 cocatalyst was crystallized at a low temperature of 350 °C to maintain substitutional nitrogen in the TiNbON-25 compound as confirmed by X-ray photoelectron spectroscopy (Figure A1). Furthermore, at 1 wt % RuO_2 loading, the cocatalyst is no detected by X-ray diffraction. To verify that RuO_2 results from the annealing treatment, a control experiment shows that annealing an aqueous solution of $RuCl_3 \bullet xH_2O$ in air at 350 C for 1 h yields polycrystalline RuO_2, confirmed by PXRD (Figure A2).

High-resolution transmission electron microscopy (HRTEM) images in Figure 3.1 show that particles have a narrow size distribution, 15 ± 5 nm, with a histogram presented in Figure A3, that form aggregates. The surface area of TiNbON-25 is 63 m^2/g, determined by fitting N_2 adsorption isotherms to the Brunauer-Emmett-Teller (BET) model, which supports the small particle size of 15 nm. The TiNbON-25 (101) lattice planes have a d-spacing of 0.35 nm, highlighted in Figure 3.1b. Figure 3.1c and d are representative images of TiNbON-25 loaded with 1 wt % RuO_2; the d-spacing for the (101) planes of anatase (0.35 nm) and (110) planes of RuO_2 (0.32 nm) are highlighted.

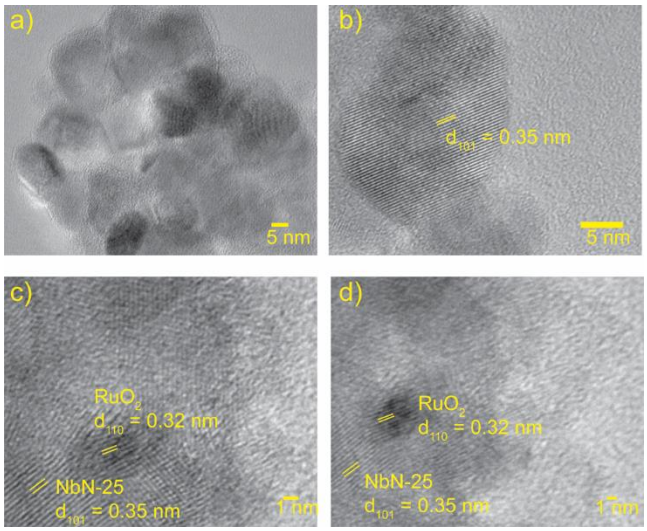

Figure 3.1. TEM images of a) dispersed TiNbON-25 nanoparticles, b) TiNbON-25 d_{101} spacing, and c) and d) 1wt% RuO_2 loaded TiNbON-25.

3.4 Photochemical Water Oxidation with TiNbON-25

Overall water splitting (hydrogen and oxygen evolution on semiconducting metal oxides requires large overpotentials (typically in excess of ~600 mV).[5] Therefore, adding sacrificial electron donors or acceptors is often employed to evaluate either the proton reduction or water oxidation half reactions separately. Our work focuses on the water oxidation reaction. To that end, two common electron acceptors (oxidants) are Ag^+ and IO_3^-, and we choose IO_3^- to avoid plating metallic silver onto our particles and blocking light absorption, which decreases the overall oxygen evolution rate over time. Using iodate as a sacrificial acceptor results in the overall reaction scheme:

$$IO_3^- + 6\ H^+ + 6\ e^- \rightarrow I^- + 3\ H_2O \qquad E^0 = 1.087\ V \qquad (1)$$

$$2\ H_2O \rightarrow 4\ H+ + 4\ e^- + O_2 \qquad E^0 = 1.23\ V \qquad (2)$$

$$2\ IO_3^- \rightarrow 2\ I^- + 3\ O_2 \qquad E^0 = -0.143\ V \qquad (3)$$

Of note, reaction 3 is endergonic under standard conditions and radiant energy is required to carry it out.

TiNbON-25 was tested as a water oxidation photocatalyst in 1 mM $NaIO_3$ under simulated solar irradiation (AM 1.5G filter). Previous work in methylene blue degradation shows that oxidation products, such as benzenesulfonic acid and dimethylaniline, are derived from hydroxyl

radicals and reactive oxygen species formed upon irradiating TiNbON-25.[2] However, water oxidation is not observed, suggesting that hole transfer for water oxidation is slow, and a cocatalyst that can carry out multielectron chemistry may assist in storing photogenerated holes. Under 6-sun illumination of a 1 mM $NaIO_3$ solution with 1 wt % RuO_2 loaded onto TiNbON-25, 15.5 µmol O_2 are observed after 3 h irradiation, illustrated in Figure 3.2. A series of control experiments shown in the inset of Figure 3.2 demonstrates that only the combination of light absorber, cocatalyst, and sacrificial oxidant generate O_2 upon illumination.

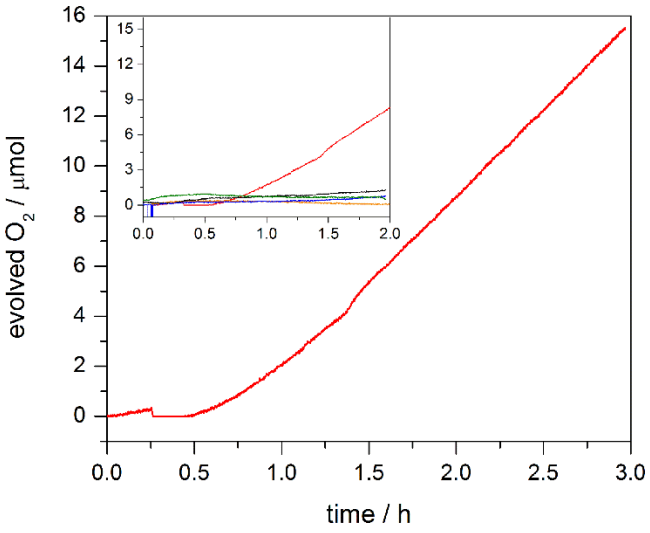

Figure 3.2. O_2 evolution using 50 mg 1 wt% RuO_2 loaded TiNbON-25 powder, 30 mL of 1 mM $NaIO_3$, and 600 mW/cm^2 illumination by a 150 W Xe lamp, AM 1.5G filter (red). **Inset**. Control experiments (all under illumination): 1 mM IO_3^- only (black), 0.5 mg RuO_2 and 1 mM IO_3^- (blue), 1 wt% RuO_2 loaded TiNbON-25 (green), TiNbON-25 and 1 mM IO_3^- (orange).

The rate of the oxygen evolution reaction depends on RuO_2 loading, as shown in Figure 3.3. The water oxidation activity improves with increasing loading percent, reaching a maximum rate at 1 wt % RuO_2. RuO_2 is required to store holes for water oxidation, as has been observed on RuO_x electrodes[6,7] and as deposited on TiO_2 powder.[8] Diffuse reflectance UV-vis spectroscopy shows that loading with 1 wt % RuO_2 does not significantly alter the absorption edge of the photocatalyst (Figure A4). Figure A4 also shows that the UV-vis spectrum of particles loaded with 2 wt % RuO_2 gives a large background absorbance, indicative of competitive light absorption by the dark RuO_2 cocatalyst, which hypothetically blocks absorption by the underlying semiconductor and reduces activity.

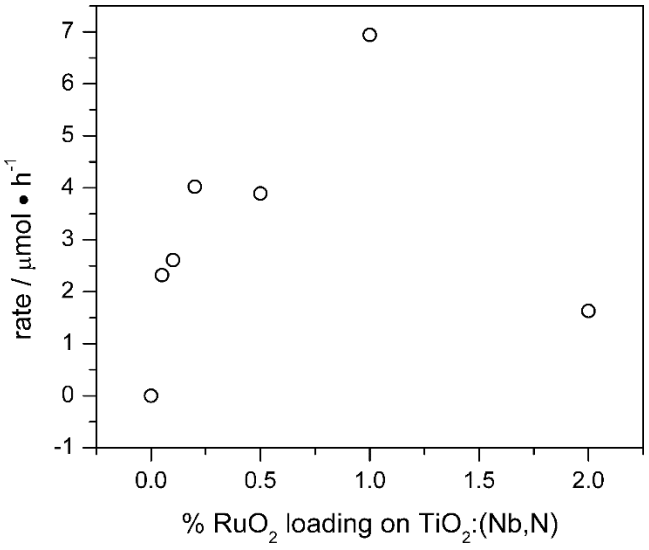

Figure 3.3. Optimization of RuO_2 wt% on TiNbON-25, annealed at 350 °C for 1 hour. Reaction conditions: 50 mg loaded powder, 30 mL of 1 mM $NaIO_3$, 600 mW/cm^2 illumination by a 150 W Xe lamp, AM 1.5G filter.

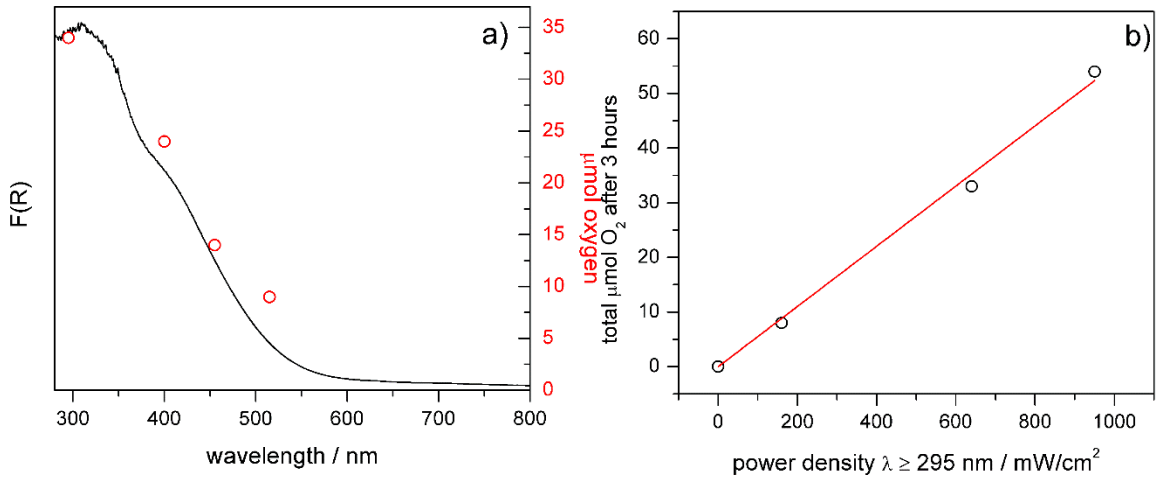

Figure 3.4. a) Dependence of O_2 evolution after three hours of irradiation with cut-on filters for NbN-25 loaded with 1wt% RuO_2 (red). The diffuse reflectance UV-Vis spectrum of TiNbON-25 is also shown (black). Reaction conditions: 50 mg catalyst, 1 mM $NaIO_3$ (30 mL), 150 W Xe lamp fitted with water filter and cut-on filters, and a custom-built Pyrex cell fitted with a quartz window. b) Oxygen evolution *vs*. irradiance for TiNbON-25 loaded with 1 wt% RuO_2. Reaction conditions: 50 mg catalyst, 1 mM $NaIO_3$ (30 mL), 150 W Xe lamp fitted with water filter and 295 nm cut-on filter, and a custom-built Pyrex cell fitted with a quartz window.

Important to establishing photocatalysis, we investigated the wavelength-dependent response of water oxidation on TiNbON-25 using a 150 W Xe lamp fitted with a water filter to eliminate IR light that can cause fluctuating temperatures upon illumination (T = 23 ± 3 °C, Figure A5). The reaction conditions include 50 mg of catalyst in 30 mL of N_2-purged 1 mM $NaIO_3$

solution in an airtight cell. The cut-on filters used to probe oxygen evolution at longer wavelengths include $\lambda \geq 295$ nm, 400 nm, 455 nm, and 515 nm. The irradiance for each experiment was ~600 mW/cm^2. Figure 3.4a highlights that oxygen evolution tracks the absorption profile of the semiconductor. Although the maximum quantity of O_2 (33 μmol) is evolved when UV light is included ($\lambda \geq 295$ nm), it is noteworthy that O_2 evolution persists under solely visible wavelengths. Oxygen detection at longer wavelengths suggests that the N-based impurity levels formed above the O(2p) valence band, due to both Nb^{5+} and N^{3-} in anatase TiO_2, contribute to the photocatalytic activity of this co-incorporated compound for water oxidation. In addition, Figure 3.4b shows that the quantity of O_2 evolved after 3 h using the 295 nm cut-on filter increases linearly with irradiance, meaning that photogenerated charge carriers perform the redox half reactions.

3.5 Kinetic Role and Stability of TiNbON-25

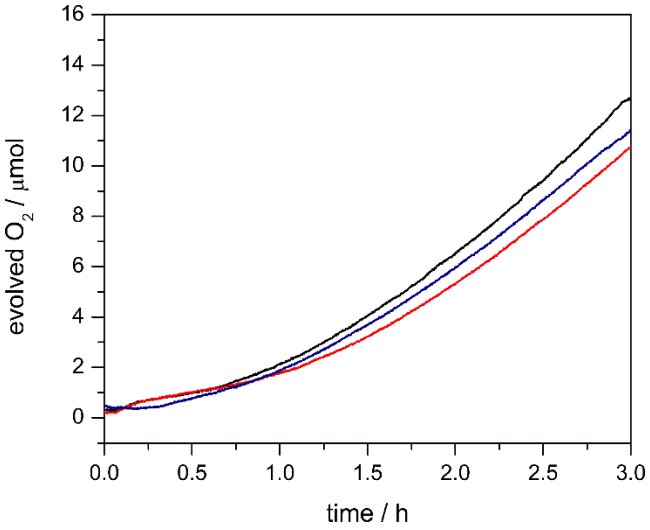

Figure 3.5. Oxygen evolution as a function of time for TiNbON-25 loaded with 1 wt% RuO_2 with different concentrations of $NaIO_3$ sacrificial acceptor.

In order to verify the role of iodate as a sacrificial oxidant, a series of oxygen evolution experiments was performed as a function of IO_3^- concentration. The rate of oxygen evolution was monitored for 3 h under illumination conditions described above ($\lambda \geq 295$ nm) at 1, 2, and 5 mM IO_3^-. Experiments were performed in duplicate. Figure 3.5 shows that the reaction is zero-order in IO_3^-, consistent with the generally accepted notion that, on a heterogeneous catalyst, the number of active catalytic sites is much smaller than the number of molecules of available substrate. Therefore, at practical substrate concentrations, the substrate(s) are always in excess, and the reaction is limited by charge carrier collection efficiency on the powdered catalyst.[9,10]

To determine the catalytic nature of the RuO_2-loaded TiNbON-25, oxygen evolution experiments were carried out in isotopically-labeled $H_2{}^{18}O$, and the product distribution was quantified by gas-phase mass spectrometry. We note that in all instances, there was a background signal from ambient air that could not be eliminated, which made rigorous quantification of evolved gases unreliable. However, in comparing the assays, we observe a 100-fold enhancement in $^{34}O_2$ and a 300-fold enhancement in $^{36}O_2$ from isotopically-enriched solutions, with the total oxygen evolution across all species remaining constant. The observation of $^{36}O_2$, the coupling product from oxidizing two molecules of $H_2{}^{18}O$, confirms that the RuO_2-loaded TiNbON-25 is indeed a photocatalytic material. However, the observed enhancement in $^{34}O_2$ is far above what would be expected statistically given the 3% abundance of $H_2{}^{16}O$ in the reactor. Another possibility is that IO_3^- is intimately involved in the reaction mechanism both as a sacrificial electron acceptor and an O-atom donor (e.g. reaction 3 above), though not as part of the rate-determining step.

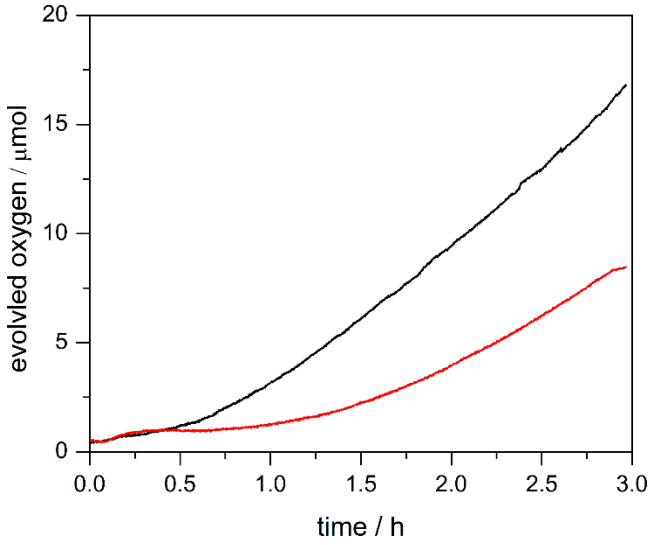

Figure 3.6. Oxygen evolution as a function of time for freshly prepared TiNbON-25 loaded with 1 wt% RuO_2 (black line) and for a second run in which the catalyst was recycled (red line). Reaction conditions: 1 mM $NaIO_3$, 600 mW/cm^2, AM 1.5G filtered light.

Finally, the used powder was recovered from oxygen evolution experiments via filtration and sonicated with deionized water, then dried *in vacuo*. A total of 50 mg of once-used catalyst was then added to the cell with 30 mL of 1 mM $NaIO_3$, and the oxygen evolution rate was quantified. As seen in Figure 3.6, the catalyst retains only half of its activity upon recycling, pointing to a loss of reactive sites either through degradation or surface passivation. Two possible degradation pathways are immediately apparent. Photogenerated electrons from TiNbON-25 can

be transferred to the conduction band of RuO_2, which is lower in energy. Ru^{4+} would then be reduced to soluble Ru^{3+} or Ru^{2+} and leave the surface of the catalyst. Additionally, TiNbON-25 can oxidatively lose N_2 gas according to the reaction[11]

$$2\ N^{3-} + 6\ h^{+} \rightarrow N_2(g) \qquad (4)$$

To elucidate the failure mechanism of the material, the solution was reserved after a typical oxygen evolution experiment, centrifuged, and then filtered to remove all solid materials. The filtrate was then subjected to ICP-AES analysis. The assay reveals no detectable amounts of Ru, Ti, or Nb present in the supernatant solution after 3 h of photocatalytic oxygen evolution. This observation rules out the possibility of RuO_2 reduction and suggests that autooxidation of the light absorber may be the prominent degradation pathway.

3.6 Conclusions

We report the water oxidation activity for a visible light-absorbing anatase phase semiconductor, TiNbON-25, in aqueous $NaIO_3$ solution. TiNbON-25 was modified with polycrystalline RuO_2 at various concentrations. The cocatalyst RuO_2 is necessary in order to evolve oxygen, and water oxidation activity depends on the cocatalyst weight percent loading, with a maximum rate observed for 1 wt % RuO_2. Headspace analysis experiments show that oxidizing $H_2{}^{18}O$ give $^{36}O_2$ as a product, confirming that photocatalytic water oxidation is carried out on 1 wt % RuO_2-loaded TiNbON-25 under visible light irradiation at all absorbed wavelengths ($\lambda \leq 515$ nm).

3.7 References

(1) Breault, T. M.; Bartlett, B. M. Lowering the Band Gap of Anatase-Structured TiO_2 by Coalloying with Nb and N: Electronic Structure and Photocatalytic Degradation of Methylene Blue Dye. *J. Phys. Chem. C* **2012**, *116* (10), 5986–5994.

(2) Breault, T. M.; Bartlett, B. M. Composition Dependence of TiO_2:(Nb,N)-X Compounds on the Rate of Photocatalytic Methylene Blue Dye Degradation. *J. Phys. Chem. C* **2013**, *117* (17), 8611–8618.

(3) Cottineau, T.; Béalu, N.; Gross, P.-A.; Pronkin, S. N.; Keller, N.; Savinova, E. R.; Keller, V. One Step Synthesis of Niobium Doped Titania Nanotube Arrays to Form (N,Nb) Co-Doped TiO_2 with High Visible Light Photoelectrochemical Activity. *J. Mater. Chem. A* **2013**, *1* (6), 2151–2160.

(4) Konstantinou, I. K.; Albanis, T. A. TiO_2-assisted photocatalytic degradation of azo dyes in aqueous solution: kinetic and mechanistic investigations: A review. *Appl. Catal. B: Environ.* **2004**, *49*, 1-14.

(5) Abe, R.; Higashi, M.; Domen, K. Overall Water Splitting under Visible Light through a Two-Step Photoexcitation between TaON and WO_3 in the Presence of an Iodate–Iodide Shuttle Redox Mediator. *Chem. Sus. Chem.* **2011**, *4*, 228-237.

(6) Lodi, G.; Sivieri, E.; De Battisti, A.; Trasatti, S. Ruthenium dioxide-based film electrodes. *J. Appl. Electrochem.* **1978**, *8*, 135−143.
(7) Näslund, L.-Å.; Sánchez-Sánchez, C. M.; Ingason, Á. S.; Bäckström, J.; Herrero, E.; Rosen, J.; Holmin, S. The Role of TiO_2 Doping on RuO_2-Coated Electrodes for the Water Oxidation Reaction. *J. Phys. Chem. C* **2013**, *117*, 6126−6135.
(8) Borgarello, E.; Pelizzetti, E. Dioxygen evolution from inorganic systems. Reactions and catalytic properties of loaded TiO_2 particles in photochemical dioxygen generation. *Inorg. Chim. Acta* **1984**, *91*, 295− 300.
(9) Kudo, A.; Miseki, Y. Heterogeneous Photocatalyst Materials for Water Splitting. *Chem. Soc. Rev.* **2009**, *38* (1), 253–278.
(10) Linsebigler, A. L.; Lu, G.; Yates, J. T., Jr. Photocatalysis on TiO_2 Surfaces: Principles, Mechanisms, and Selected Results. *Chem. Rev.* **1995**, *95*, 735−758.
(11) Hitoki, G.; Takata, T.; Kondo, J. N.; Hara, M.; Kobayashi, H.; Domen, K. An Oxynitride, TaON, as an Efficient Water Oxidation Photocatalyst under Visible Light Irradiation ($\lambda \leq 500$ nm). *Chem. Commun. (Camb).* **2002**, *2* (16), 1698–1699.

Chapter 4
Urea-Glass Preparation of Titanium Niobium Nitrides and Subsequent Oxidation to Photoactive Titanium Niobium Oxynitrides

4.1 Introduction

Recently, co-doping has arisen as a potential strategy for simultaneously introducing visible light absorption into TiO_2-based materials while minimizing electronic structure defects.[1] Co-dopants should be judiciously chosen to charge-compensate each other based on where they are likely to substitute on the TiO_2 lattice. Here, we focus on the TiO_2:(Nb, N) system, as we and others have previously; the excess negative charge supplied by N^{3-} is compensated by Nb^{5+} cations.[2-6] Numerous other dopant pairs such as (W, C),[7] (Ta, N),[8] and (Mo, N)[9,10] have also been tested. These initial reports have studied photo(electro)chemical reaction rates to demonstrate an increase in catalytic competency, hypothetically due to improvements in electronic structure. However, to truly maximize the effectiveness of a co-doped system, it is necessary to restrict the stoichiometry of dopants to charge-compensating ratios, and thus far no study has demonstrated simultaneous rigorous control over cation and anion dopant compositions. Further exploration is needed to uncover synthetic methods that enable such compositional control.

In this work, we present an adaptation of the urea-glass synthesis of transition metal nitrides[11-14] to the quaternary Ti-Nb-O-N system in an attempt to control the stoichiometry of all four elements. We begin by expanding the scope of the urea-glass method to include single-phase

titanium niobium nitride ($Ti_{1-x}Nb_xN$). We show that the as-prepared nitride can be oxidized in air to form an anatase-phase titanium niobium oxynitride with visible light absorption out to ~550 nm.

4.2 Materials Preparation

Urea (Sigma-Aldrich, >99.0%) was recrystallized from hot ethanol before use. The nitrogen used for nitride synthesis was extra-dry grade and was passed through first a P_2O_5 column and then a Cu/Cu_2O column held at 190 °C before introduction into the furnace. Remaining materials were purchased from suppliers as follows and used without further purification: $TiCl_4$ (Sigma-Aldrich, 99.8%), $NbCl_5$ (Strem, 99%), methylene blue (abbrev. MB, Fisher), H_2SO_4 (Fisher, 66° Baume), hydrofluoric acid (Fisher, 48-51%).

Metal nitride samples were prepared by the urea-glass method as described by Giordano, *et al.*[12] Briefly, 3.51 mmol of metal chloride was reacted with 1.6 mL ethanol and allowed to cool before a specified amount of urea was added. We found a "urea-to-valence ratio" *R*, defined in Equation 1 where *x* is the mole fraction of Nb of total metals, necessary to isolate pure phase nitrides. An *R* value of 1 was used for each sample unless otherwise noted.

$$R = \frac{mol\ urea}{5x + 4(1 - x)}$$

The mixture was stirred until dissolved and heated in flowing nitrogen (5 mL/min) at 750 °C with a heating and cooling rate of 3 °C/min. The reactor consists of a 1" diameter quartz tube 17" in length open with a joint for an O-ring at one end. The opposite end has a ¼" quartz tube that serves as the gas outlet that attaches 1" from the back of the larger tube. A quartz boat 2" long x ½" wide x 3/8" deep with a capacity of ~2.2 mL was used to hold the reaction mixture. The reactor was sealed by attaching a Pyrex nozzle with stopcock to the quartz tube using an O-ring and a c-clamp. A bronze crystalline product was obtained after heating in all cases. The product was ground and stored for further use. A second oxidation step was carried out by annealing 25 mg batches of urea-glass products in a box furnace in static ambient air atmosphere at 550 °C for 3 h with a heating and cooling rate of 10 °C/min.

4.3 Materials Characterization and Compositional Analysis

Powder X-ray diffraction measurements were carried out on a Panalytical Empyrean powder X-ray diffractometer using Cu Kα radiation (λ = 1.5418 Å) in θ-θ geometry with a sample stage rotating at 16 rpm. Thermogravimetric analysis was performed on a TA Q50 TGA with a platinum pan, heating rate of 10 °C/min, and a compressed air flow rate of 60 mL/min. Scanning electron microscopy (SEM) and energy dispersive X-ray spectroscopy (EDX) were performed using a JEOL-7800FLV FE scanning electron microscope. A beam voltage of 15 kV was used for imaging and for EDX. UV-Vis spectra were acquired on a Cary 5000 UV-Vis NIR Spectrophotometer. For powder measurements, a Harrick Praying Mantis diffuse reflectance accessory was employed and $BaSO_4$ was used as a 100% reflectance standard. Electron paramagnetic resonance (EPR) spectroscopy was acquired at 120 K in the X-band range using a Bruker EMX electron spin resonance spectrometer with a Bruker 4102-ST cavity. 10 mg samples were suspended in ethylene glycol before acquisition using a microwave frequency of 9.26 GHz.

Metal ratios for titanium niobium oxynitrides were measured using EDX spectroscopy as described above.

Nitrogen content was determined for $Ti_{0.95}Nb_{0.05}ON$ (TiNbON-5) by the Kjeldahl method, in which nitride is converted to ammonia, transferred from the sample, and titrated. A 1042 mg sample of TiNbON-5 was dissolved in a Teflon beaker in 15 mL a 1:1:1 by volume solution of H_2O, concentrated H_2SO_4, and 50% HF by stirring overnight at room temperature. The resulting solution was quantitatively transferred to a distillation apparatus and sealed such that the only pressure outlet to the system was through a flask filled with 30 mL of 0.5 M aqueous H_3BO_3 and 10 drops of 0.1% methyl red in ethanol as an indicator. 30 mL of 50% NaOH solution was admitted to the sample flask through a liquid addition funnel, causing rapid heating and gas evolution in the sample flask. The sample was then boiled for 1.5 h to ensure complete ammonia transfer. The expected color change from bright pink to yellow was observed in the methyl red indicator. The receiving solution was then titrated with 0.035 M H_2SO_4 until methyl red turned pink again, using a control solution of methyl red in boric acid as a color indicator. Control determinations on 35 mg samples of NH_4Cl revealed a standard overdetermination of 4-7 mass %.

Brunauer-Emmet-Teller surface areas for TiNbON were calculated from approximations of N2 sorption data collected on a Quantachrome NOVA e-series 4200 surface area analyzer.

Measurements were carried out at 77 K using ultra-high purity N2 (99.999%, Cryogenic). Approximately 75 mg sample was used for each run.

4.4 Methylene Blue Photodegradation Procedure

A 2 ppm solution of methylene blue (from methylene blue dihydrate) was prepared in 18.2 MΩ water (Millipore). For kinetics experiments, 20 mg of experimental powder was added to a 30 mL quartz tube. 20 mL of methylene blue solution was added and the mixture was allowed to stir under complete exclusion of light for 3 h. The tube was then placed in front of a Newport-Oriel 150 Xe arc lamp solar simulator equipped with AM 1.5 G and water filters with a front-cell irradiance of 500 mW/cm^2 (5 suns). For visible light-only experiments, a 400 nm cut-on filter was inserted between the lamp aperture and reactor after the lamp had been adjusted to the appropriate power resulting in a final irradiance of 170 mW/cm^2. 4 mL aliquots of the solution were removed at 0 min, 30 min, and 60 min reaction time, centrifuged at 3500 rpm for 3 min, and the absorbance spectrum of the supernatant solution was recorded between 400 and 800 nm before the aliquot was reintroduced to the kinetics experiment. Where necessary to correct for background absorption by particles still suspended after centrifugation, a polynomial baseline was subtracted from the absorption spectra. The concentration of methylene blue at each timepoint was calculated using the Lambert-Beer law based on the maximum of the absorption feature. Rate constants were derived from concentration data using the first-order Langmuir-Hinshelwood model

$$rate = -\ln(\frac{C}{C_0})kt$$

where C/C_0 is the ratio of the concentration of methylene blue at time t to the concentration at time 0, k is the rate constant, and t is the time in minutes. The amount of dye adsorbed to the particles per gram does not appear in the rate law but rather in a separate factor

$$q_e = \frac{K_L q_m C_e}{1 + K_L C_e}$$

where q_e is the equilibrium dye coverage (mg/g), q_m is the maximum dye coverage (i.e. the limit of a perfect monolayer), K_L is the equilibrium constant for the adsorption reaction, and C_e is the concentration of the dye. We have not measured full adsorption isotherms in this work, and so we report only relative adsorption values q_{rel} for our series of titanium niobium oxynitrides.

4.5 Urea-glass Synthesis of $Ti_{1-x}Nb_xN$

The powder X-ray diffraction patterns of $Ti_{1-x}Nb_xN$ prepared by the urea-glass method are shown in Figure 4.1 (with an added internal standard of tungsten powder). Each pattern indexes to the rocksalt phase expected for TiN with no crystalline impurities such as the oxide phases. Phase segregation into a mixture of nitrides is not observed for any niobium composition, based on the absence of additional reflections at higher angles that would arise from the thermodynamically stable hexagonal phase of NbN. Additionally, by correcting each pattern using the [110] reflection of the W internal standard, a progressive shift of the nitride reflections to lower angles is observed. This observation is consistent the lattice expansion expected when adding the larger Nb^{3+} ion to a Ti^{3+} site in the crystal structure according to Vegard's law and is further evidence of solid solution behavior.

For a Nb content of 15 mol %, we examined the effect of decreasing *R* on product identity in an attempt to isolate titanium niobium oxynitride in a single step. Figure B1 contains powder x-ray diffraction patterns of the resulting products, which vary in appearance from black to grey. All are multiphasic mixtures of anatase TiO_2, rutile TiO_2, and rocksalt TiN, and so these products were not further analyzed.

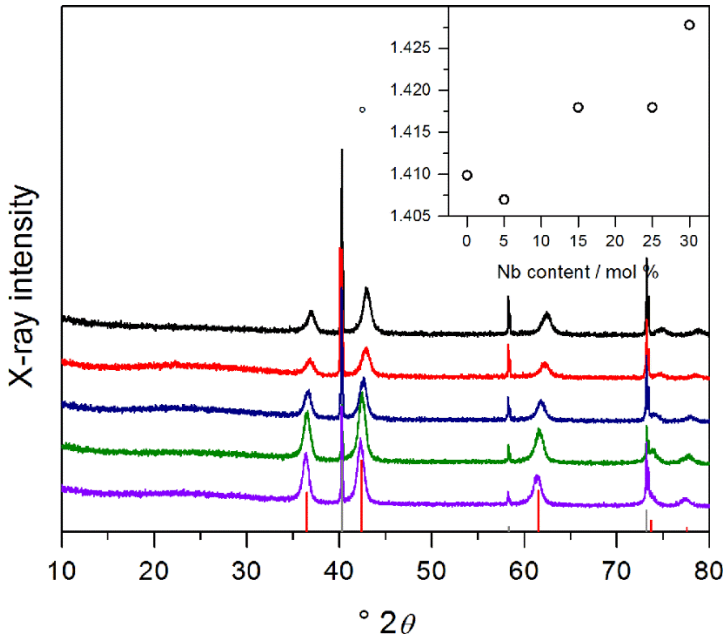

Figure 4.1. PXRD patterns for $Ti_{1-x}Nb_xN$ prepared by urea-glass synthesis with tungsten powder added as an internal standard. Nb content increases from the top of the graph to the bottom. Black: $x = 0$; red: $x = 5$; blue: $x = 15$; green: $x = 25$; purple: $x = 30$.

Scanning electron micrographs of representative nitride samples are shown in Figure B2. Contrary to what is observed by previous authors on the urea-glass method, we do not isolate monodisperse nanoparticles of any nitride sample. Instead, we observe large sheet-like particles that are tens of microns in length and width with variable thickness interspersed with smaller particles. We suspect that the flow rate of nitrogen gas used in the reaction may play a role in determining particle sizes and morphologies by influencing the evaporation rate of ethanol from the reaction gel. The nitrogen flow rate has not been specified in previous reports on the synthesis.

4.6 Nitride Oxidations

To understand the behavior of $Ti_{1-x}Nb_xN$ upon heating in air, we turned to thermogravimetric analysis (TGA). The TGA traces, recorded in flowing air, for each compound are shown in Figure 4.2. Generally, we observe a small mass loss at the beginning of heating, attributed to water loss from the surface of the compound. Secondly, a mass gain due to the oxidation of the nitride material is observed. This mass gain event appears to cease after about 500 °C for each compound, at which point a mass loss attributed to the combustion of residual carbon in the material takes over. The final event is a weak mass gain (except for pure TiN, where it is more prominent) which is explained by continued oxidation of the material to phase-segregated mixtures of rutile TiO_2 and $TiNb_2O_7$.

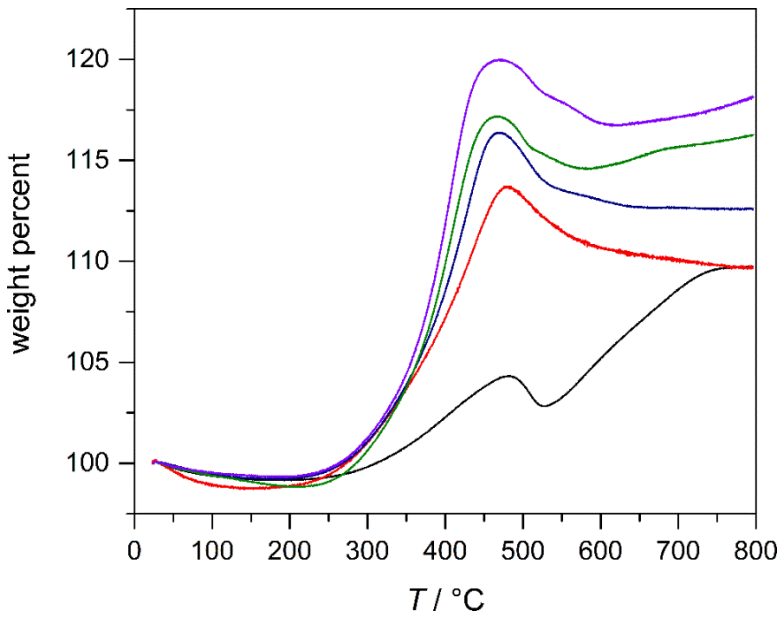

Figure 4.2. Thermogravimetric analysis traces recorded in flowing air for $Ti_{1-x}Nb_xN$ compounds. Black: $x = 0$; red: $x = 5$; blue: $x = 15$; green: $x = 25$; purple: $x = 30$.

Using these data as a guide, we oxidized $Ti_{1-x}Nb_xN$ powders in air at 550 °C in hopes of identifying the intermediate phase observed in the TGA traces. In each case, a yellow powder is isolated. The yellow materials are identified as antase phase by PXRD (Figure 4.3) and do not exhibit any notable change in particle size and morphology compared to the nitrides isolated from urea-glass synthesis (Figure B3). An impurity peak near 27° 2θ indicates the presence of small quantities of a rutile phase. Given that no rutile phase is observed in the nitrides before oxidation and that 550 °C is close to the anatase-rutile transition temperature for pure TiO_2, we attribute rutile formation as an inevitable by-product of the heating step. The broad, low-intensity peaks in the PXRD patterns suggest that the large particles seen by SEM are agglomerates of many small crystalline grains.

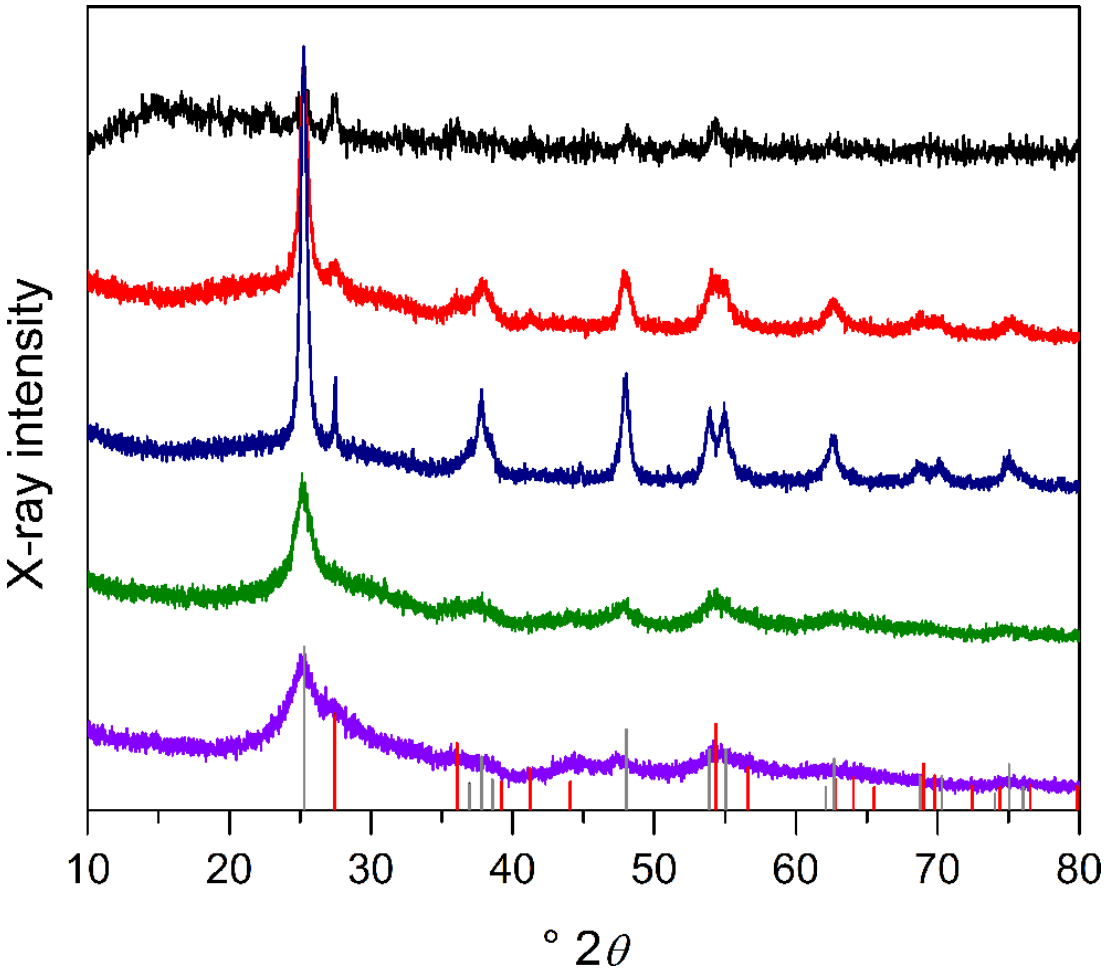

Figure 4.3. PXRD patterns for $Ti_{1-x}Nb_xN$ after oxidation in air (TiNbON-*x*). Black: $x = 0$; red: $x = 5$; blue: $x = 15$; green: $x = 25$; purple: $x = 30$. Gray and red reference patterns are anatase and rutile TiO_2, respectively.

Curiously, the TGA data show a mass gain upon oxidation that increases with increasing niobium content; such behavior is exactly contrary to what would be expected for a series of materials with mass percentages increasingly dominated by metals. Additionally, multiple reports on the urea-glass method have demonstrated an increase in residual carbon as the urea content of the reactive solution increases, as it does when one maintains a constant urea:valence ratio, *R*, while increasing Nb^{5+} content. However, in the absence of impurity phases in the PXRD patterns that would otherwise confound the TGA traces, we must attribute this observation to a decrease in the carbon content of $Ti_{1-x}Nb_xN$ with increasing Nb content. Compositional analysis reported by Giordano *et al.* demonstrate that NbN prepared by this synthetic route contains significantly less carbon than TiN prepared in an analogous way,[12] suggesting that urea decomposition under reactive contitions may be more efficient in the presence of Nb^{5+} than without.

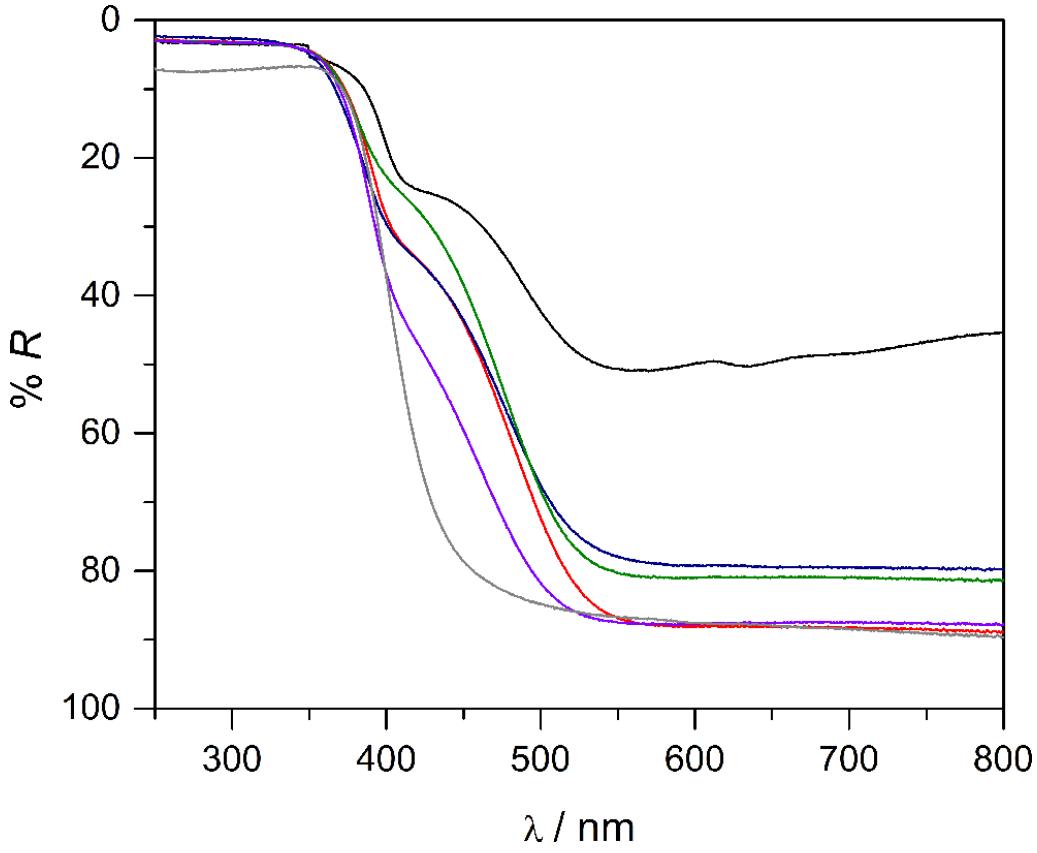

Figure 4.4. Diffuse reflectance spectra for TiNbON-*x* compounds. Black: *x* = 0; red: *x* = 5; blue: *x* = 15; green: *x* = 25; purple: *x* = 30. Degussa P25 TiO_2 is shown in grey for reference.

The diffuse reflectance spectra of the oxidized nitrides are shown in Figure 4.4. The spectra are characterized by absorption edges near 550 nm, with the exception of the TiNbON-30 sample

which begins closer to 525 nm. Additionally, the TiNbON-0 sample exhibits significant background absorption out to long wavelengths, consistent with a high concentration of defect states in the midgap region of the material's electronic structure. The absorption edges are brought about by a shoulder peak that appears to be extended from that of pure TiO_2 by an extent which varies with Nb content. The peak shape and low intensity of the new absorption are suggestive of localized defect-based transitions, so we are reluctant to conclude that we have narrowed the TiO_2 band gap – particularly because the smallest peak shoulder is observed for TiNbON-30, the compound most concentrated in Nb.

4.7 Methylene Blue Photomineralization Rate Constants

As a benchmark for photochemical activity, we measured the rate of photomineralization of methylene blue over our series of TiNbON compounds. The intimate details of the photomineralization reaction over similar compounds have been discussed in our previous work.[3] As the methylene blue molecule can be destroyed both oxidatively and reductively by the semiconductor through a variety of conceivable pathways, we compare the rates of methylene blue degradation here as a preliminary indication of the internal charge transport and collection efficiencies relative to recombination across the series of compounds presented. We note here that, consistent with previous results, a positive correlation between Nb content and surface adsorbed methylene blue during the dark adsorption period preceding illumination is observed (Table B2).

A comparison of the first-order Langmuir-Hinshelwood rate constants for methylene blue degradation can be found in Figure 4.5. The observed rate constants demonstrate an optimum Nb content for this series of compounds of between 5 and 15%, with the reaction rate dropping off by a factor of ~1.5 at higher Nb concentrations. This finding contrasts with our previous results on this compositional system which showed an optimum Nb concentration of 25%.[3] Notably, TiNbON-5 and TiNbON-15 degrade methylene blue faster than TiNbON-0, demonstrating the importance of co-doping/co-alloying in efficiently harvesting visible light photons. The observed reactivity cannot be attributed to differences in surface area (Table B2) as no correlation between Nb content and BET surface area is observed for this series of compounds.

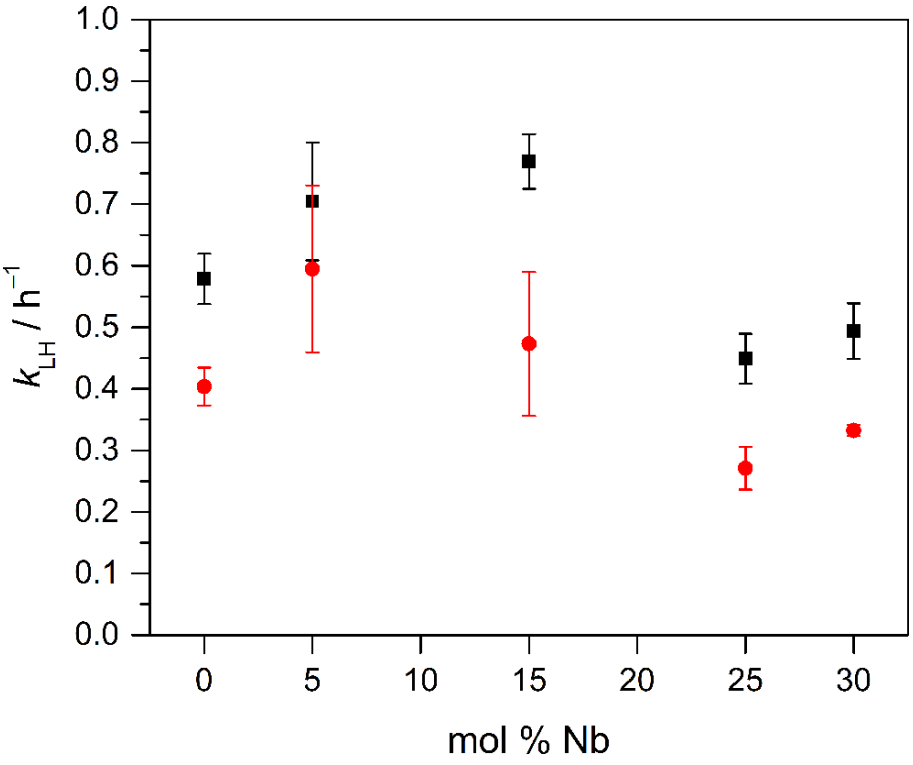

Figure 4.5. First-order Langmuir-Hinshelwood rate constants for photochemical methylene blue degradation over TiNbON-*x* as a function of Nb concentration. Data are shown for reactions run with the full AM1.5G spectrum (black squares) and for AM1.5G modified by a 400 nm cut-on filter (red circles). Error bars shown are the error in the fit for the rate law for the average concentration vs. time data for two trials.

Additionally, we measured how the rate of methylene blue degradation changes when TiNbON compounds are excited by visible light alone. We observe a decrease in reaction rate across all compounds consistent with the decreased incident lamp power after inserting the 400 nm cut-on filter (500 mW/cm^2 for full-spectrum, 170 mW/cm^2 with filter). The control compound, TiNbON-0, loses 30% of its activity when wavelengths above 400 nm are removed from the excitation spectrum. This loss is diminished for TiNbON-5, which experiences only a 16% decrease in photochemical rate despite a 17.5% attenuation in irradiance with the filter in place. An equal or greater loss compared to TiNbON-0 is observed for TiNbON-15 (39%), TiNbON-25 (40%) and TiNbON-30 (33%). On the basis of overall reaction rate and on the relative efficiencies of visible light-driven photochemsitry, we conclude from these data that TiNbON-5 is the compound with nearest to the ideal composition for this quaternary system.

4.8 Compositional Analysis Results

On the basis of our methylene blue photodegradation results, we chose to fully investigate the composition for TiNbON-5. Quantification of nitrogen content for titanium oxynitrides has typically relied on X-ray photoelectron spectroscopy. However, the low atomic weight of the nitrogen nucleus leads to weak signal, and our samples did not provide adequately strong signal for reliable chemical analysis. Instead, we quantified Ti:Nb ratios using EDX spectroscopy (Table B1) and N using the Kjeldahl method as described above, which determines nitride content as ammonia. The Kjeldahl determination yielded 4.35 mg N in 1042 mg total material; therefore, for TiNbON-5, we find a chemical formula of $Ti_{0.92}Nb_{0.08}O_{1.97}N_{0.03}$.Using this compositional analysis, we report a lower bound of the oxygen content by assuming that each nitrogen anion substitutionally occupies an oxygen site.

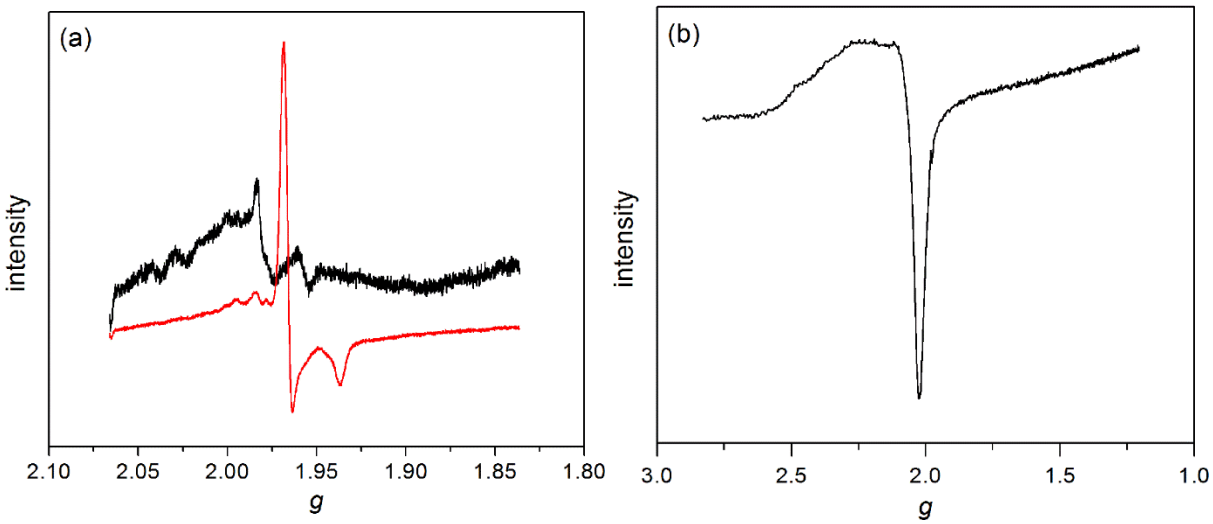

Figure 4.6. a) EPR spectra for TiNbON-0 (black, multiplied 5x) and TiNbON-5 (red). b) EPR spectrum for TiNbON-25. Spectra were acquired at a microwave frequency of 9.26 GHz at 120 K using a modulation frequency of 10 GHz.

We do not anticipate large differences in the nitrogen content across the series of niobium contents reported above, which raises the question of why TiNbON-5 exhibits a superior photochemical rate for MB degradation compared to the more highly-substituted TiNbON compounds. To further characterize these compounds, we turned to EPR spectroscopy and attempted to analyze the defect identity for TiNbON-0, TiNbON-5, and TiNbON-25. As seen in Figure 4.6a, both TiNbON-0 and TiNbON-5 exhibit localized anisotropic resonances consistent with reduced metal centers. The *g*-values for TiNbON-0 (g_y = 1.984, g_x = 1.974, g_z = 1.953) are

consistent with reduced Ti^{3+} present in the anatase structure.[2] However, in contrast to our previous work, we find that the resonance in TiNbON-5 is shifted to slightly lower *g*-values (g_y = 1.968, g_x = 1.963, g_z = 1.937), which is more consistent with an Nb^{4+} donor state than a Ti^{3+}.[15,16] Comparatively smaller peaks at lower g-values suggest the presence of some Ti^{3+} in TiNbON-5 as well. Both of these spectra are in sharp contrast to TiNbON-25, which exhibits a very broad resonance centered near a *g*-value of 2 (Figure 4.6b). The breadth of this spectral feature suggests a highly delocalized electron defect. We hypothesize that the high Nb fraction in TiNbON-25 allows nearby Nb ions to mix atomic orbitals to form bands, which induces electron delocalization from Nb^{4+} centers. Localized Nb^{4+} states measured in TiNbON-5 may serve as shallow electron traps based on the predicted position of Nb orbitals in the TiNbON electronic structure;[17] shallow trap states have been shown in some transition metal-doped TiO_2 samples to increase photochemical activity in small concentrations[18] though that finding is not widely generalizable.[17]

4.9 Conclusions

Synthetic methods for the preparation of co-doped titania that enable rigorous control of multiple compositional elements remain elusive. In this report, we have expanded upon the known urea-glass method for the preparation of pure metal nitrides to access mixed-metal nitrides of a single phase up to 30 mol % Nb. The nitrides exhibit complex oxidation behavior in flowing air, showing a plateau of stability near 550 °C. Nitrides heated to this temperature in static air are competent photocatalysts for methylene blue photomineralization, a common photochemical benchmarking reaction. We have identified a niobium concentration near 8 mol % as optimal in this series of compounds.

4.10 References

(1) Brancho, J. J.; Bartlett, B. M. Challenges in Co-Alloyed Titanium Oxynitrides, a Promising Class of Photochemically Active Materials. *Chem. Mater.* **2015**, *27* (21), 7207–7217.

(2) Breault, T. M.; Bartlett, B. M. Lowering the Band Gap of Anatase-Structured TiO_2 by Coalloying with Nb and N: Electronic Structure and Photocatalytic Degradation of Methylene Blue Dye. *J. Phys. Chem. C* **2012**, *116* (10), 5986–5994.

(3) Breault, T. M.; Bartlett, B. M. Composition Dependence of TiO_2:(Nb,N)-X Compounds on the Rate of Photocatalytic Methylene Blue Dye Degradation. *J. Phys. Chem. C* **2013**, *117* (17), 8611–8618.

(4) Breault, T. M.; Brancho, J. J.; Guo, P.; Bartlett, B. M. Visible Light Water Oxidation Using a Co-Catalyst Loaded Anatase-Structured $Ti_{1-(5x/4)}Nb_xO_{2-Y-\delta}N_y$ Compound. *Inorg. Chem.* **2013**, *52* (16), 9363–9368.

(5) Cottineau, T.; Béalu, N.; Gross, P.-A.; Pronkin, S. N.; Keller, N.; Savinova, E. R.; Keller, V. One Step Synthesis of Niobium Doped Titania Nanotube Arrays to Form (N,Nb) Co-Doped TiO_2 with High Visible Light Photoelectrochemical Activity. *J. Mater. Chem. A* **2013**, *1* (6), 2151–2160.
(6) Chadwick, N. P.; Glover, E. N. K.; Sathasivam, S.; Basahel, S. N.; Althabaiti, S. a.; Alyoubi, A. O.; Parkin, I. P.; Carmalt, C. J. Photo-Activity and Low Resistivity in N/Nb Co-Doped TiO_2 Thin Films by Combinatorial AACVD. *J. Mater. Chem. A* **2016**, *4* (2), 407–415.
(7) Cho, I. S.; Lee, C. H.; Feng, Y.; Logar, M.; Rao, P. M.; Cai, L.; Kim, D. R.; Sinclair, R.; Zheng, X. Codoping Titanium Dioxide Nanowires with Tungsten and Carbon for Enhanced Photoelectrochemical Performance. *Nat. Commun.* **2013**, *4*, 1723.
(8) Hoang, S.; Guo, S.; Mullins, C. B. Coincorporation of N and Ta into TiO_2 Nanowires for Visible Light Driven Photoelectrochemical Water Oxidation. *J. Phys. Chem. C* **2012**, *116* (44), 23283–23290.
(9) Ruddy, D. A.; Reid, O. G.; Leonard, B. M.; Pylypenko, S.; Neale, N. R. Non-Aqueous Thermolytic Route to Oxynitride Photomaterials Using Molecular Precursors $Ti(OtBu)_4$ and $N{\equiv}Mo(OtBu)_3$. *J. Mater. Chem. A* **2013**, *1* (45), 14066.
(10) Liu, H.; Lu, Z.; Yue, L.; Liu, J.; Gan, Z.; Shu, C.; Zhang, T.; Shi, J.; Xiong, R. (Mo+N) Codoped TiO_2 for Enhanced Visible-Light Photoactivity. *Appl. Surf. Sci.* **2011**, *257* (22), 9355–9361.
(11) Giordano, C.; Erpen, C.; Yao, W.; Antonietti, M. Synthesis of Mo and W Carbide and Nitride Nanoparticles via a Simple "Urea Glass" Route. *Nano Lett.* **2008**, *8* (12), 4659–4663.
(12) Giordano, C.; Erpen, C.; Yao, W.; Milke, B.; Antonietti, M. Metal Nitride and Metal Carbide Nanoparticles by a Soft Urea Pathway. *Chem. Mater.* **2009**, *21* (21), 5136–5144.
(13) Gao, Q.; Giordano, C.; Antonietti, M. Controlled Synthesis of Tantalum Oxynitride and Nitride Nanoparticles. *Small* **2011**, *7* (23), 3334–3340.
(14) Molinari, V.; Giordano, C.; Antonietti, M.; Esposito, D. Titanium Nitride-Nickel Nanocomposite as Heterogeneous Catalyst for the Hydrogenolysis of Aryl Ethers. *J. Am. Chem. Soc.* **2014**, *136* (5), 1758–1761.
(15) Chester, P. F. Cross-Doping Agents for Rutile Masers. *J. Appl. Phys.* **1961**, *32* (5), 866–868.
(16) Kiwi, J.; Suss, J. T.; Szapiro, S. EPR Spectra of Niobium-Doped TiO_2 and Imiplications for Water Photocleavage Processes. *Chem. Phys. Lett.* **1984**, *106* (1–2), 135–138.
(17) Ma, X.; Wu, Y.; Lu, Y.; Xu, J.; Wang, Y.; Zhu, Y. Effect of Compensated Codoping on the Photoelectrochemical Properties of Anatase TiO_2 Photocatalyst. *J. Phys. Chem. C* **2011**, *115* (34), 16963–16969.
(18) Zhang, Z.; Wang, C.-C.; Zakaria, R.; Ying, J. Y. Role of Particle Size in Nanocrystalline TiO_2-Based Photocatalysts. *J. Phys. Chem. B* **1998**, *102* (52), 10871–10878.

Chapter 5

Preparation of Titanium Niobium Oxynitride by an Improved Urea-Glass Synthesis Using a $CaCO_3$ Additive

5.1 Introduction

The work presented in the previous chapter demonstrates the feasibility of preparing titanium niobium oxynitride via the known urea-glass synthesis using excess urea. An attractive feature of the urea-glass method is the flexibility to easily modify the concentrations of metal precursors and/or the urea, which supplies the nitrogen equivalents needed to prepare nitride materials. Hypothetically, the nitrogen content of a given product can be decreased from stoichiometric nitride by decreasing the urea in the precursor solution. However, as demonstrated in Chapter 4, such a modification produces a mixture of anatase and rutile TiO_2-like products with rocksalt $Ti_{1-x}Nb_xN$ as well. A phase-pure product, especially without $Ti_{1-x}Nb_xN$ which is not anticipated to be photoactive, is desired.

An important modification to the urea-glass method has been demonstrated in the synthesis of tantalum oxynitride, TaON.[1] Attempts to prepare TaON by the standard urea-glass method results in multiphasic mixtures of tantalum nitrides and oxynitrides over a range of urea contents. Incorporating an alkaline-earth cation in the form of MCO_3 was demonstrated to improve the homogeneity of the observed products, and the authors succeed in isolating a two-phase mixture of β- and γ-TaON.

The authors propose that the product homogeneity is improved by decreased reaction rate. The alkaline-earth M^{2+} cation forms a stabilizing complex with urea, which is already complexed by Ta^{5+} in the reaction mixture. The stabilized Ta^{5+}-urea-M^{2+} complex decomposes more slowly compared to Ta^{5+}-urea on its own. As a result, NH_3 is released by urea decomposition at a decreased rate – a rate more proportional to the rate at which gaseous NH_3 can reduce and nitride the amorphous metal alkoxide matrix that forms upon heating the urea-glass solution.

No further reports on using an alkaline-earth-assisted urea-glass method to prepare transition metal oxynitrides. In this chapter, the method is extended to attempt facilitated preparation of TiNbON photocatalysts.

5.2 Materials Preparation

3.51 mmol combined of $TiCl_4$ and $NbCl_5$ in desired stoichiometry were slowly added to 1.6 mL of 200-proof ethanol and stirred to dissolve. Upon cooling of the solution, an appropriate amount of urea was added based on the urea:valence ratio chosen for the synthesis. The solution was stirred until urea was fully dissolved before 351 mg of $CaCO_3$ was added. The reaction was stirred until foaming ceased, transferred to a quartz reaction tube, and heated to 500 °C or 750 °C for 3 h with a heating rate of 3 ºC/min in an MTI tube furnace under flowing nitrogen (~5 mL/min) Soluble Ca^{2+}-containing by-products were removed by suspending 30 mg of crude black or grey product in 10 mL of 6 M HCl and sonicating for 3 h, after which the products were isolated by centrifugation, washed 3 times with deionized water, and dried in vacuo at 60 ºC. Where noted, samples were subjected to another air oxidation step by adding 25 mg of acid-washed product to a quartz crucible and heating at 400 ºC for 3 h in air with a heating rate of 10 ºC/min in an MTI box furnace.

5.3 Materials Characterization

Powder X-ray diffraction measurements were carried out on a Panalyticial Empyrean powder X-ray diffractometer using Cu Kα radiation (λ = 1.5418 Å) in θ-θ geometry with a sample stage rotating at 16 rpm. Thermogravimetric analysis was performed on a TA Q50 TGA with a platinum pan, heating rate of 10 °C/min, and a compressed air flow rate of 60 mL/min. Scanning electron microscopy (SEM) was performed using a Zeiss LEO 1455 VP scanning electron microscope with a tungsten filament. UV-Vis spectra were acquired on a Cary 5000 UV-Vis NIR

Spectrophotometer. For diffuse reflectance measurements, a Harrick Praying Mantis diffuse reflectance accessory was employed and $BaSO_4$ was used as a 100% reflectance standard. Solid-state absorption spectra were acquired on the same spectrometer by grinding 1 mg of the compound of interest with 99 mg of KBr to mix thoroughly, then pressing in a stainless steel die by tightening opposing bolts with handheld wrenches. A pure KBr pellet was used as the reference sample.

5.4 Methylene Blue Photodegradation Procedure

A 2 ppm solution of methylene blue (from methylene blue dihydrate) was prepared in 18.2 MΩ water (Millipore). For kinetics experiments, 15 mg of experimental powder was added to a 30 mL quartz tube. 15 mL of methylene blue solution was added and the mixture was allowed to stir under complete exclusion of light for 3 h. The tube was then placed in front of a Newport-Oriel 150 Xe arc lamp solar simulator equipped with AM 1.5 G and water filters with a front-cell irradiance of 500 mW/cm^2 (5 suns). 4 mL aliquots of the solution were removed at 0 min, 30 min, and 60 min reaction time, centrifuged at 3500 rpm for 3 min, and the absorbance spectrum of the supernatant solution was recorded between 400 and 800 nm before the aliquot was reintroduced to the kinetics experiment. A polynomial baseline was subtracted from the absorption spectra to correct for scattering by suspended particles not removed by centrifugation. The concentration of methylene blue at each timepoint was calculated using the Lambert-Beer law based on the maximum of the absorption feature. Rate constants were derived from concentration data using the first-order Langmuir-Hinshelwood model

$$rate = -\ln(\frac{C}{C_0})kt$$

where C/C_0 is the ratio of the concentration of methylene blue at time t to the concentration at time 0, k is the rate constant, and t is the time in minutes.

5.5 Effect of Temperature and Urea Content on Product Composition

Initial attempts to prepare TiNbON by the Ca^{2+}-assisted urea-glass synthesis were carried out with a 750 °C heating step according to previous reports.[1,2] Additionally, a nominal metal ratio of $Ti_{0.85}Nb_{0.15}$ was used to assist in facile identification of impurities by PXRD. For R = 0.7 and 0.1 (see Chapter 4), a multiphasic PXRD pattern (Figure 5.1a) was observed containing rutile $Ti_{0.85}Nb_{0.15}ON$, and a $CaNb_2O_6$ fersmite phase not removed during the acid wash step. (The high-

intensity peak near 45 º 2θ is from the aluminum sample holder.) In $Ti_{1-x}Nb_xO_2$ phases, it is observed that niobium is extruded from the crystal structure at extremely high temperatures, resulting in the formation of niobium-rich Nb_2O_5 and $TiNb_2O_7$ phases.[3,4] Based on this observation, we hypothesized that a reduced-temperature synthesis would prevent phase segregation and the formation of insoluble fersmite. Repeated preparations at 500 °C resulted in a two-phase mixture of anatase $Ti_{0.85}Nb_{0.15}ON$ and $CaCl_2•2H_2O$, the latter being removed in the acid treatment to leave only anatase (Figure 5.1b).

After these initial synthetic investigations, the Nb content was reduced to $Ti_{0.95}Nb_{0.05}$ consistent with photochemical results from Chapter 4. PXRD patterns after acid washing for $Ti_{0.95}Nb_{0.05}ON$ prepared at *R* = 0.7, 0.5, and 0.3 can be found in Figure 5.2a. Each *R* ratio results in an anatase product, though the color of the product differs significantly as shown in Figure 5.2b. R = 0.7 contains either a $CaTiO_3$ perovskite impurity or a rutile Nb_2O_5 impurity. The impurity peak at 50 º 2θ for R = 0.3 is ammonium chloride, likely due to sample cross-contamination during workup and analysis.

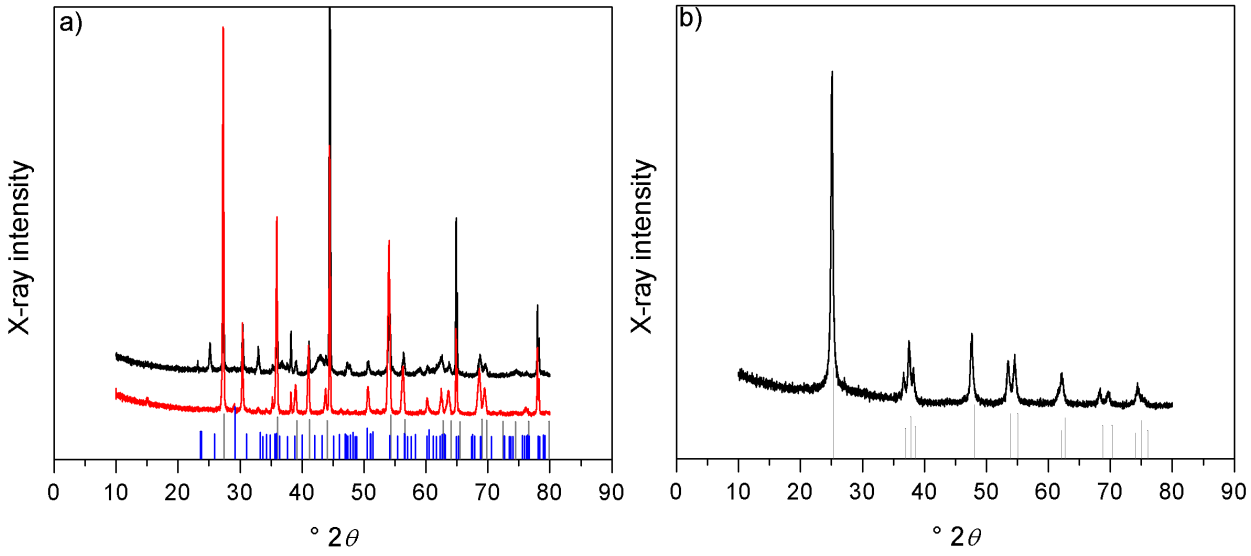

Figure 5.1. PXRD patterns for TiNbON-15 prepared by Ca2+ urea-glass synthesis. a) Reactions carried out at 750 ºC and R = 0.7 (black), R = 0.1 (red). Vertical lines represent reference patterns for rutile TiO_2 (grey) and fersmite $CaNb_2O_6$ (blue). b) Reaction carried out at 500 ºC and R = 0.7. Grey vertical lines represent reference pattern for anatase TiO_2.

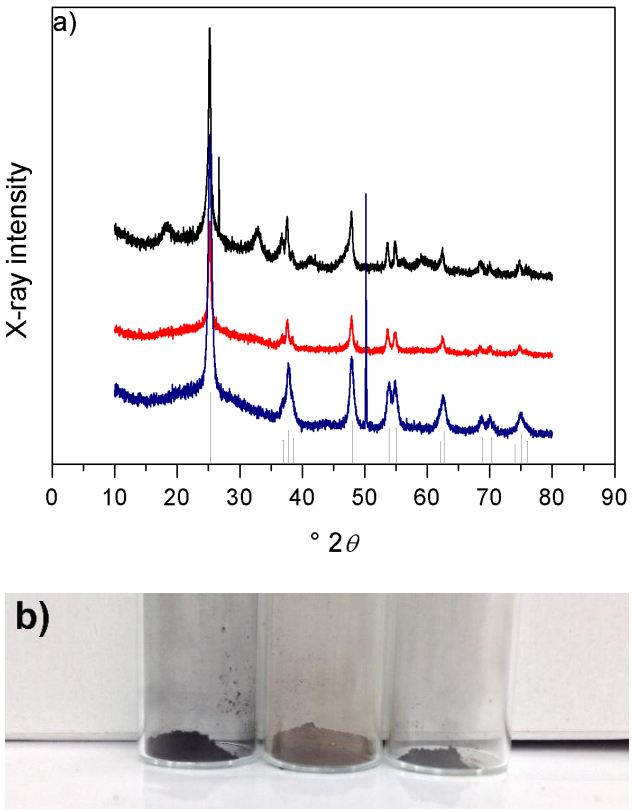

Figure 5.2. a) PXRD patterns for TiNbON-5 prepared at different *R*. b) Photographs of TiNbON prepared at different *R*. Left, *R* = 0.7 (black); middle, *R* = 0.5 (brown); right, *R* = 0.3 (grey).

For *R* = 0.7, a black product is observed, suggesting overincorporation of nitrogen to produce a highly reduced product; this observation is expected to hold for higher *R* until ammonia availability increases high enough that the product shifts from anatase oxynitride to rocksalt nitride. For *R* = 0.3, a grey product is observed, suggesting that nitrogen is not strongly incorporated into the structure due to low ammonia availability; again, this observation should be consistent for lower *R* until only oxide is observed. *R* = 0.5 appears to have accessed an intermediate region in which a brown product is isolated. For the remainder of this study, we focus on the $Ti_{0.95}Nb_{0.05}ON$ material prepared with *R* = 0.5.

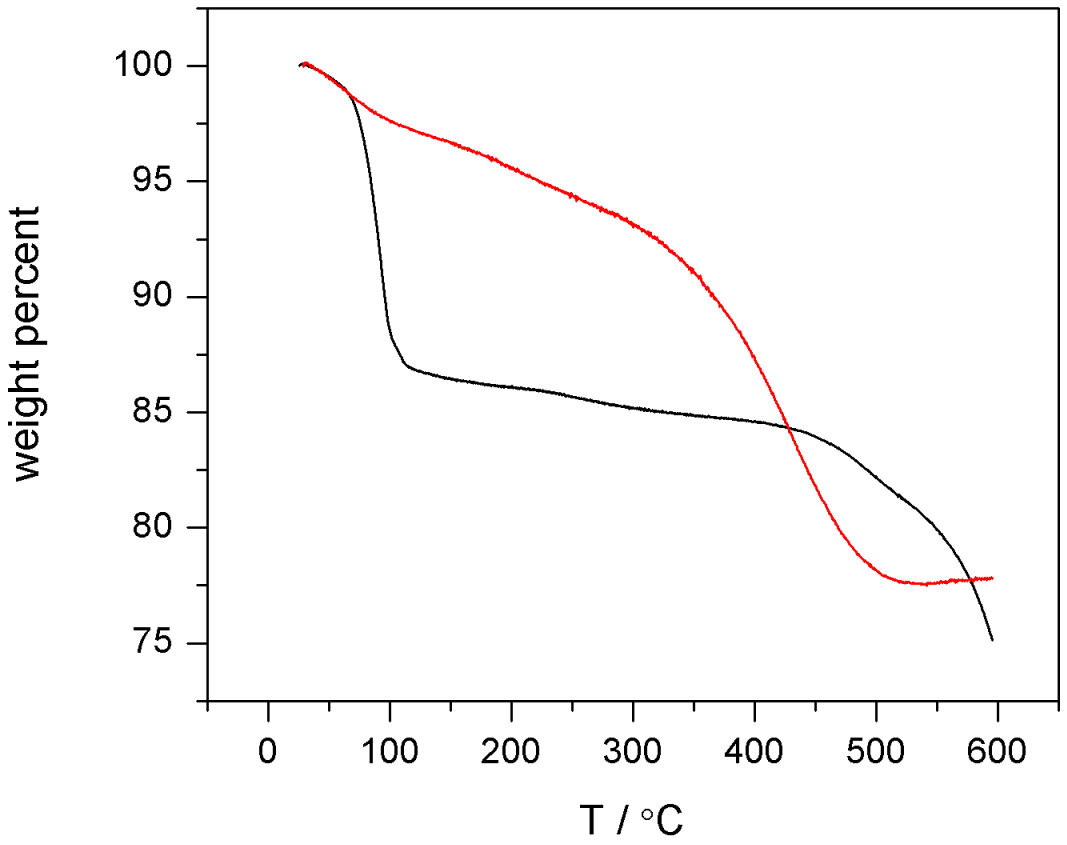

Figure 5.3. Thermogravimetric analysis trace for TiNbON before acid washing (black) and after (red). Analysis was carried out in flowing air.

To assess potential carbon by-products adsorbed to the sample and also its thermal stability, thermogravimetric analysis (TGA) was carried out in flowing air (Figure 5.3). The black trace in Figure 5.3 shows the behavior of the material before washing in acid. A sharp mass loss is observed at 100 °C corresponding to water loss from the $CaCl_2$•$2H_2O$ by-product, followed by a gradual mass loss throughout the remainder of the trace. The red trace, TiNbON after acid wash, shows only a gradual mass loss until ~400 °C, suggesting complete removal of $CaCl_2$•$2H_2O$. A mass loss suggests oxidative loss of nitride from the intersites of the anatase TiNbON,[5] and/or combustion of carbonaceous by-products from the material surface. In order to examine the effects of the mass loss, the material was heated at 400 °C in air for 3 h and analyzed by diffuse reflectance UV-Vis in addition to its use in methylene blue photodegradation.

A scanning electron micrograph of TiNbON-5 after the annealing treatment is presented in Figure 5.4. The micrograph shows a mixture of smaller submicron particles and larger ~5 micron

pieces. This average particle size is significantly decreased from that observed from the unmodified urea-glass synthesis presented in Chapter 4.

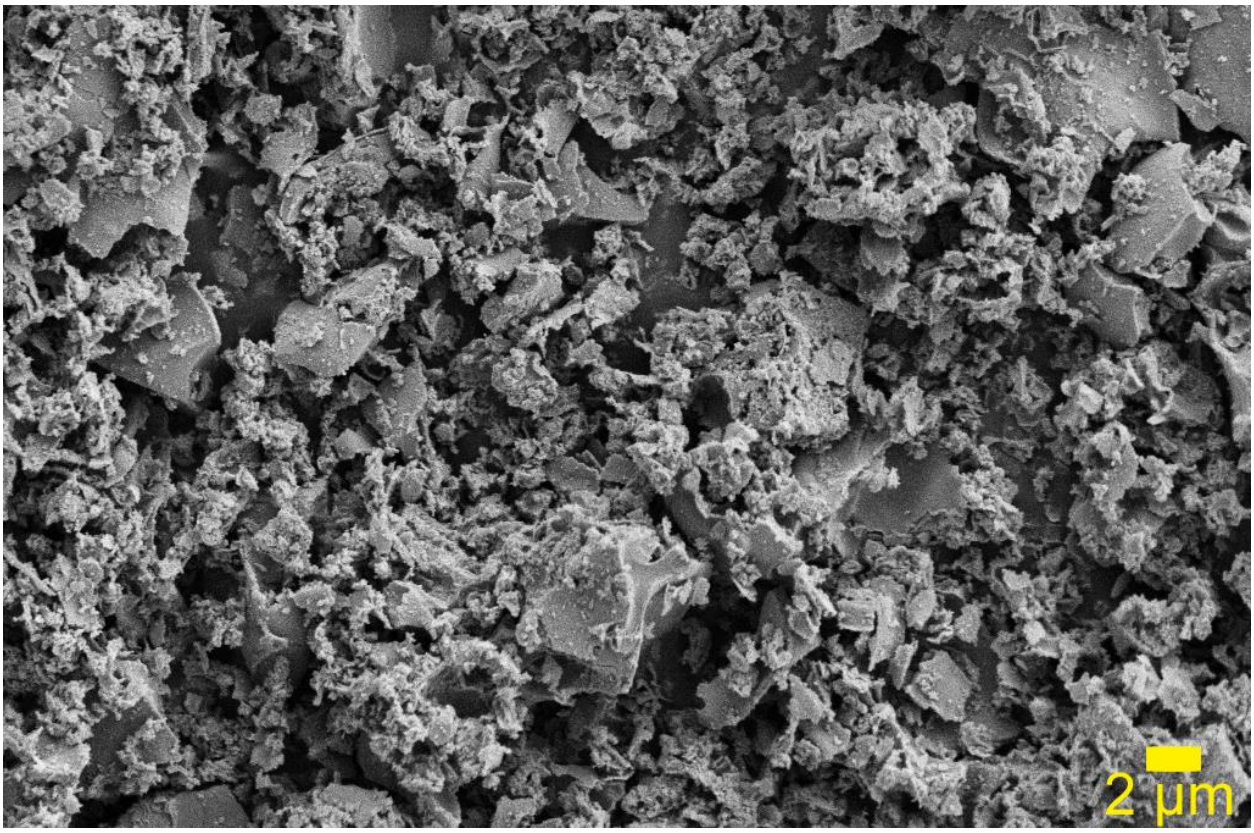

Figure 5.4. Scanning electron micrograph of TiNbON-5 prepared by Ca^{2+}-assisted urea-glass method after annealing at 400 ºC for 3 h.

5.6 Optical and Photochemical Properties

Diffuse reflectance UV-Vis spectra of TiNbON before and after the annealing treatment can be found in Figure 5.5. The material before annealing does not display a well-defined absorption edge. After annealing, a defined absorption edge near 600 nm emerges and the material changes color from dark brown to bright orange.

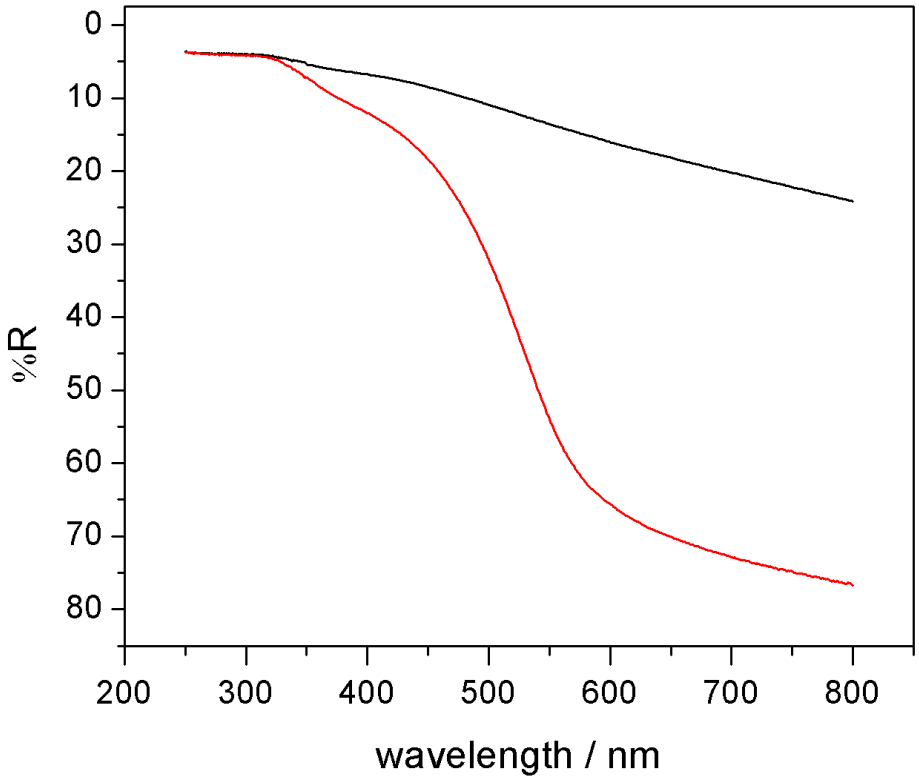

Figure 5.5. Diffuse reflectance UV-Vis spectrum of TiNbON after acid wash before annealing (black) and after annealing (red).

Whether an observed transition is indirect (requiring absorption of a photon and phonon simultaneously; lower absorptivity) or direct (photon absorption only; higher absorptivity) can be surmised from Tauc plots.[6] By multiplying the Kubelka-Munk function times the photon energy and taking the result to some power *n*, a Tauc plot for an indirect ($n = 2$) or direct ($n = 1/2$) transition is achieved. The Tauc plots for TiNbON for indirect and direct transitions can be found in Figures 5.6a and 5.6b, respectively. The indirect plot shows an absorption edge near 3.4 eV, consistent with other optical spectra of anatase TiO_2. However, no transitions whatsoever appear in the Tauc plot at lower energies. By contrast, the direct Tauc plot displays two linear absorption regions at 2.0 and 3.2 eV. This result suggests that transitions between N^{3-} and conduction band states occur with high probability, which should translate into increased photochemical reactivity over this TiNbON compound.

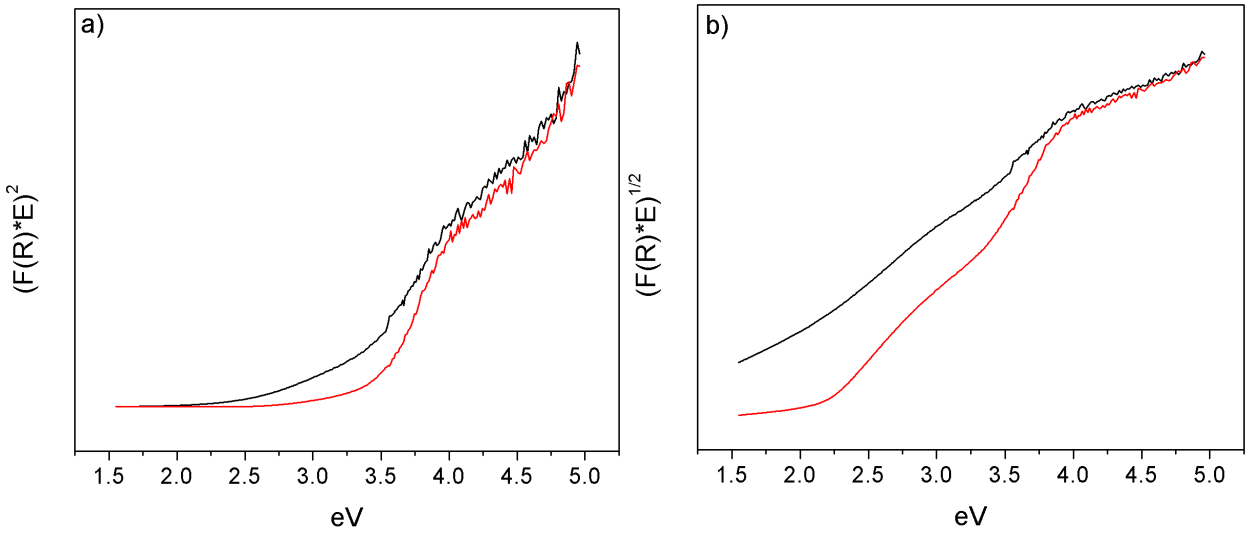

Figure 5.6. Tauc plots for TiNbON before (black) and after (red) the annealing step. Part a) is the plot for indirect band gap, and part b) for direct.

To ensure that the observed optical properties are intrinsic to the material and not an artifact of reflectance sample preparation, absorption spectra were also acquired in transmission mode by grinding TiNbON with KBr and pressing into a transparent pellet. The Tauc plots produced by this measurement are displayed in Figure 5.7. The black lines are a P25 TiO2 reference sample, and the red lines are TiNbON after acid washing and annealing. Both direct and indirect transitions are exhibited for TiNbON, though the direct transition appears at a lower energy. The large spikes in the data are caused by detector saturation at high absorptivities.

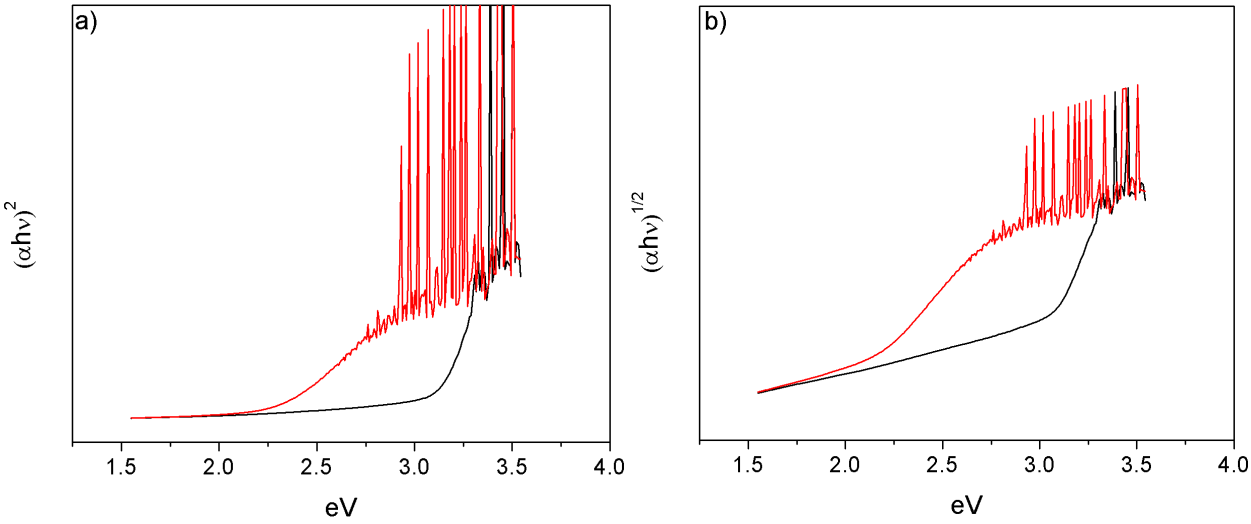

Figure 5.7. Tauc plots for P25 TiO_2 (black) and TiNbON (red) acquired in transmission mode. Part a) is the plot for indirect band gap, and part b) for direct.

To measure the photochemical reactivity of TiNbON prepared by this method, and also to evaluate the importance of the annealing treatment, we conducted methylene blue (MB) photodegradation measurements in a 2 ppm solution. Figure 5.8 shows the Langmuir-Hinshelwood kinetics plot used to calculate the first-order rate constant for MB degradation. The rate constant is equal to the slope of the line through the concentration data; the rate constants are shown in Table 5.1. After annealing, the rate constant for MB degradation over TiNbON increases almost tenfold; additionally, q_{rel}, the amount of MB adsorbed to the material surface during the dark period, increases by a factor of ~4. This result is suggestive that inactive carbonaceous material is being removed from the TiNbON surface during the low-temperature annealing step.

Table 5.1. First-order Langmuir-Hinshelwood rate constants (k_{LH}) for methylene blue degradation and dye sorption measurements (q_{rel}) over TiNbON prepared by Ca^{2+}-assisted urea-glass synthesis before and after an additional annealing step.

	k_{LH} (h^{-1})	q_{rel} (mg MB/g TiNbON)
Acid-wash only	1.785 ± 0.026	27.1 ± 3.9
Acid-washed and annealed	0.181 ± 0.004	6.7 ± 0.7

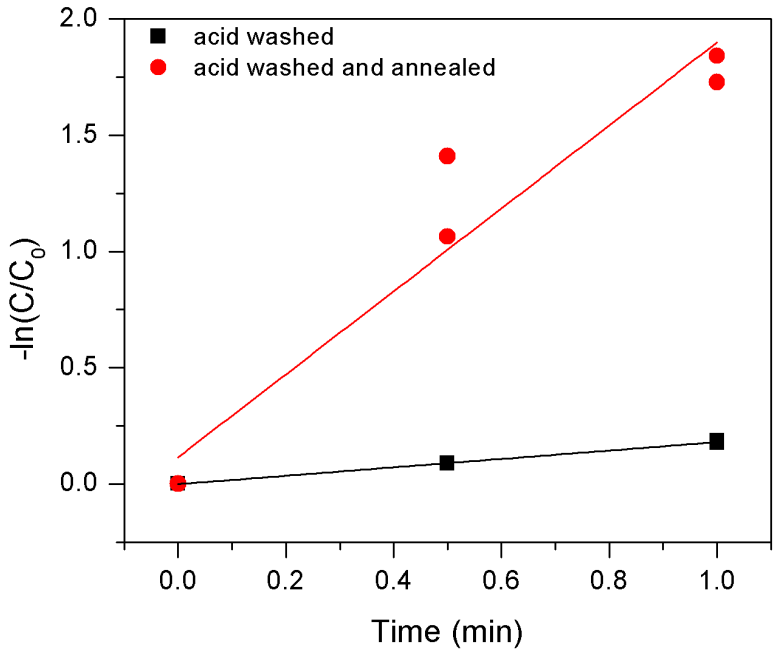

Figure 5.8. Kinetics plot showing raw concentration data over time for methylene blue degradation experiments. Black squares: before annealing, red circles: after annealing. The rate constant is equal to the slope of the line of best fit through the points.

5.7 Conclusions and Outlook

TiNbON prepared by the Ca^{2+}-assisted urea-glass method displays superior visible light absorption and photochemical reactivity to materials prepared without Ca^{2+} presented in Chapter 4. We hypothesize that this increase is due to superior nitrogen incorporation due to slower ammonia release during the synthesis step. Decreased particle size likely also contributes to the increased reaction rate. Further investigation into this intriguing material must involve an analysis of the exact function of the annealing step along with a quantification of nitrogen content compared to previously reported material; this experimental work is ongoing.

5.8 References

(1) Gao, Q.; Giordano, C.; Antonietti, M. Controlled Synthesis of Tantalum Oxynitride and Nitride Nanoparticles. *Small* **2011**, *7* (23), 3334–3340 DOI: 10.1002/smll.201101207.

(2) Giordano, C.; Erpen, C.; Yao, W.; Milke, B.; Antonietti, M. Metal Nitride and Metal Carbide Nanoparticles by a Soft Urea Pathway. *Chem. Mater.* **2009**, *21* (21), 5136–5144 DOI: 10.1021/cm9018953.

(3) Mei, B.; Sánchez, M. D.; Reinecke, T.; Kaluza, S.; Xia, W.; Muhler, M. The Synthesis of Nb-Doped TiO2 Nanoparticles by Spray Drying: An Efficient and Scalable Method. *J. Mater. Chem.* **2011**, *21* (32), 11781 DOI: 10.1039/c1jm11431j.

(4) Arbiol, J.; Cerdà, J.; Dezanneau, G.; Cirera, A.; Peiró, F.; Cornet, A.; Morante, J. R. Effects of Nb Doping on the TiO2 Anatase-to-Rutile Phase Transition. *J. Appl. Phys.* **2002**, *92* (2), 853–861 DOI: 10.1063/1.1487915.

(5) Breault, T. M.; Bartlett, B. M. Composition Dependence of TiO 2 :(Nb,N)- X Compounds on the Rate of Photocatalytic Methylene Blue Dye Degradation. *J. Phys. Chem. C* **2013**, *117* (17), 8611–8618 DOI: 10.1021/jp312199t.

(6) López, R.; Gómez, R. Band-Gap Energy Estimation from Diffuse Reflectance Measurements on Sol–gel and Commercial TiO2: A Comparative Study. *J. Sol-Gel Sci. Technol.* **2012**, *61* (1), 1–7 DOI: 10.1007/s10971-011-2582-9.

Chapter 6

$Cu_{1-x}Ni_xWO_4/WO_3$ Heterojunction Photoanodes Towards Solar Water Oxidation with Improved Faradaic Efficiency

6.1 Introduction

Photoelectrochemical (PEC) water splitting has shown promise as a fuel-generating scheme in which both solar energy and electrical energy are applied, in conjunction with a catalyst, to produce a reduced fuel (such as hydrogen) and oxygen has from liquid water.[1–3] In all such schemes, the four-electron oxidation of water has been identified as the rate-determining step. As such, the development of robust photoanodes for PEC water oxidation is an active and important area of research.

There are several design criteria that must be met in developing a photoanode material in order to maximize the solar-to-fuel-conversion efficiency. A single-phase material must 1) absorb visible light to utilize the most abundant portions of the solar spectrum; 2) exhibit high hole (h^+) conductivity such that photogenerated charges can be driven to the material surface by internal (such as in n-type semiconductors) and/or external electric fields; 3) use those h^+ chemoselectively to drive the oxidation of water at kinetically active surface sites; and 4) maintain this activity for as long as possible. A number of single-phase materials, most importantly TiO_2,[4,5] WO_3,[6,7] Fe_2O_3,[8] TaON,[9,10] and $BiVO_4$,[11] have been studied extensively for PEC water oxidation and demonstrate exceptional performance in one or more of the aforementioned areas. However, no single-phase material has satisfied each criterion simultaneously.

As a result, researchers have turned to multi-phase hybrid materials to impart specialized functionality at the semiconductor-electrolyte interface. A number of powder photocatalysts have

exhibited improved oxidation activity after the addition of oxide co-catalysts such as RuO_2,[12–14] IrO_2,[15] and, more recently, a variety of more earth-abundant metals.[16,17] These co-catalysts generally act by rapidly removing holes from the valence band of the light absorber across the semiconductor-oxide junction, where they are used to oxidize substrates on the co-catalyst surface particle where reaction kinetics are improved (e. g., by suppressing back reactions).[18–21] Another strategy is to synthesize multi-phase bulk heterojunction (BHJ) photoanodes. Heterostructured electrodes are attractive because they allow for improved charge separation, as photogenerated charges can be conducted away from one another by electric fields induced at semiconductor-semiconductor junctions. The introduction of heterostructures has increased photocurrent output and external quantum efficiency in a number of systems, including $CaFe_2O_4$/TaON,[22] $ZnWO_4/WO_3$,[23] Al_2O_3/WO_3,[24] $BiVO_4/CuWO_4$,[25] and several others.[26–29]

Copper tungstate, $CuWO_4$, has drawn recent interest as a single-phase photoanode material.[30–34] $CuWO_4$ improves WO_3 in terms of visible light absorption and photoelectrochemical stability.[35] A known degradation pathway in WO_3 during PEC water oxidation is the formation of high-energy peroxides and hydroxyl radicals, which can react chemically with the electrode material and dissolve it.[36] Additionally, the high oxidative potential of valence band holes in WO_3 facilitates side reactions with a variety of electrolyte anions, resulting in poor overall Faradaic efficiency for the OER.[37,38] As the valence band of $CuWO_4$ is ~500 mV less oxidizing (reports of the energy of the valence band vary significantly) due to the occupied Cu(3d) states that form the top of the valence band, this decay pathway is mitigated.[29, 32, 39] As a result $CuWO_4$ electrodes have shown excellent stability and near unit Faradaic efficiency in potassium borate electrolytes at pH 7.[35]

We present herein the synthesis of composite photoanodes consisting of a WO_3 absorber layer functionalized by a $CuWO_4$ interface layer. We hypothesize that the addition of a $CuWO_4$ overlayer will address the poor Faradaic efficiency of WO_3 by funneling holes through the less-oxidizing $CuWO_4$ valence band. The heterostructures are fabricated using low-cost synthetic methods. Furthermore, we modulate the electronic structure of the $CuWO_4$ interfacial layer by doping Ni^{2+} onto Cu^{2+} sites and examine the effects on charge transfer through the heterostructures. In each case, the heterostructured anode exhibits improved Faradaic efficiency and overall OER rate compared to a stand-alone WO_3 electrode. Finally, we examine the origin of this increase in chemical selectivity by employing an organic radical trap, α-thujone, to probe the activity of

hydroxyl radical intermediates at the surface of each electrode.[40,41]

6.2 Experimental Procedures

Ethanol, methanol, and methylene chloride were ACS reagent grade and purchased from Fisher Scientific. The remainder of the chemicals employed in this study were purchased from the following manufacturers at the denoted levels of purity and used without further purification: copper nitrate trihydrate, 99.9%, Fisher Scientific; copper acetate dihydrate, 98%, Sigma-Aldrich; nickel acetate dihydrate, 98%, Sigma Aldrich; nickel nitrate hexahydrate, 99.9%, Fisher Scientific; sodium tungstate dihydrate, 99%, Acros Organics; ammonium metatungstate, 99%, Sigma-Aldrich; (-)-α-thujone, 96%, Sigma-Aldrich; boric acid, 99.5%, Sigma-Aldrich; hydrogen peroxide 30% solution, Sigma-Aldrich; formic acid, 95%, Sigma-Aldrich; dodecane, 99.9%, Sigma-Aldrich; carvacrol, 98%, Sigma-Aldrich; hydrochloric acid 12.1 M concentrated solution, Fisher Scientific; polyethylene glycol 300, TCI. Potassium hydroxide (85% purum) was purchased from Sigma-Aldrich and purified according to the procedure of Trotochaud et al.[42] before use. Photoanodes were fabricated on glass substrates coated with a ~400 nm-thick layer of fluorinated tin oxide (FTO, Pilkington Glass, 12-14 Ω). The FTO substrates were cleaned by successive sonication for 15 minutes in acetone, ethanol, and 18.2 Ω Millipore purified water before drying in a stream of nitrogen.

Synthesis of $Cu_{1-x}Ni_xWO_4$ ($0 < x < 0.3$) electrodes by spray pyrolysis. $Cu_{1-x}Ni_xWO_4$ (x = 0-0.3) films were deposited onto FTO substrates using a custom-built spray pyrolysis apparatus. The spray parameters employed were adapted from a spray deposition for $CuWO_4$ previously reported by Gaillard et al.[33] Figure C1 depicts the apparatus used. Aqueous stock solutions of 100 mM copper acetate dihydrate and nickel acetate dihydrate were prepared, along with a stock solution of 8.3 mM ammonium metatungstate (chemical formula $(NH_4)_6H_2W_{12}O_{40}$, 100 mM in $[W^{6+}]$). The stock solutions were combined stoichiometrically and diluted with Millipore water to a final volume of 10 mL such that $[Cu^{2+}] + [Ni^{2+}] = 10$ mM and $[W^{6+}] = 10$ mM. The precursor solution was then sprayed through a glass nozzle onto the heated FTO substrate. The spray pyrolysis parameters employed were as follows: the substrate temperature was 275 °C, the nozzle height was 10 inches, the carrier gas was N_2 at a pressure of 12.5 psi, and the solution was sprayed 20 times for a 1 s interval with a 10 s waiting period every 10 sprays to ensure that the substrate temperature remained nearly constant.

Synthesis of MWO_4/WO_3 (M = Cu, $Cu_{0.95}Ni_{0.05}$) bulk heterojunction electrodes. Metal

tungstate/tungsten oxide (MWO_4/WO_3) bulk heterojunction photoanodes (BHJs) were synthesized in two steps by a solid-state reaction atop prefabricated WO_3 electrode. The synthesis of WO_3 electrodes was adapted from a known sol-gel procedure.[36] Briefly, a colloidal suspension of H_2WO_4 was prepared in 50/50 v/v ethanol/water solution by passing sodium tungstate dihydrate through a Dowex ion exchange column. The suspension was then concentrated by rotary evaporation and polyethylene glycol 300 was added as a stabilizing agent. 25 μL of the suspension was applied to a masked 1 cm^2 area of the FTO and spun on a Laurell Technologies model WS-400B-6NPP/LITE spin coater at 2500 rpm for 30 s. The films were then placed in a preheated oven at 500 °C for 30 min in air. This process was repeated 10 times, resulting in glassy yellow monoclinic WO_3 electrodes ~2 μm in thickness with excellent mechanical adhesion. The metal tungstate overlayer was applied via a known literature procedure.[38] Aqueous solutions of 100 mM $M(NO_3)_2$ were prepared, and 50 μL of solution was applied to a 1 cm^2 WO_3 electrode. The electrodes were immediately annealed at 550 °C for 6 h in air with a heating and cooling rate of 1.5 °C/min. Excess metal oxides that formed on the film were dissolved off from the electrode by soaking in 0.5 M HCl for 30 min.

Electrode characterization. Electrodes were analyzed by powder x-ray diffraction (PXRD), scanning electron microscopy (SEM), energy dispersive X-ray spectroscopy (EDX), and UV-VIS diffuse reflectance spectroscopy. PXRD measurements were taken on a Bruker D8 Advance diffractometer with graphite monochromator and Lynx-Eye detector using Cu Kα radiation. SEM images and EDS measurements were performed on an FEI Quanta 3D scanning electron microscope using beam voltage of 16.5 kV and current of 2.3 nA for heterostructure films (15 kV and 2.2 nA for WO_3). UV-VIS measurements were performed on a Cary 5000 UV-VIS-NIR spectrophotometer using an internal diffuse reflectance accessory (Varian) for measurements on thin films. Band gaps were calculated via standard absorption edge extrapolation on Tauc plots constructed using the Kubelka-Munk function for indirect band gap semiconductors.

Electrochemical measurements and photoelectrochemical oxidations. For all photoelectrochemical experiments, a Newport-Oriel 150 W Xe lamp was utilized. The lamp was used in conjunction with an AM 1.5G filter and fiber-optic cable to reduce the irradiance at the film to 100 mW/cm^2.

Linear sweep voltammetry were performed in a single-compartment 3-electrode Pyrex cell fitted with a quartz viewing window using a Chemical Instruments 1000A potentiostat. A saturated

calomel electrode (SCE) was employed as the reference electrode and a Pt disk was used as the counter electrode. A 20 mV/s scan rate was employed. The electrolyte used, denoted as KB_i, was 0.1 M boric acid adjusted to pH 7 with purified potassium hydroxide solution, with or without 0.2 M hydrogen peroxide, 0.2 M methanol, or 0.2 M formic acid.

Photoelectrochemical oxygen evolution was performed in a two-compartment Pyrex bulk electrolysis cell fitted with a quartz viewing window on each compartment. The compartments were separated by a sintered glass frit. Both compartments were charged with 20 mL of KB_i and sparged for 1 h with N_2 before sealing under an N_2 atmosphere with an SCE reference electrode and Pt wire counter electrode. A NeoFox FOSSPOR fluorescence lifetime oxygen detection probe was sealed in the working electrode compartment headspace, and an accompanying temperature probe was sealed in the counter electrode headspace. The oxygen probe was calibrated in ambient air (20.9%) and in N_2 gas (0%) before addition to the cell, and was allowed to equilibrate for at least 30 min before the experiment began. Photoelectrolysis was carried out at 1.23 V vs. RHE (0.573 V vs SCE) with a 60 s pre-electrolysis period before the film was illuminated. The moles of oxygen in the cell headspace were calculated by converting partial pressures recorded by the probe using the ideal gas law in conjunction with Henry's Law to account for dissolved O_2 in the electrolyte. The average drift in the probe reading was calculated by measuring the change in the moles of O_2 present while the cell was inactive both before and after the experiment, fitting both segments to a linear function, and subtracting from the final moles of O_2 measured.[37] The maximum moles of O_2 observable (assuming 100% Faradaic efficiency) was calculated by integrating the *j-t* curve for the entire illumination time, then dividing by $-4F$. Actual Faradaic efficiency was calculated by taking the ratio of observed O_2 to the maximum possible O_2 calculated by coulometry.

Hydroxyl radical detection with α-thujone. An all-quartz photoelectrolysis cell with a 6 mL working electrode compartment was used for radical detection experiments. 0.1 M KB_i was prepared with 10 mM α-thujone added. The cell was sealed under ambient conditions with an Ag/AgCl reference electrode and 6 mL of electrolyte in the working electrode compartment, and with 3.5 mL of electrolyte and a Pt wire electrode in the counter electrode compartment. Electrolysis was carried out at 1.23 V vs. RHE with a 60 s pre-electrolysis period before the film was illuminated. Photoelectrolysis was carried out until ~3 C had been passed. The electrolyte was then removed from both compartments and combined. A 3 mL aliquot of the electrolyte was

extracted 3 times with 0.5 mL methylene chloride. A 0.5 mL aliquot of the combined organic layers was diluted with 0.5 mL of a 2 mM solution of dodecane in methylene chloride. The final solution was analyzed on a Shimadzu QP-2010 GCMS equipped with a 30 m DB-5 column (0.25 mm inner diameter). This procedure was performed in triplicate to ensure consistency in the extraction procedure. GCMS data were compared with authentic samples of α-thujone and carvacrol. Product identification was achieved via comparing retention times and mass spectra with a publicly available NIST database. Peak areas were calculated by integration and normalized to the area of the dodecane internal standard.

6.3 Physical Characterization of BHJ Photoanodes

As previously reported by Hill et al., the reaction of aqueous metal nitrates with crystalline tungsten oxide produces a mixed-phase film where the WO_3 substrate has been partially converted to the corresponding MWO_4 phase.[38] The PXRD pattern of the electrodes is dominated by the large signal of the extremely crystalline WO_3 substrates, but reflections attributed $CuWO_4$ are seen in the final reaction products (Figure C2). No copper oxide or nickel oxide impurities remain in the film after the acid soaking procedure.

The optical absorption of the BHJ electrodes was measured using UV-Vis diffuse reflectance spectroscopy. The absorption spectra of the BHJ electrodes were compared to that of pure-phase WO_3, $CuWO_4$, and $Cu_{0.95}Ni_{0.05}WO_4$ electrodes (Figure C3). Comparison of these spectra supports the description of the BHJ electrodes as a phase-segregated mixture, as the absorption spectrum of the BHJ electrodes contains only features also seen in the spectra of the pure-phase materials. BHJ electrodes absorb visible light out to the 550 nm range, with no significant change in band gap observed between Ni^{2+}-doped and pure $CuWO_4$ overlayers.

The thickness and elemental distribution of the electrodes was characterized by SEM coupled with EDX. The samples were analyzed cross-sectionally, as seen in Figure 6.1. The pure WO_3 electrodes are approximately 2 μm in thickness. The treatment with aqueous metal nitrates does not significantly alter the thickness of the electrodes, resulting in BHJ electrodes of the same approximate thickness as the WO_3 starting material. EDX analysis reveals that the copper content of the electrode does not begin to increase above baseline levels until ~800 nm below the film surface. Even at the surface of the film, the Cu:W ratio does not reach 1:1, suggesting that the film composition is not consistent with a purely layered MWO_4/WO_3 heterojunction. Instead, the elemental distribution is more supportive of a morphology of MWO_4/WO_3 composite or core-shell

nanoparticles, in which the M content of the nanoparticles increases from the FTO back contact to the surface of the film.

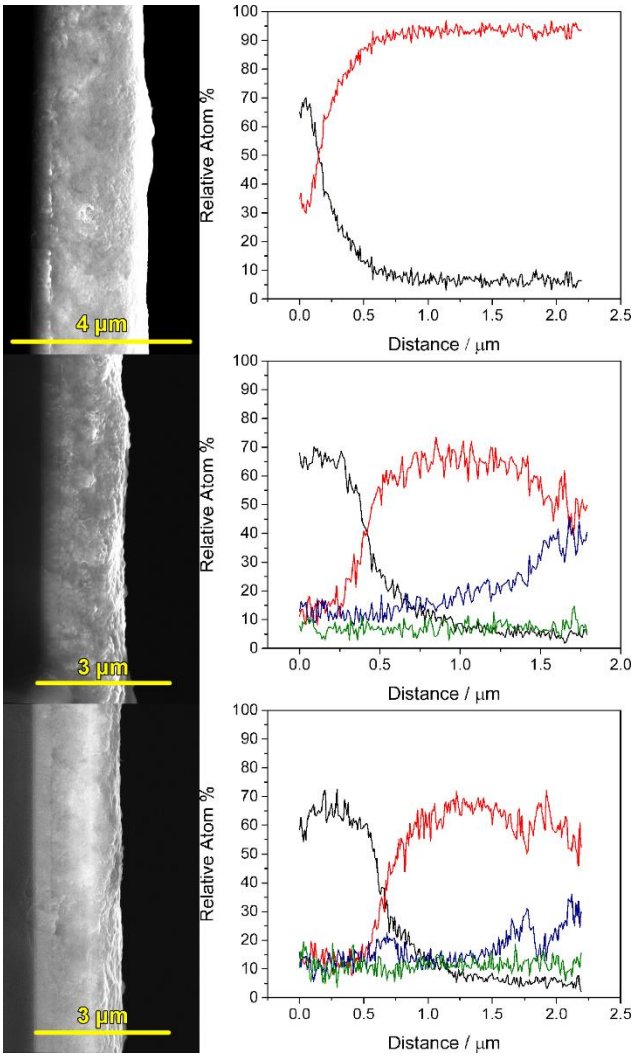

Figure 6.1. Cross-sectional scanning electron microscopy (left) and elemental mapping by energy dispersive x-ray spectroscopy (right) for WO_3 (top), BHJ-Cu (middle) and BHJ-CuNi (bottom) films. Legend: Sn, black; W, red; Cu, blue; Ni, green.

6.4 Photoelectrochemistry and Charge-Transfer Kinetics of BHJ Electrodes

The photoresponse of BHJ photoanodes was measured in 0.1 M KB_i solution by linear sweep voltammetry (Figure 6.2a). All electrodes exhibit increased photoresponse when the substrate-electrode (SE) interface is illuminated compared to the electrode-electrolyte (EE) interface (Figure C4); the data shown in Figure 6.2a-c was taken using SE illumination. Relative to WO_3, the overall photoresponse of BHJ-Cu and BHJ-CuNi photoanodes was diminished. Ni^{2+} substitution in the catalytic overlayer was found to have a positive effect on the photocurrent, as

evidenced by the slightly higher photoresponse observed in BHJ-CuNi films relative to BHJ-Cu (Table 6.1). However, it cannot be concluded from voltammetry in boric acid solution whether the increase in photocurrent is due to improved internal charge transport of photogenerated holes, or whether the Ni^{2+} substitution improves the surface kinetics of the electrode. Nickel sites on the surface hypothetically have access to the $Ni^{2+/4+}$ redox couple, which facilitates multi-electron chemistry that is critical to driving the four-electron oxidation of water.

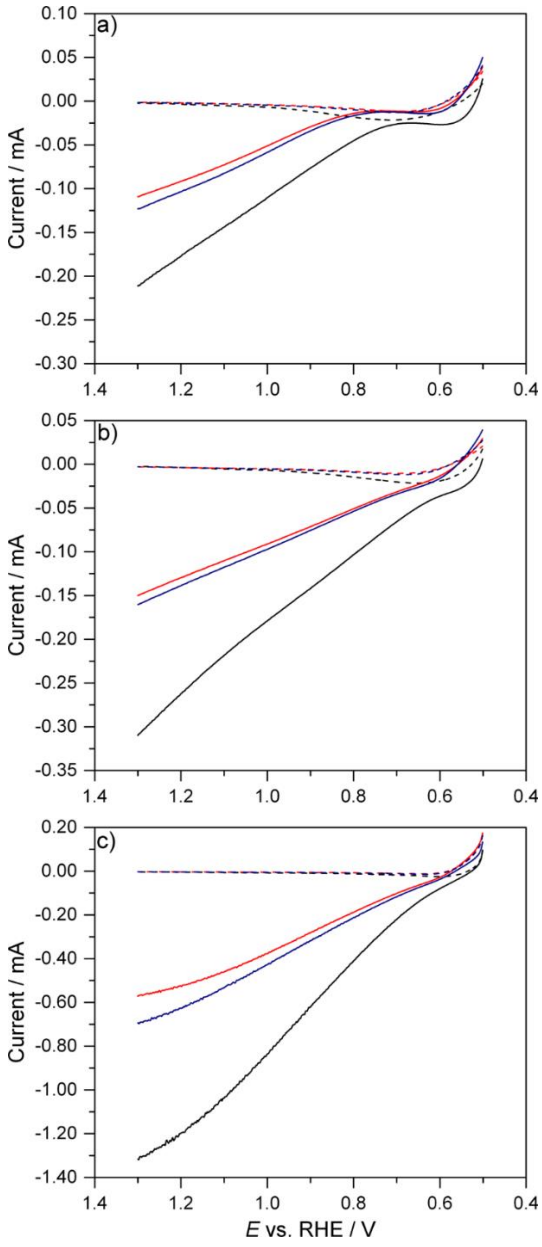

Figure 6.2. Linear sweep voltammograms in 0.1 M KBi with no additives (top), 0.2 M methanol (middle), and 0.2 M formate (bottom) for representative films. Dashed lines represent the current without illumination, and solid lines under illumination. Average values for photocurrent are shown in Table 1. Legend: WO_3, black; BHJ-Cu, red; BHJ-CuNi, blue.

To further understand the origin of the increased performance of BHJ-CuNi electrodes, we conducted linear sweep voltammetry measurements in 0.1 M boric acid solution with 0.2 M methanol added (Figure 2b) and with 0.2 M formic acid added (Figure 2c). Methanol and formic acid are well-known hole scavengers that are frequently used in investigations of charge transfer processes using TiO_2 and WO_3 photoanodes.[43–45] Methanol is oxidized over TiO_2 via an indirect hole transfer mechanism in which the semiconductor first oxidizes a bound water molecule to create a hydroxyl radical (•OH), which then goes on to oxidize methanol.[43, 45] However, the direct hole transfer mechanism was found to prevail over WO_3 films, where methanol is oxidized directly by the valence band.[44] The difference in reactivity was ascribed to the increased Lewis acidity of the W^{6+} surface sites in WO_3 relative to the Ti^{4+} sites in TiO_2, promoting methanol binding to the oxide surface. $CuWO_4$ is anticipated to have a less Lewis acidic surface than WO_3 due to the increased electron density provided by d^9 Cu^{2+} surface sites, and the mechanism of methanol oxidation remains uncertain. Formic acid is a hole scavenger known to act via the direct hole transfer mechanism over both TiO_2[43] and WO_3[44], and we have employed it here to account for either mechanistic possibility.

Table 6.1. Average values of photocurrent response in μA for WO_3 and BHJ electrodes in denoted solutions.

	0.1 M KB_i	0.1 M KB_i + 0.2 M MeOH	0.1 M KB_i + 0.2 M $HCOO^-$
WO_3	164 +/- 34	259 +/- 29	1115 +/- 222
BHJ-Cu	95.6 +/- 2.1	136 +/- 0.85	546 +/- 68
BHJ-CuNi	101 +/- 11.5	145 +/- 3.9	631 +/- 88

We observe large increases in photoresponse for all three electrodes in methanolic solutions. Representative linear sweep voltammograms are shown in Figure 6.2b. Consistent with previous reports on $CuWO_4$,[31] we observe a ~200 mV cathodic shift in the onset potential for photocurrent over MWO_4-modified electrodes; however, no significant difference in onset potential between BHJ-Cu and BHJ-CuNi electrodes could be identified. As shown in Table 1, an increase in average photoresponse for BHJ-CuNi films relative to BHJ-Cu films is again observed. In the presence of a strong electron donor such as methanol, this observation can be ascribed to improved charge transport kinetics in BHJ-CuNi films. However, given previous evidence showing that methanol is oxidized by indirect hole transfer, the influence of surface kinetics in producing •OH cannot be ruled out.

We performed linear sweep voltammetry measurements in pH 7 solutions of boric acid with formic acid added. Given formic acid's pKa of 3.75, the predominating solution species is formate anion. Formate is expected to have far stronger interaction with the Lewis acidic oxide surfaces than methanol, thereby promoting its oxidation by direct hole transfer. Consistent with this hypothesis, we observe a three- to four-fold increase in the photoresponse for each electrode type; representative voltammograms are shown in Figure 6.2c, and average photocurrent values given in Table 6.1. Again, BHJ-CuNi electrodes show significantly higher photocurrent than BHJ-Cu films. These photocurrent data corroborate the findings from Mott-Schottky analysis (Figure 3) of pure-phase $CuWO_4$ and $Cu_{0.95}Ni_{0.05}WO_4$ electrodes. Ni^{2+} substitution slightly raises the flat band potential (E_{fb}) of $CuWO_4$. Given the identical material band gaps, this likely corresponds to a raising of the conduction band energy of $Cu_{0.95}Ni_{0.05}WO_4$ relative to $CuWO_4$. Consequently, electron transfer is facilitated from the conduction band of $Cu_{0.95}Ni_{0.05}WO_4$ to the conduction band of WO_3 and throughout the remainder of the circuit. It is assumed that the corresponding hole transfer is also accelerated.

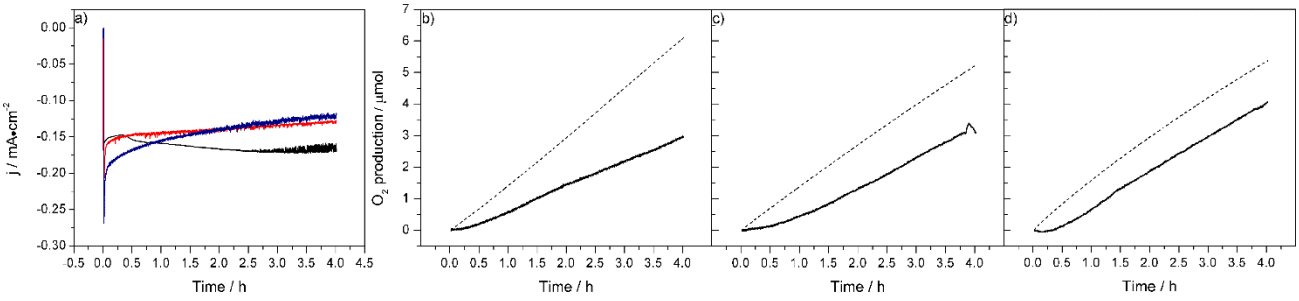

Figure 6.3. Photochemical OER of WO_3 and BHJ films. a) *j-t* curves for WO_3 (black), BHJ-Cu (red), and BHJ-CuNi. b-d) Oxygen evolution versus time for the same 3 electrodes, respectively. Dotted lines represent expected O_2 at 100% Faradaic efficiency; solid lines represent measured O_2.

6.5 Photoelectrochemical Oxygen Evolution

To measure the Faradaic efficiency for oxygen evolution, photoelectrolysis measurements were carried out under nitrogen atmosphere with a fluorescence probe to measure headspace oxygen. The results of these experiments are shown in Figure 6.3. The bulk electrolysis profiles (Figure 6.3a) display similar initial activity. WO_3 electrodes exhibit a gradual increase in photocurrent that peaks before decreasing at longer timescales. The increase in photocurrent is attributed to electrode roughening due to degradation, and the eventual decrease in photocurrent to the subsequent dissolution of electrode material into the electrolyte. Both BHJ electrodes exhibit a steady decrease in activity over the 3 h experimental timescale, implying that the catalytic

overlayer is not entirely stable. The oxygen evolution for each film is shown in Figures 4b-d. The Faradaic efficiency (η) for oxygen evolution was measured to be 50% over WO_3 electrodes, compared with 59% and 76% over BHJ-Cu and BHJ-CuNi, respectively, with a standard error of 15% across each sample. Taken in conjunction with the observation of improved electron transfer described above, we hypothesize that the trends in η observed in our oxygen evolution experiments are brought about by a difference in locality of oxygen evolution on a complex BHJ surface. It has been observed previously that $CuWO_4$ electrodes display excellent η for OER in the KB_i electrolyte.[35] In the example of BHJ-Cu, the comparatively poor electron transfer increases the overall resistance for hole transfer from photoexcited WO_3 to $CuWO_4$ and ultimately into solution. As a result, the lower-resistance pathway is for water to be oxidized over BHJ-Cu at exposed WO_3 sites, the quantity of which has been reduced by the $CuWO_4$ overlayer treatment. This hypothesis accounts both for the decreased photocurrent and for the marginal increase in η relative to WO_3. In the case of BHJ-CuNi, the improved electron transfer allows for facilitated hole transfer from WO_3 through $Cu_{0.95}Ni_{0.05}WO_4$ and into solution. We infer that a greater number of OER turnovers occurs on selective $Cu_{0.95}Ni_{0.05}WO_4$ sites compared to WO_3 sites, resulting in the observed increase in η for the reaction.

6.6 Hydroxyl Radical Trapping Using α-Thujone

To further investigate the increase in OER selectivity, we sought to measure the relative production of •OH by each of the electrodes employed in this study, we carried out controlled potential photoelectrolysis at 1.23 V vs. RHE in the presence of α-thujone. α-thujone has been employed previously to carry out mechanistic investigations into the activity and rate constants involved in oxidations by cytochrome P450.[40] Due to the high anodic potentials employed in our photoelectrochemical OER experiments, we sought an organic probe molecule that could be transformed to easily-discernable products based on the mechanism of oxidation employed. α-thujone is ideal for this purpose. As described in references 40 and 41, α-thujone reacts with radicals via rapid cyclopropane ring opening, followed by formation of either an alkene or alcohol moiety. Conversely, when non-radical oxidants are used, the oxidation proceeds through a carbocationic intermediate. Rapid aromatization follows, resulting in carvacrol as the product (see Scheme 1). By quantifying the yield of relevant alkene (**1** and **2**) and alcohol products seen previously in reference 41, and also by quantifying carvacrol (**3**), we gain insight into the surface chemistry occurring over each of our electrode types.

Table 6.2. GCMS yields of a-thujone oxidation products using the denoted working electrodes expressed as a percentage of total detected products. *: Total radically-oxidized products per coulomb, normalized to ROP/C detected using WO_3.

	1	**2**	**4**	**5**	Total ROP	**3**	ROP/C*
WO_3	12.9%	14.6%	33.9%	17.3%	78.7%	21.3%	1
BHJ-Cu	0	3.7%	65.0%	11.3%	80.1%	19.9%	0.75
BHJ-CuNi	0	0	51.8%	18.6%	70.5%	29.5%	0.47
$CuWO_4$	0	0	58.5%	41.5%	100%	0%	0.087

The calculated yields, expressed as a percentage of total detected products, are given in Table 2. Ring-opening products **1** and **2**, along with hydroxylated thujones **4** and **5**, are consistent with commonly observed reactions of radical clock substrates with hydroxyl radicals. Carvacrol (**3**) is also observed for oxidations using all three electrodes. A decrease in the total fraction of radical oxidation products (**1**, **2**, **4**, and **5**; radically-oxidized products (ROP)) is observed progressing from WO_3 to BHJ-Cu to BHJ-CuNi. Similar amounts of **3** are detected over WO_3 and BHJ-Cu, with a ~10% increase in total product fraction of **3** detected over BHJ-CuNi. Surprisingly, a control experiment carried out with a pure phase $CuWO_4$ working electrode resulted exclusively in the detection of radically oxidized products **4** and **5**, though the yield of these products on a per coulomb basis was drastically decreased.

The final column of Table 6.2 lists the total yield per coulomb of all ROPs in each assay divided by the yield of ROPs per coulomb using a WO_3 working electrode. This quantity allows for the examination of total radical product conversion between assays as opposed to relative yields within the same assay. The total yield per coulomb of ROPs decreases from WO_3 to BHJ-Cu to BHJ-CuNi. Notably, the yield of these products over $CuWO_4$ is less than 10% of that observed for the WO_3 electrode. Assuming that the efficiency of •OH trapping by α-thujone is primarily dependent upon •OH concentration near the electrode surface, the decreased trapping efficiency per coulomb is indicative of a decrease in overall •OH production.

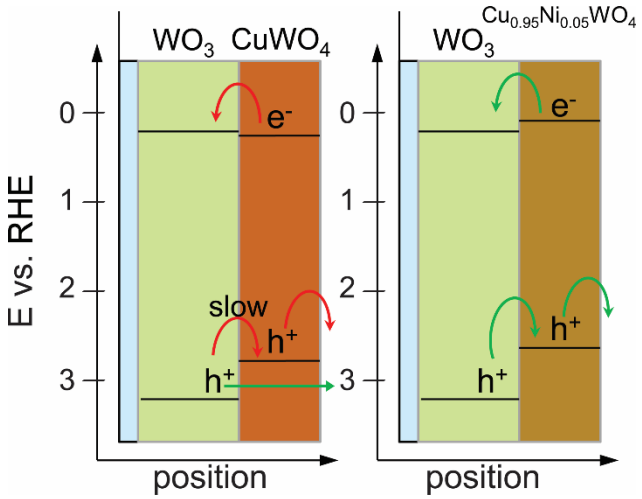

Figure 6.4. Schematic depicting favorable and unfavorable charge transport pathways during photochemical OER using BHJ-Cu (left) and BHJ-CuNi (right) photoanodes.

These observations are consistent with what would be expected given the thermodynamic positions of the $H_2O/^{\cdot}OH$ redox couple ($E°$ = 2.9 V vs. RHE) and the positions of the valence bands of $CuWO_4$ and WO_3. The experimentally-determined positions of these energy levels are shown in Figure 6.4. Under illumination, high-energy holes in the O(2p) valence band of WO_3 can rapidly oxidize adsorbed water molecules to form •OH via a thermodynamically favorable process. By contrast, the $CuWO_4$ valence band maximum is dominated by less oxidative Cu(3d) states. Photogenerated holes at the valence band maximum of $Cu_{0.95}Ni_{0.05}WO_4$ cannot access the $H_2O/^{\cdot}OH$ redox couple without added potential energy. As a result, pure-phase $CuWO_4$ (and by extension $Cu_{0.95}Ni_{0.05}WO_4$) oxidize water by lower-energy, non-radical pathways.

The energetic restrictions on oxidative chemistry are present in the heterojunction electrodes, but now charge transfer of electrons from semiconductor to semiconductor becomes an important consideration as well. In BHJ-Cu, the $CuWO_4$ conduction band is slightly more positive than the WO_3 conduction band, resulting in a Type I heterojunction in which electron transfer from conduction band to conduction band experiences a thermodynamic barrier. In BHJ-CuNi, however, the conduction band has been slightly raised by Ni^{2+} substitution, so the electron transfer from $Cu_{0.95}Ni_{0.05}WO_4$ to WO_3 and onwards throughout the circuit is facilitated. As discussed above, sluggish electron transfer in BHJ-Cu allows for holes in photoexcited WO_3 to take a less-resistive pathway into solution by oxidizing water at exposed WO_3 surface sites, producing •OH as an intermediate which reacts with α-thujone. By contrast, in BHJ-CuNi electrodes, photoexcited electrons are more easily transferred from $Cu_{0.95}Ni_{0.05}WO_4$ to WO_3. A higher fraction of hole

current can then proceed from the valence band of WO_3 to that of $Cu_{0.95}Ni_{0.05}WO_4$ where water is oxidized via a non-radical mechanism.

6.7 Conclusions

We have prepared heterostructured MWO_4/WO_3 photoanodes via a simple treatment of sol-gel WO_3 substrates with aqueous precursors. In pure-phase electrodes synthesized by spray pyrolysis, we observe a slight raising of the conduction band of $CuWO_4$ after 5% substitutional doping with Ni^{2+}. The effects of the raised conduction on internal charge transport in bulk heterjunction electrodes are observed via photoelectrochemistry in the presence of methanol and formate hole scavengers, with $Cu_{0.95}Ni_{0.05}WO_4/WO_3$ electrodes passing significantly higher photocurrent than $CuWO_4/WO_3$. On the basis of hydroxyl radical scavenging experiments carried out with α-thujone, we ascribe the increase in selectivity to a decrease in the fraction of •OH produced at the electrode surface. This suggests that, with the improved charge transport across the MWO_4/WO_3 junction in BHJ-CuNi electrodes, a higher percentage of holes are funneled through the comparatively less oxidizing MWO_4 valence band where 1 e^- chemistry that would result in the formation of •OH is inaccessible thermodynamically.

6.8 References

(1) Walter, M. G.; Warren, E. L.; McKone, J. R.; Boettcher, S. W.; Mi, Q.; Santori, E. A.; Lewis, N. S. *Chem. Rev.* **2010**, *110*, 6446–6473.
(2) Kudo, A.; Miseki, Y. *Chem. Soc. Rev.* **2009**, *38*, 253–278.
(3) Batzill, M. *Energy Environ. Sci.* **2011**, *4*, 3275.
(4) Fujishima, A. *Nature* **1972**, *238*, 37–38.
(5) Fujishima, a; Zhang, X.; Tryk, D. *Int. J. Hydrogen Energy* **2007**, *32*, 2664–2672.
(6) Butler, M. a. *J. Appl. Phys.* **1977**, *48*, 1914.
(7) Bignozzi, C. A.; Caramori, S.; Cristino, V.; Argazzi, R.; Meda, L.; Tacca, A. *Chem. Soc. Rev.* **2013**, *42*, 2228–2246.
(8) Bora, D. K.; Braun, A.; Constable, E. C. *Energy Environ. Sci.* **2013**, *6*, 407.
(9) Maeda, K.; Lu, D.; Domen, K. *Chemistry* **2013**, *19*, 4986–4991.
(10) Hitoki, G.; Takata, T.; Kondo, J. N.; Hara, M.; Kobayashi, H.; Domen, K. *Chem. Commun. (Camb).* **2002**, *2*, 1698–1699.
(11) Kudo, A.; Omori, K.; Kato, H. *J. Am. Chem. Soc.* **1999**, *121*, 11459–11467.
(12) Teramura, K.; Maeda, K.; Saito, T.; Takata, T.; Saito, N.; Inoue, Y.; Domen, K. *J. Phys. Chem. B* **2005**, *109*, 21915–21921.
(13) Sato, J.; Saito, N.; Yamada, Y.; Maeda, K.; Takata, T.; Kondo, J. N.; Hara, M.; Kobayashi, H.; Domen, K.; Inoue, Y. *J. Am. Chem. Soc.* **2005**, *127*, 4150–4151.
(14) Breault, T. M.; Brancho, J. J.; Guo, P.; Bartlett, B. M. *Inorg. Chem.* **2013**, *52*, 9363–9368.
(15) Ma, B.; Yang, J.; Han, H.; Wang, J.; Zhang, X.; Li, C. *J. Phys. Chem. C* **2010**, *114*, 12818–12822.
(16) Maeda, K.; Ohno, T.; Domen, K. *Chem. Sci.* **2011**, *2*, 1362.
(17) Ran, J.; Zhang, J.; Yu, J.; Jaroniec, M.; Qiao, S. Z. *Chem. Soc. Rev.* **2014**, *43*, 7787–7812.
(18) Borgarello, E.; Pelizzetti, E. *Inorganica Chim. Acta* **1984**, *91*, 295–300.
(19) Minero, C.; Lorenzi, E.; Pramauro, E.; Pelizzetti, E. *Inorganica Chim. Acta* **1984**, *91*, 301–305.
(20) Maeda, K.; Abe, R.; Domen, K. *J. Phys. Chem. C* **2011**, *115*, 3057–3064.

(21) Maeda, K.; Teramura, K.; Lu, D.; Saito, N.; Inoue, Y.; Domen, K. *Angew. Chem. Int. Ed. Engl.* **2006**, *45*, 7806–7809.
(22) Kim, E. S.; Nishimura, N.; Kim, J. Y.; Jang, J.-W.; Jun, H.; Kubota, J.; Domen, K.; Lee, J. S. *J. Am. Chem. Soc.* **2013**, *135*, 5375–5383.
(23) Leonard, K. C.; Nam, K. M.; Lee, H. C.; Kang, S. H.; Park, H. S.; Bard, A. J. **2013**.
(24) Kim, H., Majima, T., Choi, W. *Energy Environ. Sci.* **2013**, *advance*.
(25) Pilli, S. K.; Deutsch, T. G.; Furtak, T. E.; Brown, L. D.; Turner, J. a; Herring, A. M. *Phys. Chem. Chem. Phys.* **2013**, *15*, 3273–3278.
(26) Kim, E. S.; Kang, H. J.; Magesh, G.; Kim, J. Y.; Jang, J.; Lee, J. S. *ACS Appl. Mater. Interfaces* **2014**, *6*, 17762–17769.
(27) Hou, J.; Yang, C.; Cheng, H.; Jiao, S.; Takeda, O.; Zhu, H. *Energy Environ. Sci.* **2014**, *7*, 3758–3768.
(28) Zhu, J.; Li, W.; Li, J.; Li, Y.; Hu, H.; Yang, Y. *Electrochim. Acta* **2013**, *112*, 191–198.
(29) Chen, H.; Leng, W.; Xu, Y. *J. Phys. Chem. C* **2014**, *118*, 9982–9989.
(30) Hill, J. C.; Ping, Y.; Galli, G. a.; Choi, K.-S. *Energy Environ. Sci.* **2013**, *6*, 2440.
(31) Yourey, J. E.; Bartlett, B. M. *J. Mater. Chem.* **2011**, *21*, 7651.
(32) Pyper, K. J.; Yourey, J. E.; Bartlett, B. M. *J. Phys. Chem. C* **2013**, *117*, 24726.
(33) Gaillard, N.; Chang, Y.; DeAngelis, A.; Higgins, S.; Braun, A. *Int. J. Hydrogen Energy* **2013**, *38*, 3166–3176.
(34) Lalić, M. V; Popović, Z. S.; Vukajlović, F. R. *Comput. Mater. Sci.* **2011**, *50*, 1179–1186.
(35) Yourey, J. E.; Pyper, K. J.; Kurtz, J. B.; Bartlett, B. M. **2013**.
(36) Augustynski, J.; Solarska, R.; Hagemann, H.; Santato, C. *Proc. SPIE* **2006**, *6340*, 63400J–63400J–9.
(37) Mi, Q.; Zhanaidarova, A.; Brunschwig, B. S.; Gray, H. B.; Lewis, N. S. *Energy Environ. Sci.* **2012**, *5*, 5694–5700.
(38) Hill, J.; Choi, K. *J. Phys. Chem. C* **2012**, 7612–7620.
(39) Chang, Y.; Braun, A.; Deangelis, A.; Kaneshiro, J.; Gaillard, N. *J. Phys. Chem. C* **2011**, *115*, 25490–25495.
(40) He, X.; Ortiz de Montellano, P. R. *J. Org. Chem.* **2004**, *69*, 5684–5689.
(41) He, X.; Ortiz de Montellano, P. R. *J. Biol. Chem.* **2004**, *279*, 39479–39484.
(42) Trotochaud, L.; Young, S. L.; Ranney, J. K.; Boettcher, S. W. *J. Am. Chem. Soc.* **2014**, *136*, 6744–6753.
(43) Mora-Seró, I.; Villarreal, T. L.; Bisquert, J.; Pitarch, A.; Gómez, R.; Salvador, P. *J. Phys. Chem. B* **2005**, *109*, 3371–3380.
(44) Monllor-Satoca, D.; Borja, L.; Rodes, A.; Gómez, R.; Salvador, P. *Chemphyschem* **2006**, *7*, 2540–2551.
(45) Villarreal, T. L.; Go, R.; Gonza, M.; Salvador, P. *J. Phys. Chem. B* **2004**, *108*, 20278–20290.

Chapter 7

Conclusions and Potential Future Directions

7.1 Summary of Presented Work

The work presented in this thesis establishes 1) the fundamental chemical properties of co-incorporated titanium dioxide semiconductors, including TiNbON; 2) their competence as catalysts for both methylene blue photomineralization (primarily useful as a benchmarking reaction for research purposes) and photochemical water oxidation; and 3) a new synthetic pathway for preparing titanium niobium oxynitrides that could potentially be used to more rigorously control stoichiometry in the quaternary system. Furthermore, the final chapter of this thesis explores WO_3 photoanodes modified by $CuWO_4$ and $Cu_{0.95}Ni_{0.05}WO_4$ overlayers as improved materials for photoelectrochemical water oxidation.

While the urea-glass method offers tunability in metal content and potentially nitrogen content, that potential has yet to be experimentally verified. This work serves to establish the proof-of-concept necessary for further investigations into the synthetic method as it applies to TiNbON or, hypothetically, any other Ti(M)ON. There is potential for further development from the findings presented in Chapters 4 and 5, and some ideas are highlighted below.

Regarding the work in Chapter 6 on WO_3/MWO_4 photoanodes, the OER and radical trapping results are inconclusive due to high variability in the electrode performance sample to sample. This is particularly problematic when interpreting the OER data, where the variance in the measurement is larger than the observed effect size. Two factors are at play here. First, the

FOSSPOR probe used for the oxygen headspace analysis is quite variable and requires an extensive number of trials to obtain reliable data. Cell leaks are often encountered. A more reliable method of oxygen detection, preferably in-line gas chromatography, is required. Secondly, the solution-based method for preparing the MWO_4 overlayer results in a mechanically unstable film with highly variable surface coverage. A more controlled method for preparing overlayers, such as electrodeposition or atomic layer deposition, is desirable, though methods for preparing complex ternary oxides by these methods remain unavailable.

An interesting area for further research from Chapter 6 is the use of α-thujone as a chemical probe for hydroxyl radical activity. In evaluating new semiconducing materials as photocatalysts in aqueous solution, whether for water splitting or otherwise, knowing the prevalence of hydroxyl radical is critical to interpreting stability data and, in the case of organic transformations on semiconductor surfaces, reactivity. Methods for radical detection typically involve spin trapping agents such as (2,2,6,6-tetramethylpiperidin-1-yl)oxidanyl (TEMPO) and N-tert-Butyl-α-(4-pyridyl)nitrone N′-oxide (POBN) which, while stable on their own, often form spin adducts that are easily quenched by oxygen. Each α-thujone oxidation product is a closed-shell, stable organic molecule which can be detected by GCMS.[1,2] A large amount of organic synthesis may be required to fully standardize this chemical probe. However, its potential application to oxygenated environments with high anodic biases is a point of merit.

7.2 Ammonia Selective Electrodes for Compositional Analysis

Chemical analysis for nitrogen content by the Kjeldahl method presented in Chapter 4 is a mainstay method for organic chemistry biochemistry. Kjeldahl analysis is typically performed with large sample sizes (gram scale) on compounds with comparatively high nitrogen content; for example, β-lactoglobulin has a Kjeldahl nitrogen content of ~15%.[3]

In the present work, Kjeldahl analysis requires nearly unworkably large sample sizes to detect even small amounts of nitrogen. TiNbON-5, the compound analyzed to complete empirical formula in Chapter 4, possessed 0.42 % N by mass and required a 1-gram sample to obtain a reliable analysis. Due to the time required to prepare titanium niobium oxynitride by the present methods, obtaining such large sample sizes for a range of synthetic samples is extremely difficult. Conducting the measurements required to determine whether a synthetic strategy establishes control over the resultant nitrogen in a series of compounds is precluded by this difficulty.

This problem could be avoided through the use of an ammonium ion-selective electrode (ISE). Ion-selective electrodes function when a difference in the concentration of a certain analyte ion on either side of a selective membrane establishes a difference in electrical potential between the standardized solution inside the electrode and the analyte solution outside. Ammonium-selective electrodes are well-documented in the scientific literature. Common interferent species are cations of alkali metals, particularly K^+.[4] Higher-valent alkaline-earth metal cations appear not to interfere.

A proposed analysis scheme for TiNbON materials with an ISE would look very similar to that of Kjeldahl analysis. The material would still require strongly acidic and fluorided solution to dissolve the TiO_2-like material and release ammonium cation to solution. However, after the material is fully dissolved, the solution – which could potentially be of a very small volume depending on the size of the ion-selective device – is hypothetically prepared for analysis.

Compositional analysis with an ammonium ISE is a low-cost and potentially more accurate alternative to expensive spectroscopic methods such as X-ray photoelectron spectroscopy and Auger electron spectroscopy, and could enable higher-throughput determination of chemical formulae for experimental TiNbON materials.

7.3 Thin Film Photoelectrodes of TiNbON

Giordano et al.[5] demonstrated the facile application of the urea-glass synthesis towards preparing immobilized films of metal nitrides and carbonitrides. Metal nitrides have been mixed with conductive carbon additives and immobilized in Nafion membranes to prepare electrocatalytic materials.[6,7] However, a detailed study that furthers the preparation method by immobilizing a urea-glass product to create a photoelectrode has not yet been reported.

Preparing TiNbON photoelectrodes can be achieved by drying the urea-glass precursor onto a clean fluorinated tin oxide substrate and carrying out the synthesis as outlined in Chapters 4 or 5. Obtaining high-quality photoelectrodes would enable studying TiNbON as a candidate material for photoelectrochemical water splitting schemes, as well as probing certain fundamental materials parameters such as whether a given TiNbON composition is n-type or p-type, dopant density and kinetic overpotential for HER and/or OER that are most easily studied electrochemically.

7.4 Further Reactivity Studies with TiNbON prepared by Urea-Glass Synthesis

Dye degradation studies on TiNbON materials, reported in this thesis and elsewhere, have demonstrated an increase in methylene blue surface saturation as a function of increasing niobium content. While the exact adsorption mechanism of methylene blue to these materials is not known, it can be reasonably hypothesized that the basic, neutral nitrogen pyridine-like heteroatom is the most likely binding site (as opposed to what in the major resonance contributor is a positively-charged sulfur). According to established hard-soft acid base theory, Nb^{5+} is predicted to have a somewhat lower chemical hardness than Ti^{4+}.[8] In aqueous solution, these neutral nitrogen bases must compete with water and hydroxide for surface sites; a potential explanation for the increase in surface coverage by methylene blue could be that the softer Nb^{5+} acid appearing on the surface decreases its affinity for harder aquo and hydroxide bases, concurrently increasing its relative affinity for methylene blue. Increasing niobium content induces this effect whether the photochemistry is promoted (as in Breault *et al*.)[9] or hindered (as presented here) by increased Nb.

Recently, research groups have begun to apply semiconductors as photochemical catalysts for alcohol, and amine oxidation. TiO_2 and Nb_2O_5 have emerged independently as preeminent materials for these reactions in terms of their kinetic rate (time to complete conversion) and selectivity.[10,11] However, as TiO_2 and Nb_2O_5 are both white, wide-gap materials, ultraviolet light is often required to promote these reactions. An increased rate and higher energy efficiency are both possible with visible light-absorbing TiNbON.

Strong adsorption of amine and imine bases to TiNbON is hypothesized based on observed trends in methylene blue adsorption. As substrate adsorption is a critical step in any heterogeneous catalyst cycle, and as both TiO_2 and $Nb2O_5$ surfaces have demonstrated favorable selectivity for these oxidations, pursuing organic oxidations over TiNbON may be a promising direction for further study.

7.5 Concluding Remarks

Synthetic pathways for preparing co-incorporated titania remain limited. Each report prepares the experimental material in a different way, and there is little continuity study-to-study. Furthermore, these synthetic methods are exclusively differentiated from one another on the basis of the reactivity of the obtained product. This represents a logical shortcoming. The work presented

herein contributes another synthetic method to the field's toolbox. What is missing from the field as a whole is consistent and rigorous compositional analysis. Interpretations of reactivity and defect structure, and consequently the synthetic method as a whole, are underinformed when the composition of the material in question remains mysterious. It is my opinion that a strong focus on compositional analysis will lead to rapid improvements in both the understanding of the properties of co-incorporated titania, as well as their performance as photocatalysts.

7.6 References

(1) He, X.; Ortiz de Montellano, P. R. Alpha- and Beta-Thujone Radical Rearrangements and Isomerizations. A New Radical Clock. *J. Org. Chem.* **2004**, *69* (17), 5684–5689.

(2) He, X.; de Montellano, P. R. O. Radical Rebound Mechanism in Cytochrome P-450-Catalyzed Hydroxylation of the Multifaceted Radical Clocks Alpha- and Beta-Thujone. *J. Biol. Chem.* **2004**, *279* (38), 39479–39484.

(3) Chibnall, A. C.; Rees, M. W.; Williams, E. F. The Total Nitrogen Content of Egg Albumin and Other Proteins. *Biochem. J.* **1943**, *37* (3), 354.

(4) Benco, J. S.; Nienaber, H. A.; McGimpsey, W. G. Synthesis of an Ammonium Ionophore and Its Application in a Planar Ion-Selective Electrode. *Anal. Chem.* **2003**, *75* (1), 152–156.

(5) Giordano, C.; Erpen, C.; Yao, W.; Milke, B.; Antonietti, M. Metal Nitride and Metal Carbide Nanoparticles by a Soft Urea Pathway. *Chem. Mater.* **2009**, *21* (21), 5136–5144.

(6) Molinari, V.; Giordano, C.; Antonietti, M.; Eposito, D. Titanium Nitride-Nickel Nanocomposite as Heterogeneous Catalyst for the Hyrogenolysis of Aryl Ethers. *J. Am. Chem. Soc.* **2014**, *136* (5), 1758–1761.

(7) Youn, D. H.; Bae, G.; Han, S.; Kim, J. Y.; Jang, J.-W.; Park, H.; Choi, S. H.; Lee, J. S. A Highly Efficient Transition Metal Nitride-Based Electrocatalyst for Oxygen Reduction Reaction: TiN on a CNT–graphene Hybrid Support. *J. Mater. Chem. A* **2013**, *1* (27), 8007.

(8) Pearson, R. G. Absolute Electronegativity and Hardness: Application to Inorganic Chemistry. *Inorg. Chem.* **1988**, *27* (4), 734–740.

(9) Breault, T. M.; Bartlett, B. M. Composition Dependence of TiO_2:(Nb,N)-X Compounds on the Rate of Photocatalytic Methylene Blue Dye Degradation. *J. Phys. Chem. C* **2013**, *117* (17), 8611–8618.

(10) Lang, X.; Ji, H.; Chen, C.; Ma, W.; Zhao, J. Selective Formation of Imines by Aerobic Photocatalytic Oxidation of Amines on TiO_2. *Angew. Chemie Int. Ed.* **2011**, *50* (17), 3934–3937.

(11) Furukawa, S.; Ohno, Y.; Shishido, T.; Teramura, K.; Tanaka, T. Selective Amine Oxidation Using Nb_2O_5 Photocatalyst and O_2. *ACS Catal.* **2011**, *1* (10), 1150–1153.

Appendix A

Supporting Information for Chapter 3

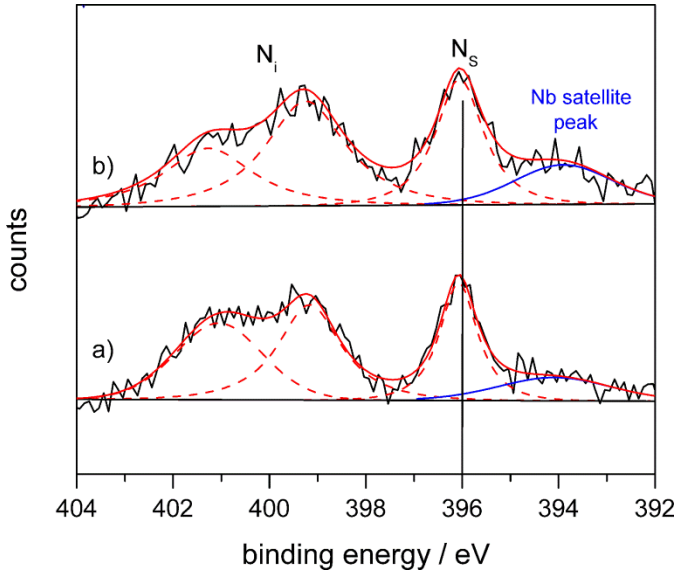

Figure A1. X-ray photoelectron spectra of N(1s) peak a) before and b) after annealing TiNbON-25 at 350 °C for 1 hour. N_i denotes interstitial nitrogen, N_S denotes substitutional nitrogen.

Table A1. XPS Ratios of N_s/N_i

Sample	N_s/N_i ratio
TiNbON-25 / **1**	0.350
1 heated at 350 °C for 1 hour	0.445

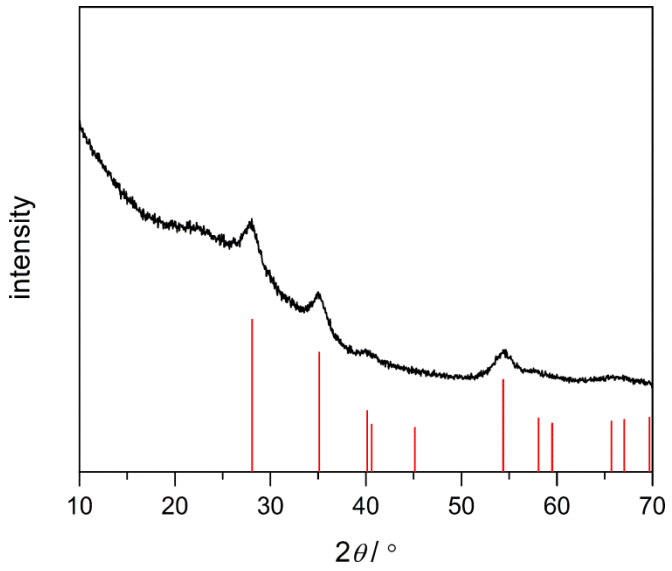

Figure A2. XRD of $RuCl_3$ annealed at 350 °C for 1 hour, yielding RuO_2 (JCPDF 70-2662).

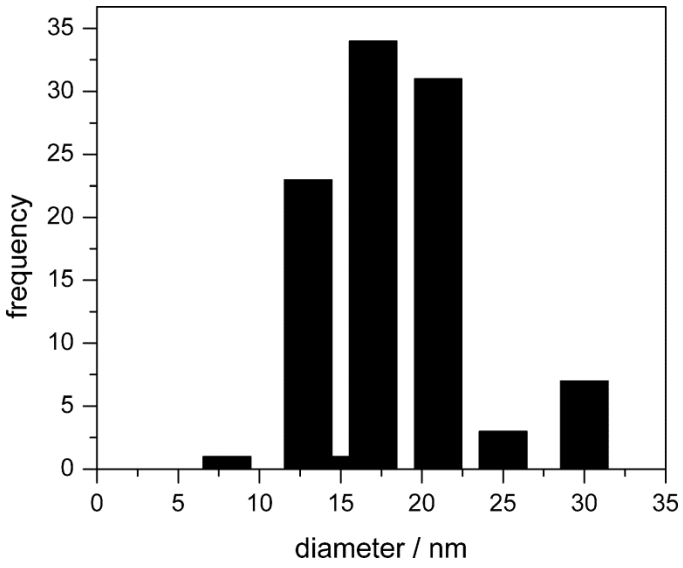

Figure A3. Histogram of particle size for 100 randomly measured particles by SEM.

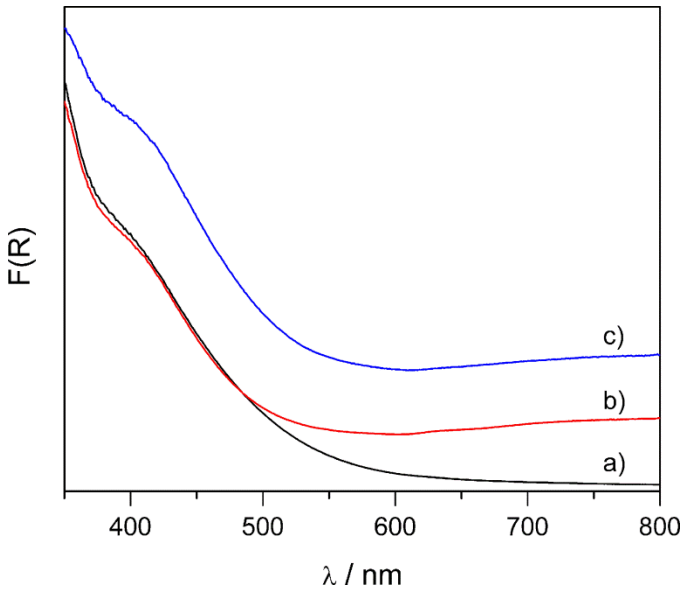

Figure A4. Diffuse reflectance UV-Vis spectroscopy of a) TiNbON-25 and b) TiNbON-25 loaded with 1 wt% RuO_2 and annealed at 350 °C for 1 hour, and c) 2 wt% RuO_2.

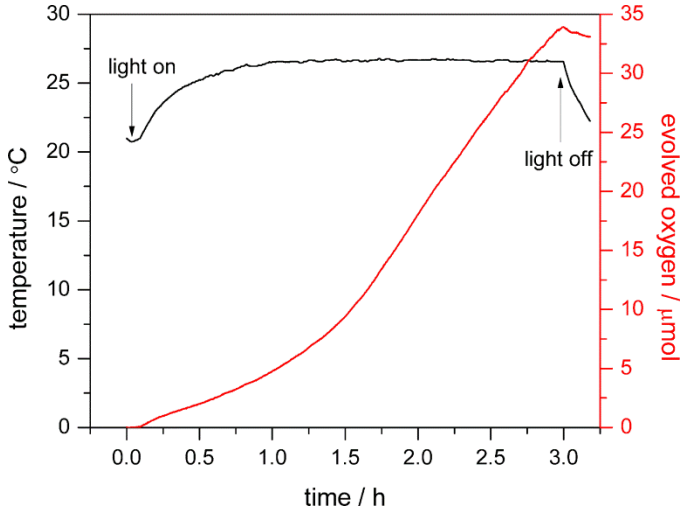

Figure A5. Temperature *vs.* time for a representative oxygen-evolution experiment. Reaction conditions: 50 mg catalyst, 1 mM $NaIO_3$ (30 mL), 150 W Xe lamp fitted with water filter and 295 nm cut-on filter (~ 600 mW/cm^2), and a custom built Pyrex cell fitted with a quartz window.

Appendix B

Supporting Information for Chapter 4

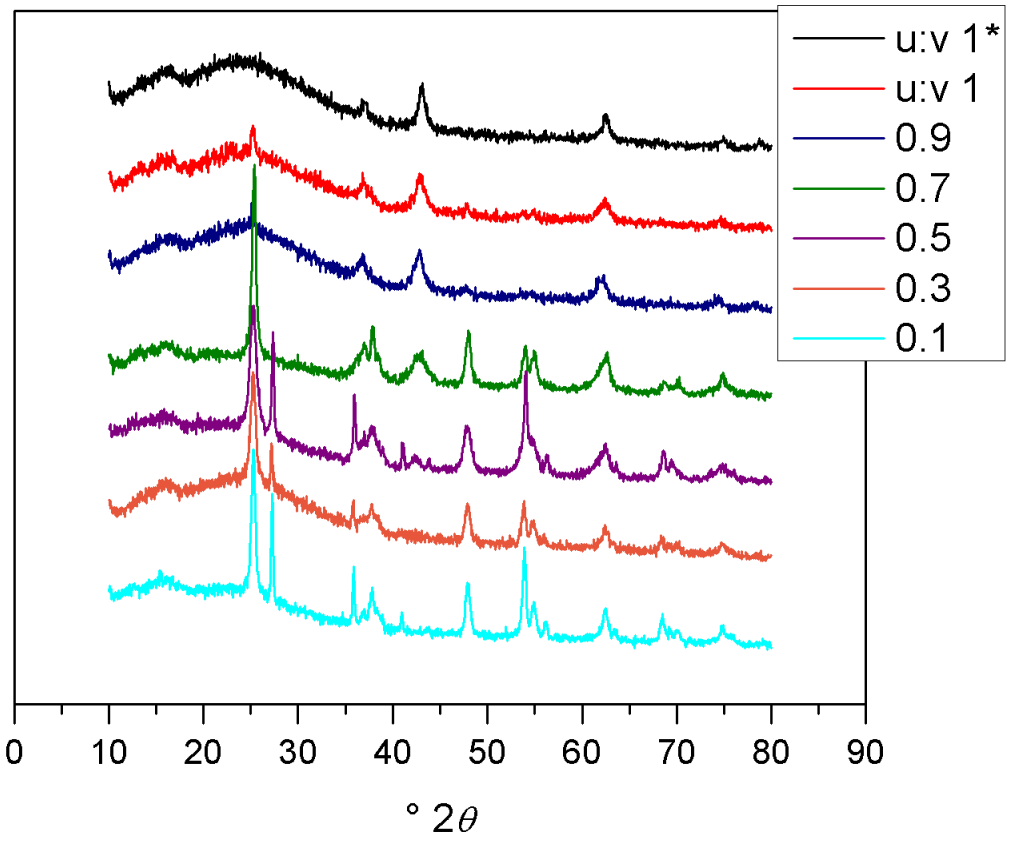

Figure B1. Urea-glass synthesis products prepared at different urea:valence ratios *R*, denoted here u:v. *: No Nb added. All other samples prepared using a metals ratio of $Ti_{0.85}Nb_{0.15}$.

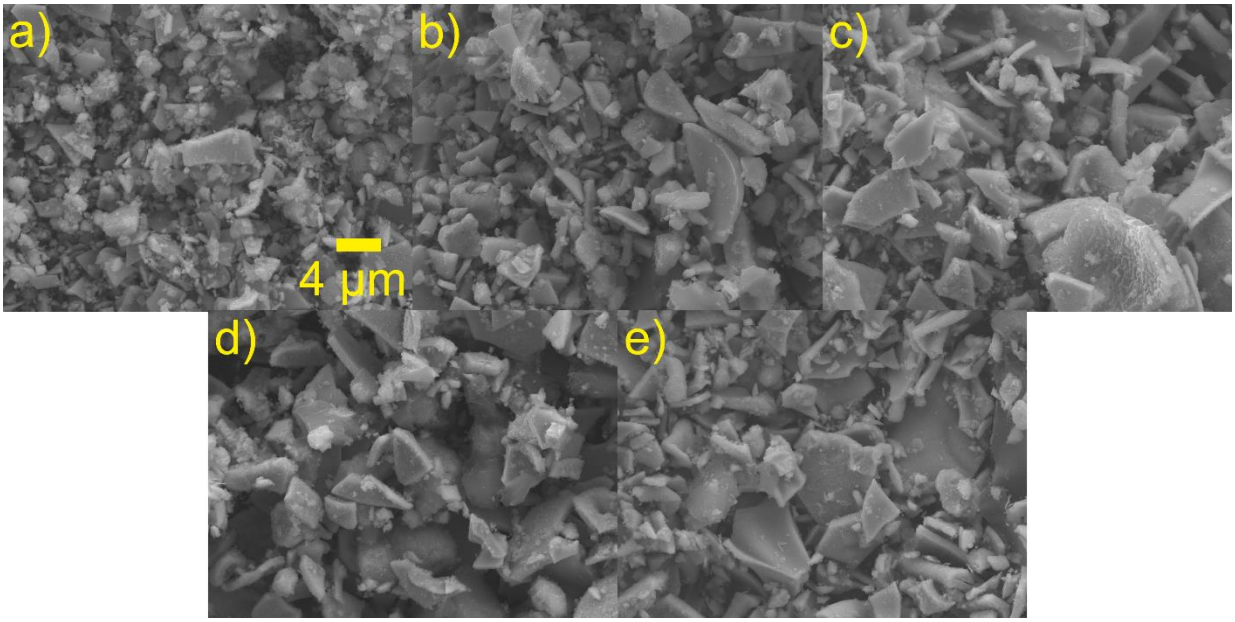

Figure B2. Scanning electron micrographs of $Ti_{1-x}Nb_xN$ prepared by the urea-glass route: a) x = 0, b) x = 5, c) x = 15, d) x = 25, e) x = 30. Each sample shares a common scale bar.

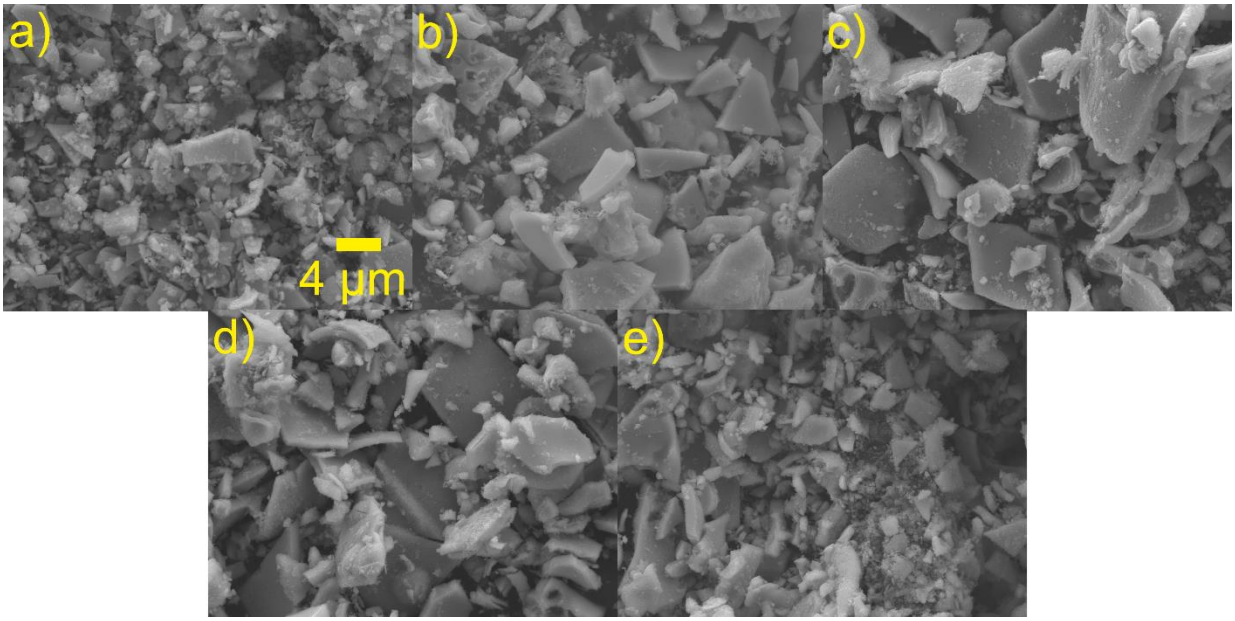

Figure B3. Scanning electron micrographs of TiNbON-X prepared by the urea-glass route: a) x = 0, b) x = 5, c) x = 15, d) x = 25, e) x = 30. Each sample shares a common scale bar.

Table B1. Metal contents for $Ti_{1-x}Nb_xN$ found by energy dispersive X-ray spectroscopy.

x	0	5	15	25	30
Found Ti:Nb	Ti_1Nb_0	$Ti_{0.92}Nb_{0.08}$	$Ti_{0.82}Nb_{0.18}$	$Ti_{0.77}Nb_{0.23}$	$Ti_{0.69}Nb_{0.31}$

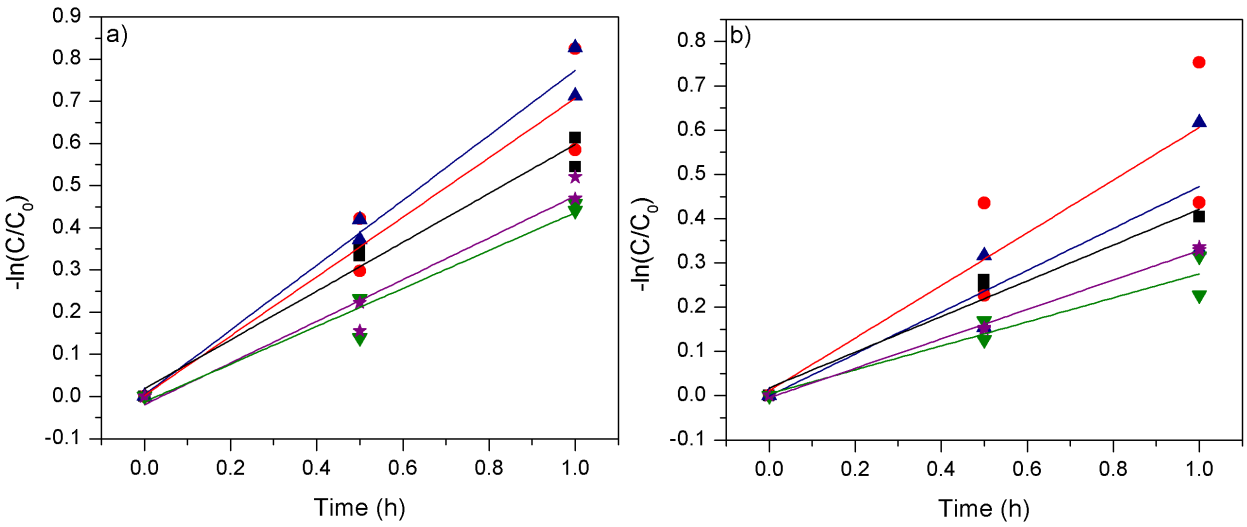

Figure B4. Linear fits for first-order Langmuir-Hinshelwood kinetics for a) full-spectrum and b) $\lambda \geq 400$ nm methylene blue degradation measurements. The slope of the fit line is the rate constant for the reaction. Black squares: TiNbON-0; red circles: TiNbON-5; blue up-triangles: TiNbON-15; green down-triangles: TiNbON-25; purple stars: TiNbON-30.

Table B2. First-order Langmuir-Hinshelwood rate constants for methylene blue degradation (k_{LH}) and specific methylene blue adsorption (q_{rel}) over TiNbON-*x* compounds, along with BET surface areas.

	TiNbON-0	TiNbON-5	TiNbON-15	TiNbON-25	TiNbON-30
k_{LH} (h^{-1}) full spectrum	0.579 ± 0.041	0.704 ± 0.096	0.769 ± 0.044	0.449 ± 0.040	0.494 ± 0.045
k_{LH} (h^{-1}) $\lambda \geq 400$ nm	0.404 ± 0.031	0.595 ± 0.136	0.473 ± 0.117	0.332 ± 0.009	0.333 ± 0.016
q_{rel}, mg/g	2.5 ± 0.6	7.4 ± 2.8	21.2 ± 2.2	19.4 ± 2.4	24.4 ± 1.6
surface area, m^2/g	41	36	40	46	45

Appendix C

Supporting Information for Chapter 6

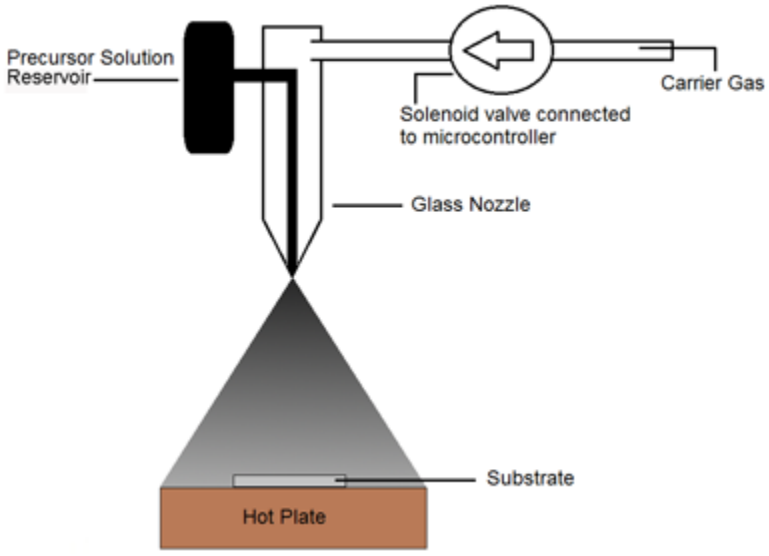

Figure C1. Schematic depiction of the spray pyrolysis apparatus used to synthesize pure-phase $CuWO_4$ and $Cu_{0.95}Ni_{0.05}WO_4$ films.

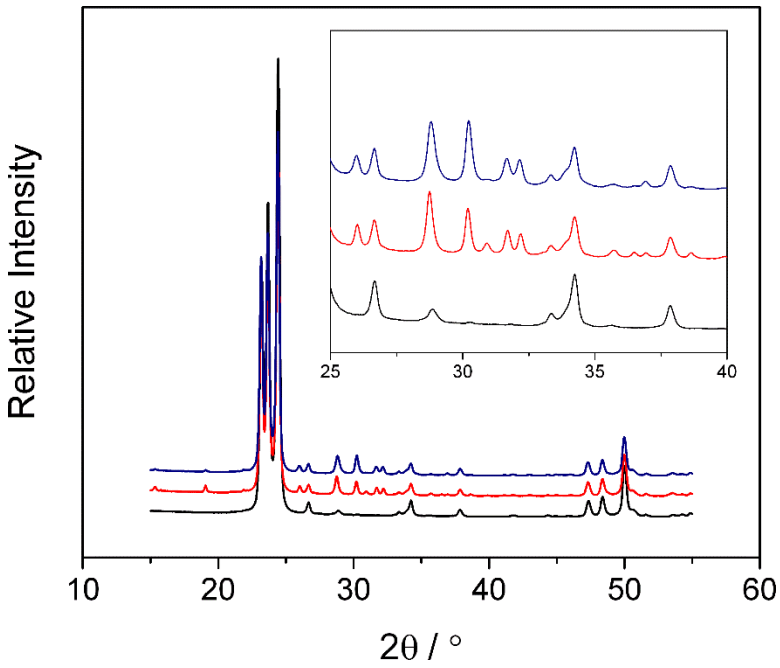

Figure C2. Powder x-ray diffraction patterns of sol-gel WO_3 (black), BHJ-Cu (red), and BHJ-CuNi films after synthesis and soaking in 0.5 M HCl. Inset: enlarged pattern between 25-40° 2θ, showing the appearance of $CuWO_4$ peaks for BHJ films.

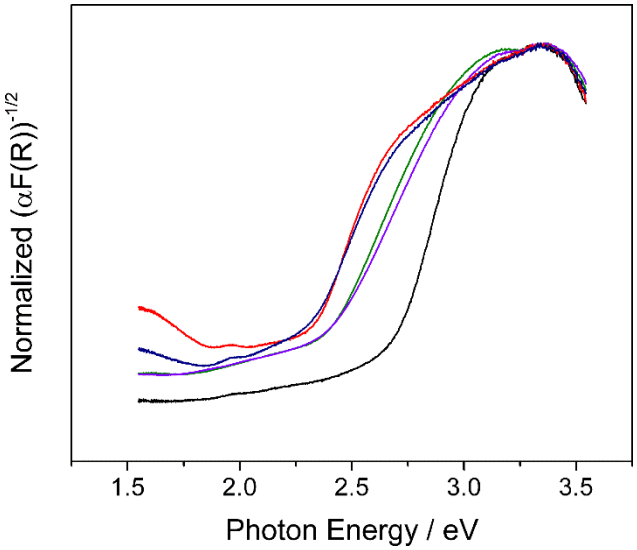

Figure C3. Tauc plots for UV-Vis diffuse reflectance spectra of WO_3 and MWO_4 thin films. Legend: WO_3 (black), BHJ-Cu (red), BHJ-CuNi (blue), $CuWO_4$ (green), and $Cu_{0.95}Ni_{0.05}WO_4$ (violet).

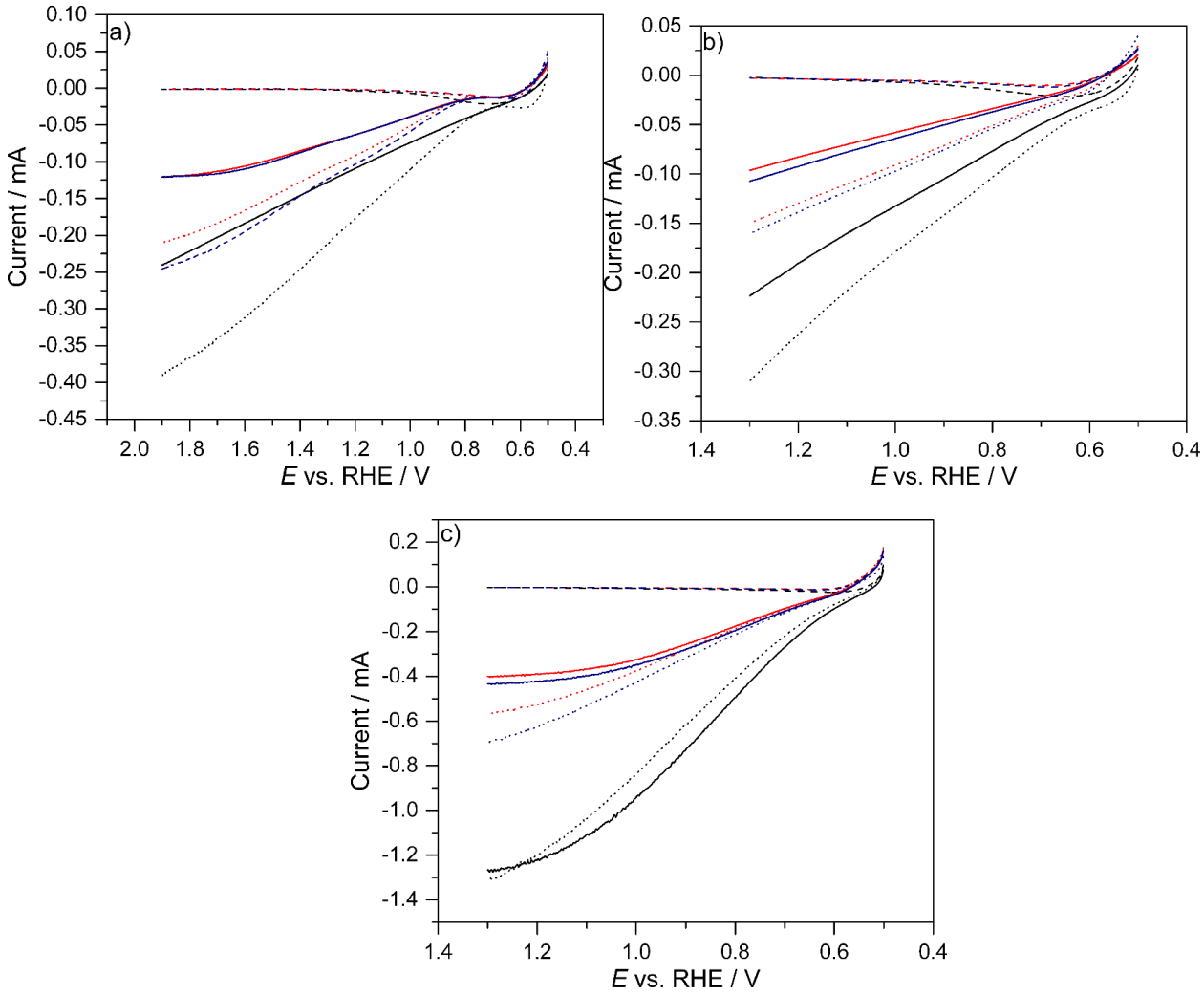

Figure C4. Linear sweep voltammograms of WO_3 and BHJ electrodes in 0.1 M KBi with no additives (a), 0.2 M methanol (b), and 0.2 M formate (c) added. Dashed lines depict the current response under no illumination, solid lines from electrode-electrolyte (EE) illumination, and dotted lines from substrate-electrolyte (SE) illumination. Legend: WO_3 (black), BHJ-Cu (red), BHJ-CuNi (blue).